Electronic transport in the presence of localized states in disordered semiconductors

Abel Thayil

INSTITUT POLYTECHNIQUE DE PARIS

NNT : 2022IPPAX142

Thèse de doctorat

ÉCOLE POLYTECHNIQUE

IP PARIS

Electronic transport in the presence of localized states in disordered semiconductors

Thèse de doctorat de l'Institut Polytechnique de Paris
préparée à l'École polytechnique

École doctorale n°626
Spécialité de doctorat : Physique

Thèse présentée et soutenue à Palaiseau, le 20/12/2022, par

ABEL THAYIL

Silke Biermann Directrice de recherche Ecole polytechnique - CPHT, France	Présidente
Bernard Gil Directeur de recherche Université de Montpellier, Laboratoire Charles Coulomb, France	Rapporteur
Christophe Texier Professeur Université Paris Saclay, LPTMS, France	Rapporteur
Maria Chamarro Professeure Sorbonne Université - INSP, France	Examinatrice
Marcel Filoche Directeur de recherche Ecole polytechnique - LPMC, France ESPCI, PSL University, Institut Langevin, France	Directeur de thèse
Jacques Peretti Directeur de recherche Ecole polytechnique - LPMC, France	Co-directeur de thèse

Acknowledgements

It is an honor and privilege to be a Ph.D student and I would like to thank my Ph.D supervisor, Marcel Filoche, firstly, for giving me such an opportunity. I am equally grateful for his time, valuable feedback and attention to detail which have contributed to making me a better scientist.

I thank Jacques Peretti for his constant presence which had a calming effect and for the stimulating discussions.

I am grateful to Alistair Rowe for his guidance with the work on the space charge limited regime. I have learnt a lot about semiconductor physics from him.

My work builds on work done by Jean-Marie Lentali and Perceval Desforges. Their contributions were invaluable to me. I have benefitted a lot from my discussions with members of the EPS group, Claude Weisbuch, Fabian Cadiz, Fausto Sirotti and Yves Lasailly, to name a few. My work would not have been possible without my daily interactions with Jean-Philippe Banon, Mylène Sauty, Pierre Pelletier, Alioune Seye and Wiebke Hahn.

The Simon's collaboration on the localization of waves was an exciting scientific community and I learnt a lot by pariticipating in their events. I am particularly grateful to Douglas Arnold and Tyson Loudon for help with the some of the numerical aspects of this thesis.

I am grateful to Hervé Henry, Denis Coupvent-Desgraviers, Julien Monguillon and Antoni Fernandes for technical support and Anne-Marie Dujardin for administrative support. I would also like to thank Mathis Plapp for pointing me in the right direction during stressful times.

My friends were a constant source of support and inspiration, Maria, Bruno, Aishwarya, John, Mher, and so many others. Finally, I would not have made it this far without my parents, Shelley and Anju, and brother Ansh.

Résumé en français

Le développement de l'industrie des semi-conducteurs et la recherche en physique des semi-conducteurs ont entraîné la miniaturisation des dispositifs à l'échelle nanométrique. La physique des semi-conducteurs implique souvent la compréhension des propriétés électroniques et optiques de différents matériaux semi-conducteurs ainsi que de leurs applications aux dispositifs. Dans ce contexte, la description de ces dispositifs repose souvent sur certaines hypothèses concernant la symétrie du matériau, ce qui rend le problème gérable. Par exemple, une hypothèse courante est que les semi-conducteurs sont parfaitement périodiques et que les états électroniques sont des ondes de Bloch délocalisées, ce qui signifie que l'état électronique est délocalisé sur toute la structure du semi-conducteur, une conséquence de sa nature d'onde.
Cependant, à l'échelle nanométrique, toutes les imperfections ou inhomogénéités du matériau peuvent avoir un impact considérable sur les performances électriques ou optiques. La présence d'un degré croissant de désordre dans certains types de matériaux tels que les semi-conducteurs amorphes, les semi-conducteurs organiques ou les alliages aléatoires d'InGaN peut changer la nature délocalisée des fonctions d'onde électroniques. Dans ces cas, les matériaux présentent un désordre structural ou de substitution et, par conséquent, l'électron subit un potentiel désordonné. La fonction d'onde électronique peut ainsi se localiser en raison d'interférences destructives, un exemple célèbre de cela étant la localisation d'Anderson.
Le transport de charges dans les semi-conducteurs peut être largement classé en deux régimes en fonction du degré de localisation des états électroniques impliqués dans le processus, à savoir le transport de bande et le transport de saut. Si les électrons impliqués dans le transport sont des ondes de Bloch délocalisées, le mécanisme de transport est appelé transport de bande. Si les états électroniques impliqués dans le transport sont localisés et que le porteur de charge saute donc entre des états lo-

calisés, le mécanisme est appelé transport de saut. Le transport peut également se produire par une combinaison des deux processus, et le mécanisme dominant dépend de la concentration des porteurs, de la température de l'échantillon et du degré de désordre, pour ne citer que quelques paramètres importants.

Nous commençons par décrire le transport de bande en présence de profonds états localisés dans le régime de charge d'espace. Le régime de charge d'espace correspond aux situations où des champs électrostatiques non négligeables sont présents dans un semi-conducteur, modifiant ainsi le courant. La prise en compte du champ électrostatique nécessite la résolution de l'équation de Poisson couplée aux équations de dérive-diffusion et aux équations de conservation de courant. Nous montrons que les effets de l'électrostatique et de la recombinaison via des pièges profonds sont importants pour modéliser de manière appropriée les caractéristiques intensité-tension dans des échantillons expérimentaux de silicium piézorésistif.

Nous modélisons ensuite le transport par saut entre des états localisés induits par le désordre intrinsèque. Le transport par saut se produit lorsqu'un électron saute d'un état localisé à un autre, assisté par des phonons. Ce transport est prédominant à des concentrations de porteurs suffisamment basses et à des températures suffisamment basses. Le transport par saut est souvent étudié à l'aide du modèle de Miller-Abrahams qui nécessite un ensemble de paramètres empiriques pour définir les taux de saut et les chemins préférentiels entre les états. Nous montrons que ce réseau de saut peut être visualisé avec un potentiel effectif dérivé de la théorie du paysage de localisation, et que le couplage entre les états localisés est essentiellement soutenu le long des géodésiques d'une métrique déduite du paysage de localisation. Le réseau de saut est caractérisé par les longueurs de localisation des états, leurs niveaux d'énergie et les taux de saut subséquents entre les différents états. Nous calculons les taux de saut en utilisant ce potentiel effectif, comparons ses prédictions avec les calculs d'états propres exacts, puis évaluons l'applicabilité de la modélisation du transport par saut en utilisant la théorie du paysage de localisation.

Contents

Chapter 1

Introduction

Semiconductor devices are ubiquitous in modern society. They have integrated and made possible a large range of devices from computers, mobile phones, smart watches, cars, light emitting diodes (LEDs) to name a few, since the first transistors were invented in the 1940s. The development of the semiconductor industry and in parallel the research in semiconductor physics has led to the miniaturization of these devices to the nanometer scale. This has been accompanied with the research and incorporation of newer materials in such devices. At the nanometer scale, all imperfections or inhomogeneities of the material can drastically impact the electrical or optical performance. In this context, it is an important challenge to understand and model how charge carriers flow through these newer devices and materials.

Electrons in a semiconductor are governed by the Schrödinger equation. The time-independent Schrödinger equation for a single massive quantum particle is

$$-\frac{\hbar^2}{2m}\Delta\psi(\boldsymbol{r}) + V(\boldsymbol{r})\psi(\boldsymbol{r}) = E\psi(\boldsymbol{r}) \tag{1.1}$$

where $\boldsymbol{r}$ is the position, ψ is the wave function, m is the mass of the particle, V is the potential and E is the energy of the particle. The solutions ψ to the above equation in a periodic potential are Bloch waves. Mathematically, they read

$$\psi(\boldsymbol{r}) = e^{i\boldsymbol{k}.\boldsymbol{r}}u_{\boldsymbol{k}}(\boldsymbol{r}) \tag{1.2}$$

where $u_{\boldsymbol{k}}$ is a periodic function with the same periodicity as the potential and the

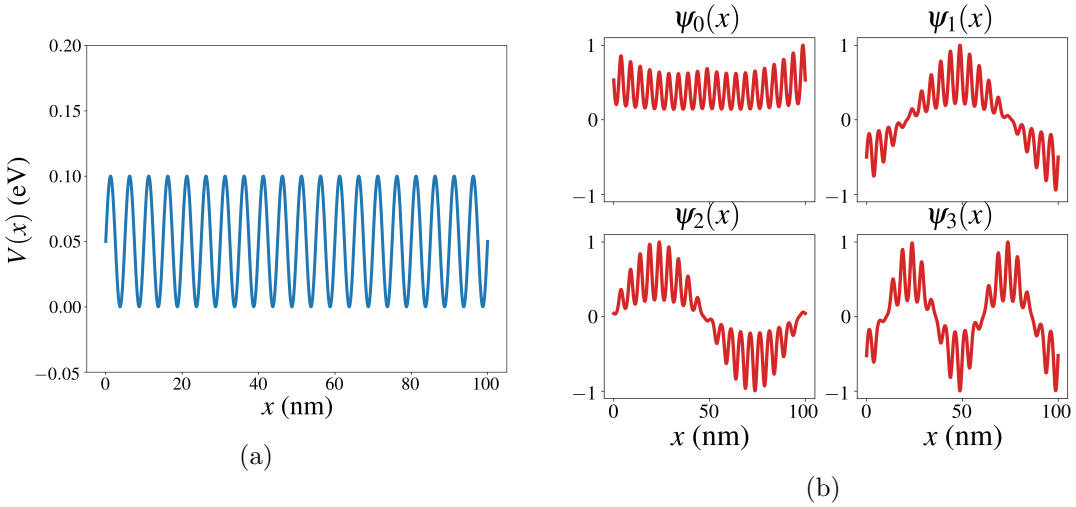

Figure 1.1: a) A one dimensional periodic potential $V(x) = A(1 + \sin(2\pi ax))$ with $A = 0.05\,\text{eV}$ and $a = 0.2\,\text{nm}^{-1}$. b) The first four eigenstates for the potential in a). One observes they are delocalized over the entire domain.

wave vector $\boldsymbol{k}$ is the crystal momentum vector. The above solutions are plane waves modulated by a periodic function, and therefore spatially extend over the entire domain as is shown for a few of the eigenstates in Fig. 1.1. Such states are referred to as *delocalized* or *extended* states. The above defined Bloch waves form the basis for band theory since the energies of the electronic states form separate bands when plotted as a function of the crystal momentum vector $\boldsymbol{k}$ as can be seen in Fig. 1.2.

Band theory has been successful in explaining the electronic and optical properties of many materials such as their conductivity, based on the degree of filling of the bands of the material. The assumption of a perfectly periodic potential which is necessary to have Bloch waves as solutions is not satisfied for the purest of materials, because there are always defects in the crystal lattice of any real sample. In addition, at any given temperature the crystal lattice is vibrating due to its thermal energy. Despite this, band theory based on Bloch waves performs remarkably well since, many quantities of interest such as the density of states and the carrier densities can be calculated as a small perturbation to the perfectly periodic case.

The presence of an increasing degree of disorder in certain kinds of materials such as amorphous semiconductors [1], organic semiconductors [2] or random alloys of InGaN [3], can change the delocalized nature of the electron wavefunctions. In

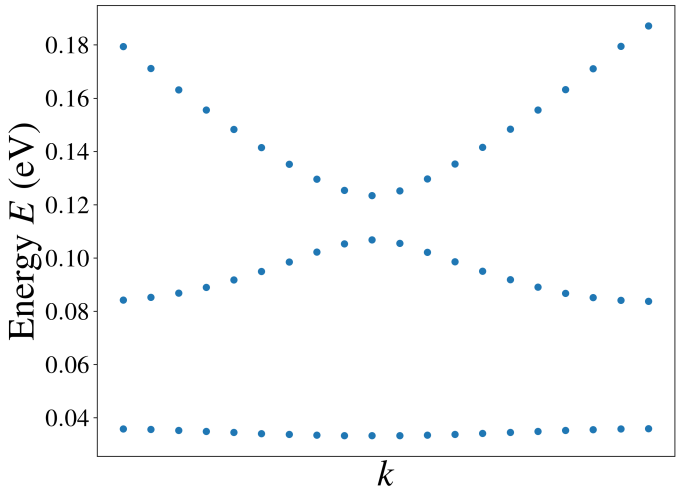

Figure 1.2: The band structure for the potential in Fig. 1.1.

these situations, the materials present structural or substitutional disorder and consequently the electron experiences a disordered potential. The electron wavefunction can thus localize due to destructive interferences [4]. In Fig. 1.4, we show localized eigenstates due to a disordered potential in one dimension.

In such a situation, $\boldsymbol{k}$ is no longer an appropriate quantum number for the electronic states. The localized nature of the electronic states affects the electronic transport in the material, and much work has been devoted to addressing the effects of disorder on electronic transport [7, 8]. This manuscript deals with the modeling of electronic transport in semiconductor devices in two different regimes. In the first regime, electronic transport is achieved via extended states and we study how the current is influenced by deep traps. In the second regime electronic transport occurs via localized states in semiconductors with compositional disorder. This work therefore treats the problem of modeling electronic transport in the presence of two kinds of disorder, defect states and intrinsic compositional disorder.

In the following section, we first outline some of the general theories of electronic transport in semiconductor physics.

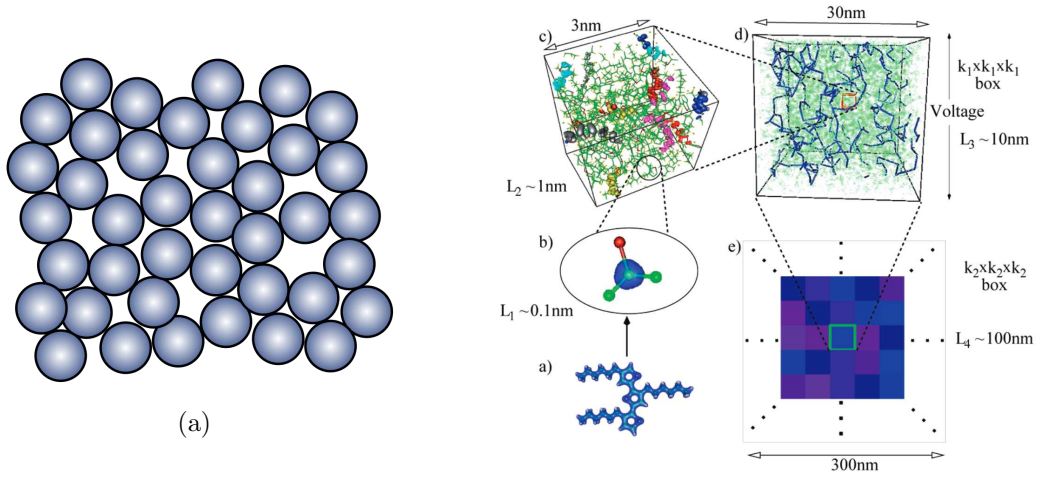

(a) (b)

Figure 1.3: Schematic of disordered semiconductors. a) An amorphous semiconductor (from [5]) and b) an organic semiconductor (from [6]).

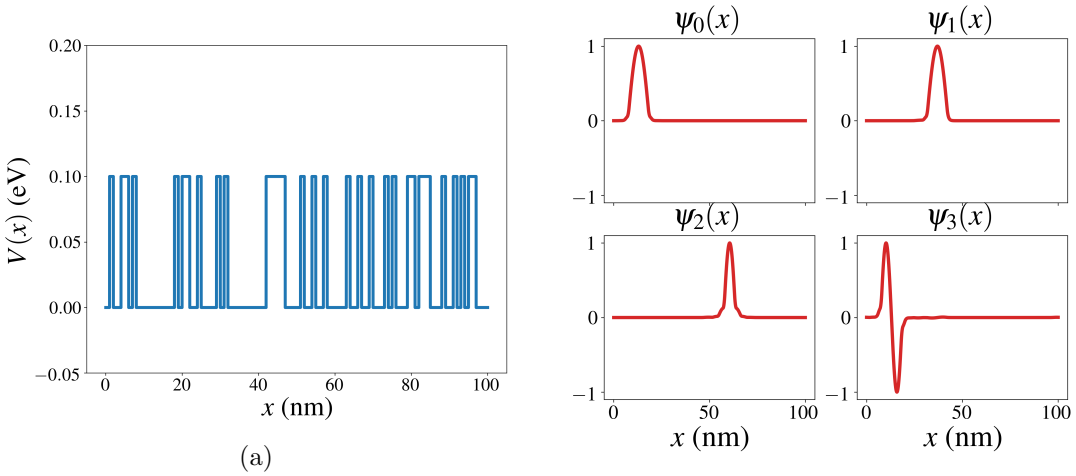

(a) (b)

Figure 1.4: a) A 1D disordered potential. b) The first four eigenstates of the potential in a). These states are localized.

1.1 Modeling electronic transport in semiconductors

Strictly speaking, electrons are quantum mechanical particles and therefore are governed by the laws of quantum mechanics. They are susceptible to quantum effects such as tunneling, interference and localization, and a quantum theory of transport is required to account for such effects. These effects are increasingly relevant in nanoscale devices and have led to the development of the field of mesoscopic physics [9]. However, for a large range of experiments and devices, the quantum formalism is not required. For many devices, a semi-classical treatment of the transport is sufficient, where the electrons are treated as classical particles and quantum mechanics enters only when calculating certain properties such as the effective mass of the electron, or while calculating the scattering rates of the particles with the crystal vibrations.

1.1.1 Quantum transport

To model how the electronic states evolve quantum mechanically in time, one needs to solve the time-dependent Schrödinger equation defined as

$$i\hbar\frac{\partial}{\partial t}\psi(\mathbf{r},t) = \hat{H}\psi(\mathbf{r},t) \tag{1.3}$$

where $\hat{H}$ is the Hamiltonian of the system. Semiconductors are macroscopic structures that involve many quantum particles that interact with each other and with the environment. To describe such systems in all generality, one must resort to quantum-statistical mechanics, and one of the key mathematical objects is the density matrix operator defined as

$$\hat{\rho} = \sum_{\alpha} p_\alpha \left|\psi_\alpha\right\rangle \left\langle\psi_\alpha\right| \tag{1.4}$$

where $\{|\psi_\alpha\rangle\}$ denotes a basis of eigenvectors for the system and p_α denotes the statistical probability of the system to be in the state $|\psi_\alpha\rangle$. For example, in the canonical ensemble, $p_\alpha = \frac{e^{-\beta E_\alpha}}{Z}$ is the Boltzmann weight, where E_α refers to the

energy of the state $|\psi_\alpha\rangle$, $\beta = (k_B T)^{-1}$ and Z refers to the partition function $Z = \sum_\alpha e^{-\beta E_\alpha}$. The overall expectation value of any observable $\hat{O}$ for an ensemble is given by

$$\langle \hat{O} \rangle = \mathrm{Tr}(\hat{\rho}\hat{O}) \tag{1.5}$$

where Tr refers to the trace of the operator. The temporal evolution of the density matrix operator derived from Eq. 1.3 is given by the Liouville-von Neumann equation

$$\hbar \frac{d\hat{\rho}}{dt} = -i[\hat{H}, \hat{\rho}], \tag{1.6}$$

where [..] refers to the commutator. Solving the Liouville-von Neumann equation is an amazingly difficult task. In linear response theory where the response of the system to a perturbation is considered linear in the perturbation, for example, we have Ohm's law $\boldsymbol{J} = \sigma \boldsymbol{F}$ where $\boldsymbol{J}$ is the current density, $\boldsymbol{F}$ is the applied field, and σ is the conductance of the system. The Hamiltonian is first written as the sum of an equilibrium Hamiltonian $\hat{H}_0$ with a time dependent perturbation $\hat{H}'(t)$ that drives the system out of equilibrium

$$\hat{H} = \hat{H}_0 + \hat{H}'(t) \tag{1.7}$$

where $\hat{H}'(t) = \hat{F} \cos \omega t$ is an applied electric field at a certain frequency ω. The linearization of the Liouville-von Neumann equation gives the Kubo formula [10, 11] which provides an expression for the conductivity tensor $\sigma_{\mu\nu}$

$$\sigma_{\mu\nu}(\omega) = \frac{1}{V} \int_0^\infty e^{-i\omega\tau} \int_0^\beta \langle \hat{J}_\nu(-i\hbar\beta') \hat{J}_\mu(\tau) \rangle d\beta' d\tau. \tag{1.8}$$

Here, $\hat{J}$ refers to the current density operator and V is the volume of the system. The above expression can be thought of as the quantum mechanical analogue of the fluctuation-dissipation theorem. Classically, the susceptibility of an observable in response to a perturbation is

$$\sigma_{\mu\nu}(\omega) = \frac{N}{V} \frac{q^2}{kT} \int_0^\infty e^{-i\omega\tau} \langle v_\nu(0) v_\mu(\tau) \rangle d\tau, \tag{1.9}$$

where N is the total number of particles, q is the charge of the carrier, $\langle v_\nu(0)v_\mu(\tau)\rangle$ is the velocity auto-correlation function, related to the diffusion constant D as $\int_0^\infty \langle v_\nu(0)v_\mu(\tau)\rangle d\tau = D$. The Kubo formula has been used to describe transient localization in disordered organic semiconductors [12] and electronic transport in organic crystals [13], among numerous other applications in the literature.

Another approach to quantum transport is via the Wigner-Weyl transform, which is a representation of quantum mechanics in phase space and involves both the momentum $\boldsymbol{k}$ and spatial variables $\boldsymbol{r}$. The Wigner function f_W, which was introduced to study the quantum corrections to classical statistical mechanics, is defined in phase space $(\boldsymbol{r}, \boldsymbol{k})$ as [14, 15, 11]

$$f_W(\boldsymbol{r}, \boldsymbol{k}) \equiv \int \left\langle \boldsymbol{r} + \frac{\boldsymbol{x}}{2} \,\middle|\, \hat{\rho} \,\middle|\, \boldsymbol{r} - \frac{\boldsymbol{x}}{2} \right\rangle \exp(-i\boldsymbol{k}.\boldsymbol{x}) d\boldsymbol{x} \tag{1.10}$$

The Wigner function satisfies many important properties. It can be understood as being close to a probability distribution in phase space. This statement comes from the fact that the two marginal integrals along $\boldsymbol{r}$ and $\boldsymbol{k}$ satisfy for pure states (when we have $\hat{\rho} = |\psi\rangle \langle\psi|$)

$$\frac{1}{(2\pi)^d} \int f_W(\boldsymbol{r}, \boldsymbol{k}) d\boldsymbol{k} = |\psi(\boldsymbol{r})|^2 \tag{1.11}$$

$$\frac{1}{(2\pi)^d} \int f_W(\boldsymbol{r}, \boldsymbol{k}) d\boldsymbol{r} = |\chi(\boldsymbol{k})|^2 \tag{1.12}$$

where $\chi(\boldsymbol{k})$ is the Fourier transform of the wave function ψ defined as $\chi(\boldsymbol{k}) = \frac{1}{(2\pi)^{d/2}} \int e^{-i\boldsymbol{k}.\boldsymbol{x}} \psi(\boldsymbol{x}) d\boldsymbol{x}$. The time evolution of the Wigner function for a single particle is given by

$$\frac{\partial f_W(\boldsymbol{r}, \boldsymbol{k}, t)}{\partial t} + \frac{\hbar \boldsymbol{k}}{m} \nabla_{\boldsymbol{r}} f(\boldsymbol{r}, \boldsymbol{k}, t) = \int d\boldsymbol{k'} V_W(\boldsymbol{r}, \boldsymbol{k} - \boldsymbol{k'}) f_W(\boldsymbol{r}, \boldsymbol{k'}, t) \tag{1.13}$$

where $V_W(\boldsymbol{r}, \boldsymbol{k}) = \frac{1}{i\hbar(2\pi)^d} \int d\boldsymbol{r'} \exp(-i\boldsymbol{k}.\boldsymbol{r'}) \Big(V(\boldsymbol{r} + \frac{\boldsymbol{r'}}{2}) - V(\boldsymbol{r} - \frac{\boldsymbol{r'}}{2}) \Big)$. The above description resembles the semi-classical Boltzmann equation (described in section 1.1.2) for the terms on the left-hand side and the quantum corrections are due to the terms on the right-hand side. The Wigner function approach has been used to study electronic transport in resonant tunneling diodes [11, 16, 17, 18] and to study the effects of decoherence [19]. The approach is suitable for studying mesoscopic systems where

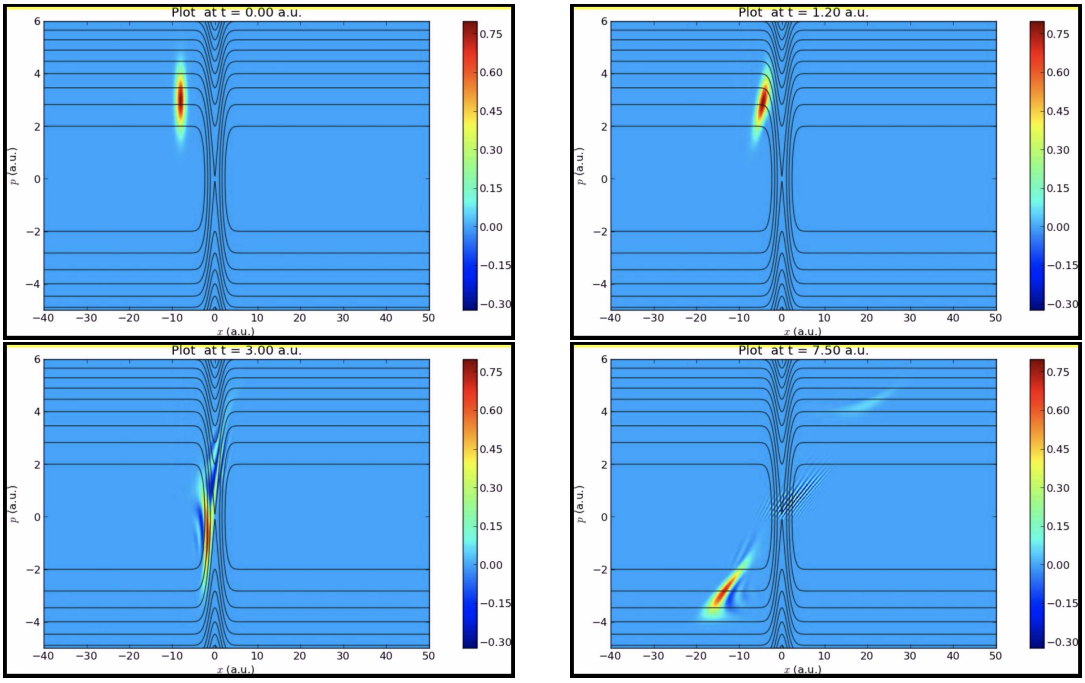

Figure 1.5: The time evolution of the Wigner function through a potential barrier at four instants of time. The solid lines represent the level set of the Hamiltonian $H(x,k) = k^2/2 + V(x)$. (From [20])

the typical dimensions are such that transport cannot be assumed to be totally coherent since dissipative scattering begins to take place. In such conditions, the Schrödinger equation for isolated electrons cannot be used. On the other hand, dimensions are so small that coherent quantum effects are present, and so one cannot justify semi-classical approaches.

1.1.2 Semi-classical transport

Semi-classical theories of transport treat the particle as localized in phase space: particles move through the semiconductor classically scattering with defects, vibrations of the crystal lattice or other electrons. The transition from quantum to semi-classical transport requires introducing decoherence into the time evolution. Wolfgang Pauli, using the time evolution of the density matrix described in Eq. 1.6, attempted to describe how a system driven off-equilibrium approaches thermodynamic equilibrium [21]. If one assumes that at every time step the phases of states

of the system are randomized, then the occupation ρ_i of any eigenstate $|i\rangle$ of the Hamiltonian evolves in time according to the master equation

$$\frac{d\rho_i}{dt} = -\sum_j w_{ij}\rho_i + \sum_j w_{ji}\rho_j \tag{1.14}$$

where w_{ij} is the transition rate from state i to state j, given by the Fermi golden rule

$$w_{ij} = \frac{2\pi}{\hbar}|\langle\Psi_j|\hat{H}_{int}|\Psi_i\rangle|^2\delta(E_j - E_i \pm E_{int}). \tag{1.15}$$

$\hat{H}_{int}$ above refers to the interaction part of the Hamiltonian that causes the transitions between the states i and j. We will use a similar master equation in chapter 4 to model hopping transport in a disordered potential. The above master equation is Markovian, that is without memory. The transition rate w_{ij} at any instant t does not depend on the history of the particle. The dynamics is irreversible, and it describes a particle's approach to equilibrium or steady-state dynamics. Léon Van Hove showed that Eq. 1.14 can be obtained without requiring a randomization of the phases at every time step and can be derived based on making certain assumptions of the number of degrees of the phonons [21, 22] involved in the transitions. The details of the above change from a quantum to semi-classical approach are quite involved and are part of the field of open quantum systems [22].

If one considers that the electronic states involved in the master equation of Eq. 1.14 are delocalized Bloch waves and are therefore indexed by $\boldsymbol{k}$ and $\boldsymbol{k'}$, with the further assumption that the semiconductor sample is composed of many constituent parts where Eq. 1.14 holds, then indexing each of those constituent parts with a spatial coordinate j, one defines the phase space occupation probability$f(\boldsymbol{r_j}, \boldsymbol{k}, t) = \rho^j_{\boldsymbol{k}}$ and the Boltzmann transport equation [21] can be "derived" as

$$\frac{\partial f(\boldsymbol{r},\boldsymbol{k},t)}{\partial t} = -\frac{1}{\hbar}\nabla_{\boldsymbol{k}}E(\boldsymbol{k}).\nabla_{\boldsymbol{r}}f(\boldsymbol{r},\boldsymbol{k},t) + e\nabla_{\boldsymbol{r}}\phi(\boldsymbol{r},t).\nabla_{\boldsymbol{k}}f(\boldsymbol{r},\boldsymbol{k},t) + \Big(\frac{\partial f}{\partial t}\Big)_{collision} \tag{1.16}$$

where $E(\boldsymbol{k})$ refers to the band dispersion, ϕ refers to the electrostatic potential and we have passed into the continuum limit for the spatial coordinates. The collision

term in the above expression is given by

$$\Big(\frac{\partial f}{\partial t}\Big)_{collision} = \sum_{\boldsymbol{k'}} W_{\boldsymbol{k},\boldsymbol{k'}} f(\boldsymbol{r},\boldsymbol{k'},t) - W_{\boldsymbol{k'},\boldsymbol{k}} f(\boldsymbol{r},\boldsymbol{k},t). \tag{1.17}$$

The Boltzmann equation traces the occupation probability of the particles as a function of position and momentum, and treats the scattering process with the different particles such as defects and phonons as collision terms. In the relaxation time approximation, the deviation in the steady-state statistics is considered small as

$$\Big(\frac{\partial f}{\partial t}\Big)_{collision} = \frac{f(\boldsymbol{r},\boldsymbol{k},t) - f_0(\boldsymbol{r},\boldsymbol{k})}{\tau(\epsilon)}, \tag{1.18}$$

where $f_0(\boldsymbol{r},\boldsymbol{k})$ is given by the equilibrium distribution, and $\tau(\epsilon)$ refers to the characteristic scattering rate of the collision process in question at energy ϵ. The above approximation can finally lead to an expression of the familiar Drude mobility [11]

$$\mu = \frac{e}{m}\frac{\langle\tau(\epsilon)\epsilon\rangle}{\langle\epsilon\rangle} \tag{1.19}$$

where $\langle\epsilon\rangle$ is the average energy.

Finally, when simulating semiconductor structures at the device level, say for p-n junctions and transistors, one often uses the drift-diffusion model. One can define statistical averages and moments from the Boltzmann equation to arrive at the hydrodynamic model of transport. The drift-diffusion expression for the current density J is given by

$$J = qn\mu E + qD\nabla n \tag{1.20}$$

where n is the carrier concentration, E is now the electric field, μ is the mobility for the electrons and D is the diffusion constant, the two being related by the Einstein relation $\mu k_B T/q = D$. We will use the drift-diffusion model in chapter 2 to study the electronic transport in the space charge regime.

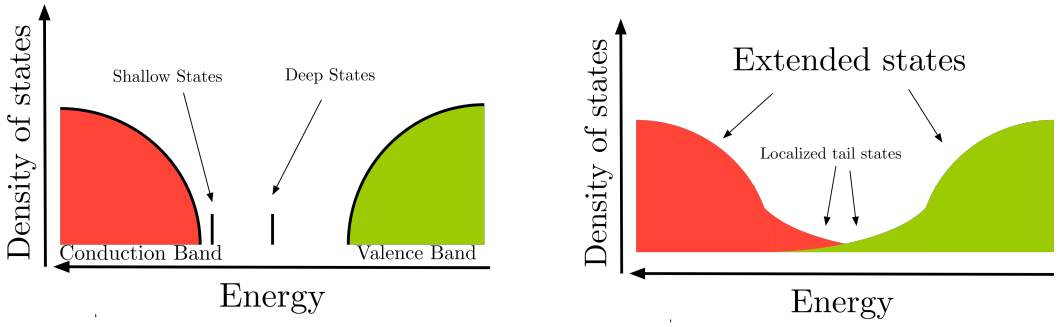

Figure 1.6: a) A schematic of the density of states for a crystalline semiconductor with shallow and deep traps. b) A schematic of the density of states for an amorphous semiconductor where there are now tails of localized states in the gap.

1.2 The role of disorder in semiconductor physics

So far, the transport theories described are quite general, and sometimes they assume that the electronic states are delocalized Bloch waves (for example, the Boltzmann equation). However, as mentioned before, when there is sufficient disorder, the electronic states tend to localize and this can change the transport mechanisms involved and the transport parameters such as the mobility and the diffusion constant.

The simplest kind of disorder one can imagine is a defect in a crystal lattice. The defect is often treated as a slowly varying perturbation $V(\boldsymbol{r})$ to the periodic potential and leads to the creation of an electronic state near the band edge ($10-100\,\text{meV}$) and is called a shallow defect (Fig. 1.6). These states are localized and are used to model dopants introduced in semiconductors which are ultimately responsible for their "semiconducting" nature. Theoretically, they are often treated using the effective mass approximation which involves assuming the wavefunction for the state as a Bloch wave multiplied by an envelope function. The total state is approximated $\psi = u_0 F(\boldsymbol{r})$ where u_0 refers to a Bloch wave for $\boldsymbol{k} \approx 0$ since the slowly varying perturbation is assumed to require only low $\boldsymbol{k}$ to be accounted for and $F(\boldsymbol{r})$ is the envelope function. Such a representation allows us to write an effective Schrödinger equation [23]

$$\Big[-\frac{\hbar^2}{2m^*}\Delta + V(\boldsymbol{r})\Big]F(\boldsymbol{r}) = EF(\boldsymbol{r}). \tag{1.21}$$

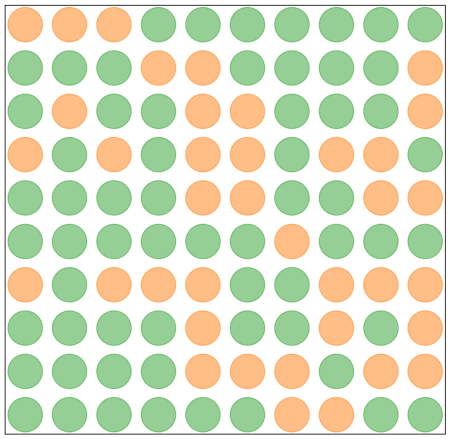

Figure 1.7: A schematic of a crystalline random alloy.

where m^* is now the effective mass of the electron.

However, certain impurities or defects can also introduce electronic states deep within the gap (Fig. 1.6), which are called deep traps. These deep traps can alter the current because they serve as non-radiative recombination centers for electrons and holes, a mechanism known as the *Shockley-Read-Hall* [24] recombination. They enter the current conservation equation through a source-well term in the right-hand side as

$$\nabla.J = qR, \tag{1.22}$$

where R refers to the recombination rate due to the deep traps. We will use this expression to account for recombination effects in chapter 2.

If one considers a more disordered system such as a random alloy, where the material is still crystalline but the atoms are randomly assigned positions (Fig. 1.7), one common approach is the *virtual crystal approximation* [25]. In this method, the alloy is replaced by a weighted average of the two constituent elements such that for an alloy A_xB_{1-x} where x is the composition of element A, the effective virtual potential is $V_0 = xV_A + (1-x)V_B$. Then, for an area of the material where the local concentration varies as x', the fluctuations in the potential are $V - V_0 = (V_A - V_B)(x' - x)$. The RMS deviation of the potential (assumed to be an uncorrelated

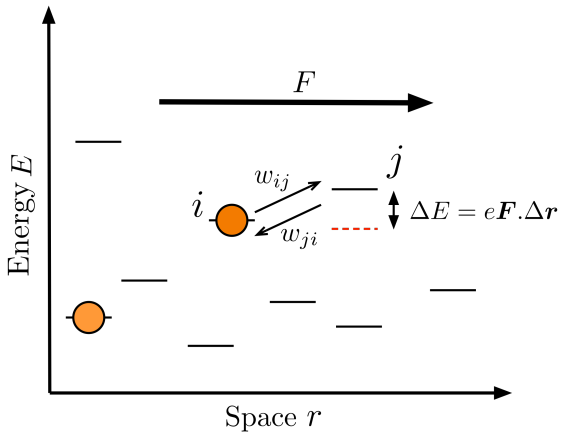

Figure 1.8: A schematic of the hopping states. The presence of a small field F shifts the energy difference between the states by an amount proportional to F.

binary law) is

$$|\langle V - V_0\rangle| \propto |V_A - V_B|\,[x(1-x)]^{1/2}\,. \tag{1.23}$$

The scattering rate, which is proportional to the square of the above quantity then becomes

$$\frac{1}{\tau} \propto |\,\langle \boldsymbol{k}|\langle V - V_0\rangle|\boldsymbol{k}'\rangle\,|^2 \propto |V_A - V_B|^2 x(1-x) \tag{1.24}$$

It can be shown that the mobility for such a material where the transport is still due to extended states is [26]

$$\mu = \frac{\pi^{3/2}}{2\sqrt{2}}\frac{e\hbar^4 N}{|V_A - V_B|^2 x(1-x) m^{*5/2}(k_B T)^{1/2}}. \tag{1.25}$$

The above situation of a random alloy is better treated with the coherent potential approximation (CPA)[27] which involves approximating the Green's function for a disordered alloy.

The above approaches all assume that the transport is due to extended states. The compositional disorder in the system alters the transport as we have seen, but the transport still occurs through the extended states. In the following section, we will describe what occurs when the electronic transport is due to localized states.

Hopping transport occurs when a charge carrier hops between localized electronic states at low enough carrier concentrations and low enough temperatures.

The hops are due to the atomic vibrations of the system, or phonons. Hopping transport through localized states was first studied in the context of impurity states in silicon [28, 29] by Miller and Abrahams. The localized states were described by hydrogen-like wavefunctions of a certain localization length a given as

$$\psi(\boldsymbol{r}) = \sqrt{\frac{1}{\pi a^3}} \exp\left\{-\frac{r}{a}\right\}. \tag{1.26}$$

The hopping rates between each state, which are now commonly referred to as the Miller-Abrahams' rates, are given as

$$w_{ij} = \begin{cases} w_0 \exp\left\{-\dfrac{2r_{ij}}{a} - \dfrac{E_j - E_i}{k_B T}\right\} & \text{if } E_j > E_i \\ w_0 \exp\left\{-\dfrac{2r_{ij}}{a}\right\} & \text{else,} \end{cases} \tag{1.27}$$

where w_{ij} is the hopping rate from state i to state j. One notes that the above expression has two principal contributions, one spatial due to the distance r_{ij} between hopping states, and the other energetic, due to the difference of energies $E_j - E_i$ between the states. In the absence of an electric field, the steady state occupation probabilites are given by the Fermi-Dirac statistics, where the dynamics of the hopping process is governed by a master equation similiar to Eq. 1.14. In the presence of a small electric field F (small compared to the potential responsible for the localization), we assume that the localized states are not altered, and the energies are modified by $e\boldsymbol{F}.\boldsymbol{r}_i$, giving us a net current (Fig. 1.8). At high enough temperatures, the hopping rates are dominated by exponential decay due to the spatial term in Eq. 1.27. Therefore the largest hopping rates are due to the closest hopping centers: this regime is called *nearest-neighbor hopping* [26]. At low enough temperatures, the hopping rate is no longer dominated by the spatial coordinates since the exponential decay of the energy term becomes comparable with the spatial term. This means that although the long range hops at low temperatures are less probable compared to long range hops at higher temperatures, they become more probable than short hops at low temperatures. Therefore, a hop can occur further away than the nearest neighbors, and this regime is called *variable-range hopping*. Overall, the hopping transport is modeled by assuming a certain density of states for the localized states

(usually exponential for inorganic semiconductors and Gaussian for organic semiconductors). Under the assumption of a constant density of states around the Fermi level, we have Mott's law [7] for variable range hopping

$$\sigma(T) \propto \exp\left[-\left(\frac{T_0}{T}\right)^{1/(d+1)}\right], \tag{1.28}$$

where d refers to the dimension of the system, and T_0 is a characteristic temperature of the system which depends on the localization length a and the density of states of the localized states. The above expression reflects the fact that the charge carrier hops in a $d+1$ space, d spatial dimensions and 1 energy dimension. The typical energy difference of a hop $\Delta E \sim R^d N(E_F)$, where R is the distance of the hop and $N(E_F)$ is the density of states at the Fermi level E_F. Inserting this into Eq. 1.27 and finding R that maximizes the hopping rate gives us Mott's law. The above law holds in the absence of interactions between carriers. When the electrostatic interactions between carriers become important, a gap in the density of states is created which is known as the Coulomb gap. The density of states rises quadratically on either side of the gap and gives rise to the Efros–Shklovskii law,

$$\sigma(T) \propto \exp\left[-\left(\frac{\bar{T}_0}{T}\right)^{1/2}\right], \tag{1.29}$$

for all dimensions where $\bar{T}_0$ depends on the dielectric constant of the material and the localization length a. The above results can also be derived through percolation theory [30]. This involves constructing spheres around each state as depicted in Fig. 1.9 and calculating the radius r_c for which one can find a conducting path through the domain as depicted in red in Fig. 1.9. This critical radius r_c helps to determine the transport parameters such as the conductance and mobility. It has also been employed in calculating the mobility for continuum problems or in other words to calculate the percolation levels for a fluctuating potential [8]. Percolation theory has been used to calculate the mobility in amorphous oxide semiconductors of InGaZnO [31].

The Miller-Abrahams' model has been extended to a large variety of systems where transport is believed to occur via localized states [31, 32, 33, 34, 35]. One

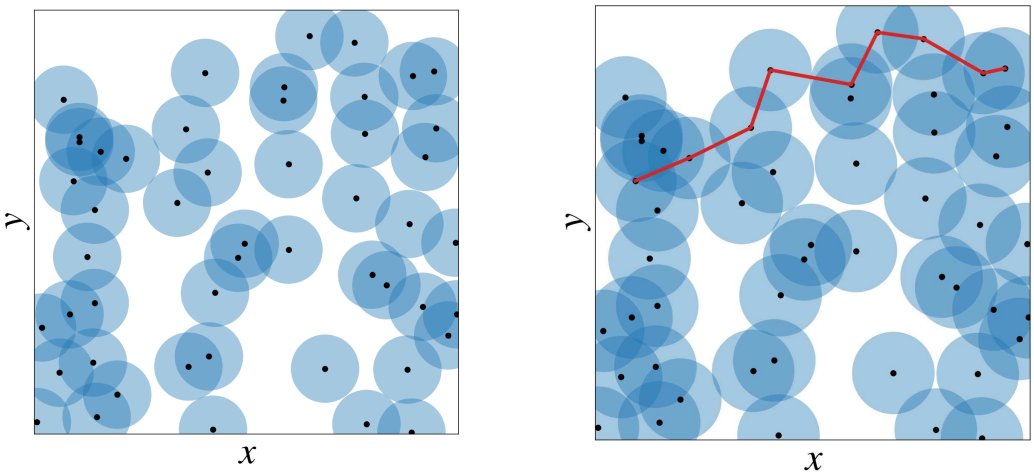

Figure 1.9: a) A hopping network that does not percolate for the chosen radius around each hopping center. b) A hopping network that does percolate with a percolating path drawn in red.

also finds other expressions for the hopping rates such as the Marcus rates, which are often used to describe hopping due to polarons [36, 37]. In chapter 4, we will employ the localization landscape theory to model hopping transport due to localized states.

In the above overview, we have mainly described the effects of static disorder, which is disorder due to random positions of the constituent atoms of a semiconductor, and not due to say, thermal motion of the atoms which is referred to as dynamic disorder [38, 39]. Interactions between electrons [40, 41, 42] can also lead to localization of electronic states, and forms part of the theories of many-body localization. Even in the context of hopping transport, as described above, Coulomb interactions between the charge carries can alter the density of states and conductance.

1.3 Organization of this manuscript

This manuscript deals with electronic transport in semiconductors for two different scales of disorder. In Chapter 2, we describe electronic transport in the space charge regime using the drift-diffusion model for silicon samples. The drift-diffusion equations are coupled with the Poisson equation to account for the electrostatic effect

of charge carriers on the bands, and situations when non-negligible electric fields due to the charge carriers are important is referred to as the space charge regime. We show that the effects of electrostatics and the recombination via deep traps are important to suitably model the current-bias curves in experimental samples.

In Chapter 3, we introduce the previously developed localization landscape (LL) theory and present the main results derived from it. These results and concepts will be useful in the following chapter, where we use the LL theory to address hopping transport between localized states. We present previous work that has been used to model the effects of localization in disordered semiconductors such as InGaN, as well as the recently developed Wigner-Weyl approach with LL theory.

In Chapter 4, we present an LL-based approach to hopping transport. As described above, hopping transport occurs when the electronic states involved in the transport are localized, and the charge carrier therefore hops between localized states, assisted by phonons. In this work, we compare the true Schrödinger equation eigenstates and LL theory based states for computations of the energies, localization lengths, hopping rates and mobilities. We show that this hopping network can actually be visualized with an effective potential derived from the LL theory, and that the coupling between localized states is essentially supported along geodesics of a metric deduced from the effective potential.

In the conclusion, we summarize the findings of this work and examine the possible avenues for future developments of our approach.

References

[1] A. R. Zanatta and I. Chambouleyron. “Absorption Edge, Band Tails, and Disorder of Amorphous Semiconductors”. In: *Phys. Rev. B* 53.7 (Feb. 15, 1996), pp. 3833–3836. ISSN: 0163-1829, 1095-3795. DOI: 10.1103/PhysRevB.53.3833.

[2] D. P. McMahon and A. Troisi. “Organic Semiconductors: Impact of Disorder at Different Timescales”. In: *ChemPhysChem* 11.10 (2010), pp. 2067–2074. ISSN: 1439-7641. DOI: 10.1002/cphc.201000182.

[3] C. Weisbuch et al. "Disorder Effects in Nitride Semiconductors: Impact on Fundamental and Device Properties". In: *Nanophotonics* 10.1 (Nov. 18, 2020), pp. 3–21. ISSN: 2192-8614, 2192-8606. DOI: 10.1515/nanoph-2020-0590.

[4] P. W. Anderson. "Absence of Diffusion in Certain Random Lattices". In: *Physical Review* 109.5 (Mar. 1, 1958), pp. 1492–1505. ISSN: 0031-899X. DOI: 10.1103/PhysRev.109.1492.

[5] *Amorphous Silicon*. In: *Wikipedia*. Aug. 2, 2022.

[6] N. Vukmirović and L.-W. Wang. "Charge Carrier Motion in Disordered Conjugated Polymers: A Multiscale Ab Initio Study". en. In: *Nano Letters* 9.12 (Dec. 2009), pp. 3996–4000. ISSN: 1530-6984, 1530-6992. DOI: 10.1021/nl9021539.

[7] N. F. Mott and E. A. Davis. *Electronic Processes in Non-Crystalline Materials*. Oxford Classic Texts in the Physical Sciences. Oxford, New York: Oxford University Press, Feb. 2, 2012. 608 pp. ISBN: 978-0-19-964533-6.

[8] B. I. Shklovskii and A. L. Efros. *Electronic Properties of Doped Semiconductors*. Red. by M. Cardona, P. Fulde, and H.-J. Queisser. Vol. 45. Springer Series in Solid-State Sciences. Berlin, Heidelberg: Springer Berlin Heidelberg, 1984. ISBN: 978-3-662-02405-8 978-3-662-02403-4. DOI: 10.1007/978-3-662-02403-4.

[9] E. Akkermans and G. Montambaux. *Mesoscopic Physics of Electrons and Photons*. Cambridge: Cambridge University Press, 2007. ISBN: 978-0-521-85512-9. DOI: 10.1017/CBO9780511618833.

[10] R. Kubo. "Statistical-Mechanical Theory of Irreversible Processes. I. General Theory and Simple Applications to Magnetic and Conduction Problems". In: *J. Phys. Soc. Jpn.* 12.6 (June 15, 1957), pp. 570–586. ISSN: 0031-9015. DOI: 10.1143/JPSJ.12.570.

[11] C. Jacoboni. *Theory of Electron Transport in Semiconductors*. Vol. 165. Springer Series in Solid-State Sciences. Berlin, Heidelberg: Springer Berlin Heidelberg, 2010. ISBN: 978-3-642-10585-2 978-3-642-10586-9. DOI: 10.1007/978-3-642-10586-9.

[12] S. Ciuchi, S. Fratini, and D. Mayou. "Transient Localization in Crystalline Organic Semiconductors". In: *Phys. Rev. B* 83.8 (Feb. 23, 2011), p. 081202. ISSN: 1098-0121, 1550-235X. DOI: 10.1103/PhysRevB.83.081202.

[13] F. Ortmann, F. Bechstedt, and K. Hannewald. "Theory of charge transport in organic crystals: Beyond Holstein's small-polaron model". en. In: *Physical Review B* 79.23 (June 2009), p. 235206. ISSN: 1098-0121, 1550-235X. DOI: 10.1103/PhysRevB.79.235206.

[14] E. Wigner. "On the Quantum Correction For Thermodynamic Equilibrium". In: *Physical Review* 40.5 (June 1932), pp. 749–759. DOI: 10.1103/PhysRev.40.749.

[15] M. Hillery et al. "Distribution Functions in Physics: Fundamentals". In: *Physics Reports* 106.3 (Apr. 1, 1984), pp. 121–167. ISSN: 0370-1573. DOI: 10.1016/0370-1573(84)90160-1.

[16] N. C. Kluksdahl et al. "Self-Consistent Study of the Resonant-Tunneling Diode". In: *Phys. Rev. B* 39.11 (Apr. 15, 1989), pp. 7720–7735. DOI: 10.1103/PhysRevB.39.7720.

[17] W. R. Frensley. "Wigner-Function Model of a Resonant-Tunneling Semiconductor Device". In: *Phys. Rev. B* 36.3 (July 15, 1987), pp. 1570–1580. DOI: 10.1103/PhysRevB.36.1570.

[18] U. Ravaioli et al. "Investigation of Ballistic Transport through Resonant-Tunnelling Quantum Wells Using Wigner Function Approach". In: *Physica B+C* 134.1 (Nov. 1, 1985), pp. 36–40. ISSN: 0378-4363. DOI: 10.1016/0378-4363(85)90317-1.

[19] D. Querlioz and P. Dollfus. *The Wigner Monte Carlo Method for Nanoelectronic Devices: A Particle Description of Quantum Transport and Decoherence*. Wiley, May 3, 2010. 256 pp. ISBN: 978-1-84821-150-6. Google Books: _uuZQQAACAAJ.

[20] *File:Wigner Function for Tunnelling.Ogv - Wikipedia*. URL: https://commons.wikimedia.org/wiki/File:Wigner_function_for_tunnelling.ogv (visited on 10/28/2022).

[21] M. V. Fischetti and W. G. Vandenberghe. *Advanced Physics of Electron Transport in Semiconductors and Nanostructures*. Graduate Texts in Physics. Cham: Springer International Publishing, 2016. ISBN: 978-3-319-01100-4 978-3-319-01101-1. DOI: 10.1007/978-3-319-01101-1.

[22] H.-P. Breuer and F. Petruccione. *The Theory of Open Quantum Systems*. Oxford ; New York: Oxford University Press, 2002. 625 pp. ISBN: 978-0-19-852063-4.

[23] T. Ihn. "Envelope Functions and Effective Mass Approximation". In: *Semiconductor Nanostructures: Quantum States and Electronic Transport*. Ed. by T. Ihn. Oxford University Press, Nov. 26, 2009, p. 0. ISBN: 978-0-19-953442-5. DOI: 10.1093/acprof:oso/9780199534425.003.0004.

[24] W. Shockley and W. T. Read. "Statistics of the Recombinations of Holes and Electrons". en. In: *Physical Review* 87.5 (Sept. 1952), pp. 835–842. ISSN: 0031-899X. DOI: 10.1103/PhysRev.87.835.

[25] B. K. Ridley. *Quantum Processes in Semiconductors*. Fifth Edition. Oxford, New York: Oxford University Press, Aug. 8, 2013. 450 pp. ISBN: 978-0-19-967722-1.

[26] S. Baranovskii and O. Rubel. "Charge Transport in Disordered Materials". In: *Springer Handbook of Electronic and Photonic Materials*. Ed. by S. Kasap and P. Capper. Cham: Springer International Publishing, 2017, pp. 1–1. ISBN: 978-3-319-48931-5 978-3-319-48933-9. DOI: 10.1007/978-3-319-48933-9_9.

[27] B. Velický. "Theory of Electronic Transport in Disordered Binary Alloys: Coherent-Potential Approximation". In: *Phys. Rev.* 184.3 (Aug. 15, 1969), pp. 614–627. ISSN: 0031-899X. DOI: 10.1103/PhysRev.184.614.

[28] A. Miller and E. Abrahams. "Impurity Conduction at Low Concentrations". In: *Phys. Rev.* 120.3 (Nov. 1, 1960), pp. 745–755. ISSN: 0031-899X. DOI: 10.1103/PhysRev.120.745.

[29] T. Kasuya and S. Koide. "A Theory of Impurity Conduction. II". In: *Journal of the Physical Society of Japan* 13.11 (1958), pp. 1287–1297. DOI: 10.1143/JPSJ.13.1287.

[30] V. Ambegaokar, B. I. Halperin, and J. S. Langer. "Hopping Conductivity in Disordered Systems". In: *Phys. Rev. B* 4.8 (Oct. 15, 1971), pp. 2612–2620. ISSN: 0556-2805. DOI: 10.1103/PhysRevB.4.2612.

[31] A. V. Nenashev et al. "Percolation Description of Charge Transport in Amorphous Oxide Semiconductors". In: *Phys. Rev. B* 100.12 (Sept. 12, 2019), p. 125202. ISSN: 2469-9950, 2469-9969. DOI: 10.1103/PhysRevB.100.125202.

[32] J. O. Oelerich et al. "Field Dependence of Hopping Mobility: Lattice Models against Spatial Disorder". In: *Phys. Rev. B* 96.19 (Nov. 21, 2017), p. 195208. ISSN: 2469-9950, 2469-9969. DOI: 10.1103/PhysRevB.96.195208.

[33] W. F. Pasveer et al. "Unified Description of Charge-Carrier Mobilities in Disordered Semiconducting Polymers". In: *Phys. Rev. Lett.* 94.20 (May 23, 2005), p. 206601. ISSN: 0031-9007, 1079-7114. DOI: 10.1103/PhysRevLett.94.206601.

[34] S. D. Baranovskii et al. "Charge-Carrier Transport in Disordered Organic Solids". In: *Phys. Rev. B* 62.12 (Sept. 15, 2000), pp. 7934–7938. DOI: 10.1103/PhysRevB.62.7934.

[35] M. C. J. M. Vissenberg and M. Matters. "Theory of the Field-Effect Mobility in Amorphous Organic Transistors". In: *Phys. Rev. B* 57.20 (May 15, 1998), pp. 12964–12967. DOI: 10.1103/PhysRevB.57.12964.

[36] H. Oberhofer, K. Reuter, and J. Blumberger. "Charge Transport in Molecular Materials: An Assessment of Computational Methods". en. In: *Chemical Reviews* 117.15 (Aug. 2017), pp. 10319–10357. ISSN: 0009-2665, 1520-6890. DOI: 10.1021/acs.chemrev.7b00086.

[37] R. P. Fornari, J. Aragó, and A. Troisi. "A Very General Rate Expression for Charge Hopping in Semiconducting Polymers". In: *The Journal of Chemical Physics* 142.18 (May 14, 2015), p. 184105. ISSN: 0021-9606, 1089-7690. DOI: 10.1063/1.4920945.

[38] A. Troisi, D. L. Cheung, and D. Andrienko. "Charge Transport in Semiconductors with Multiscale Conformational Dynamics". en. In: *Physical Review Letters* 102.11 (Mar. 2009), p. 116602. ISSN: 0031-9007, 1079-7114. DOI: 10.1103/PhysRevLett.102.116602.

[39] A. Troisi and D. L. Cheung. "Transition from dynamic to static disorder in one-dimensional organic semiconductors". en. In: *The Journal of Chemical Physics* 131.1 (July 2009), p. 014703. ISSN: 0021-9606, 1089-7690. DOI: 10.1063/1.3167406.

[40] A. L. Efros and B. I. Shklovskii. "Coulomb Gap and Low Temperature Conductivity of Disordered Systems". In: *J. Phys. C: Solid State Phys.* 8.4 (Feb. 21, 1975), pp. L49–L51. ISSN: 0022-3719. DOI: 10.1088/0022-3719/8/4/003.

[41] T. Giamarchi and H. J. Schulz. "Anderson localization and interactions in one-dimensional metals". en. In: *Physical Review B* 37.1 (Jan. 1988), pp. 325–340. ISSN: 0163-1829. DOI: 10.1103/PhysRevB.37.325.

[42] P. Sierant, D. Delande, and J. Zakrzewski. "Many-body localization due to random interactions". en. In: *Physical Review A* 95.2 (Feb. 2017), p. 021601. ISSN: 2469-9926, 2469-9934. DOI: 10.1103/PhysRevA.95.021601.

Chapter 2

Electronic transport in the space charge regime

In the previous chapter, we briefly introduced the semi-classical drift-diffusion equations for electrons. The drift-diffusion equations are often used to model electronic transport in devices such as transistors and we can define two such equations for electrons and holes respectively,

$$J_n = q\mu_n nE + qD_n \nabla n, \tag{2.1}$$

$$J_p = q\mu_p pE - qD_p \nabla p, \tag{2.2}$$

where J_n, J_p are the electron and hole current densities, μ_n, μ_p are the electron and hole mobilities, D_n, D_p are the electron and hole diffusion constants, n, p are the electron and hole concentrations and E is the electric field. The presence of defects can induce localized states deep in the gap, and these can serve as recombination centers. Recombination enters the current conservation equations by introducing a source/sink term as,

$$\nabla \cdot J_n = -qR, \tag{2.3}$$

$$\nabla \cdot J_p = qR, \tag{2.4}$$

where R is the recombination rate for electrons and holes. In this chapter, we are interested in a regime of transport where the dominant carrier type can potentially

change, and when significant non-equilibrium carriers are injected via the contacts giving rise to non-negligible internal electric fields within the conducting medium. Therefore, one must also account for the electric potential via Poisson's equation,

$$-\nabla^2\psi = \frac{q}{\epsilon_r\epsilon_0}(p - n + C). \tag{2.5}$$

In the above equation, ψ is the electric potential, ϵ_0 is the permittivity of vacuum, and ϵ_r is the relative permittivity of the medium in question. The right hand side of Poisson's equation consists of the global charge density and is the sum of holes density p, electron density n and the ionized dopant concentration C. These terms usually balance each other in conductors so as to ensure electrical neutrality within the bulk. However, in the case of very large biases or in interface regions between different materials or doping concentration, this is not necessarily true. The *space charge regime* thus refers to a situation in electronic transport when the right hand side of Poisson's equation is not zero.

Space charge-limited currents were first studied in the context of vacuum tubes to explain the current measured when a potential difference was applied across the two electrodes [1]. I-V curves for the cathode-anode system vary as $I \propto V^{\frac{3}{2}}$ and this dependence is known as Child's law. An analogous situation can arise in insulators [2] and semiconductors [3] when the intrinsic carrier density is low, and a high number of carriers are injected through the contacts. I-V curves in this situation would scale as $I \propto V^2$ a case known as the Mott-Gurney limit [4].

The development of organic semiconductors has given rise to a renewed interest in space charge limited transport because conduction in organic semiconductors depends critically on injection of carriers through the contacts [5, 6, 7, 8]. Another area where one observes space charge limited currents is in semiconductor nanostructures. For devices such as nano-wires, the dimensions of the device itself can often be smaller than the surface depletion layer width [9]. This depletion layer in such nanostructures, i.e., the region where there is a lack of free charge carriers, is formed due to the presence of surface defects. Large surface to volume ratios in nanostructures can cause strong surface effects such as band bending and the formation of depletion regions larger than the size of the devices themselves [10].

In this chapter, we will study electronic transport in the space charge regime by

numerically solving the drift-diffusion equations coupled with the Poisson equation in two cases. First we will study the behavior without recombination, and then we will include the effects of recombination. We will then apply this model to interpret the experimental results on piezoresistive silicon.

2.1 Transport model and numerical results

We numerically solve the current equations and Poisson's equation (Eqs. 2.1-2.5) introduced above in 1D. When an external potential is applied across a semiconductor, the electron and holes are no longer in equilibrium with each other and a unique Fermi level can no longer be defined. However, if one assumes a local equilibrium for each of the carriers, one can define quasi-Fermi potentials φ_n, φ_p for electrons and holes respectively. These quasi-Fermi potentials along with the electrostatic potential ψ can be used to write down the expressions for the current,

$$J_n = -q\mu_n n(\psi, \varphi_n)\frac{d}{dx}\varphi_n, \tag{2.6}$$

$$J_p = -q\mu_p p(\psi, \varphi_p)\frac{d}{dx}\varphi_p, \tag{2.7}$$

where the gradient of the quasi-Fermi level simultaneously accounts for the drift currents due to an electric field and the diffusive currents due to a concentration gradient. The current conservation equations can also be written as,

$$\frac{dJ_n}{dx} = -qR(\psi, \varphi_p, \varphi_n), \tag{2.8}$$

$$\frac{dJ_p}{dx} = qR(\psi, \varphi_p, \varphi_n), \tag{2.9}$$

where R is the recombination rate for electrons and holes as mentioned before. Strictly speaking the statistics of electrons and holes are given by the Fermi-Dirac statistics. If the quasi-Fermi levels are sufficiently far from the band edges, one can use the Maxwell-Boltzmann approximation to evaluate the electron and hole densities as

$$n(\psi, \varphi_n) = N_c \exp\left(\frac{q(\psi - \varphi_n) - E_c}{k_B T}\right) \tag{2.10}$$

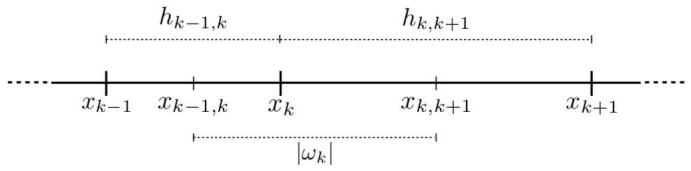

Figure 2.1: 1D discretization around the kth node along with the corresponding notation, from [11]

$$p(\psi, \varphi_p) = N_v \exp\left(\frac{q(\varphi_p - \psi) + E_v}{k_B T}\right) \tag{2.11}$$

where N_c, N_v are the density of states of the conduction and valence band respectively, E_c, E_v are the positions of the band edges of the conduction and valence band respectively.

2.1.1 Finite difference discretization

Since we are dealing with a 1D system, it is relatively simple to discretize the domain. We split the domain into $N+1$ points and define the quantities of interest on each of these $N+1$ points $\{x_0, x_1, x_2..x_N\}$, namely $\psi(x_k)$, $C(x_k)$, $n(x_k)$, $p(x_k)$ as shown in Fig 2.1. Integrating Poisson's equation over the discretization length $\Delta x_k = \omega_k$, we get

$$-\epsilon_r\epsilon_0\left(\frac{d}{dx}\psi\bigg|_{x_{k,k+1}} - \frac{d}{dx}\psi\bigg|_{x_{k-1,k}}\right) = q\left(C_k + p(\psi_k, \varphi_{p;k}) - n(\psi_k, \varphi_{n;k})\right)|\omega_k|. \tag{2.12}$$

Discretizing the derivatives in the above equation gives

$$\begin{aligned} -\epsilon_0\epsilon_r\left(\frac{1}{h_{k,k+1}}\psi_{k+1} - \left[\frac{1}{h_{k,k+1}} + \frac{1}{h_{k-1,k}}\right]\psi_k + \frac{1}{h_{k-1,k}}\psi_{k-1}\right) \\ = q\left(C_k + p(\psi_k, \varphi_{p;k}) - n(\psi_k, \varphi_{n;k})\right)|\omega_k|. \end{aligned} \tag{2.13}$$

Repeating a similar procedure for the current conservation equations gives us

$$j_{n;k,k+1}(\psi_k, \psi_{k+1}, \varphi_{n;k}, \varphi_{n;k+1}) - j_{n;k-1,k}(\psi_{k-1}, \psi_k, \varphi_{n;k-1}, \varphi_{n;k}) = qR(\psi_k, \varphi_{n;k}, \varphi_{p;k})|\omega_k|, \tag{2.14}$$

and

$$j_{p;k,k+1}(\psi_k,\psi_{k+1},\varphi_{p;k},\varphi_{p;k+1})-j_{p;k-1,k}(\psi_{k-1},\psi_k,\varphi_{p;k-1},\varphi_{p;k}) = -qR(\psi_k,\varphi_{n;k}.\varphi_{p;k})|\omega_k|, \tag{2.15}$$

where,

$$j_{n;k,l} = \frac{\mu_n k_B T}{h_{k,l}}\left[B\Big(-\frac{q(\psi_l-\psi_k)}{k_BT}\Big)n_k - B\Big(\frac{q(\psi_l-\psi_k)}{k_BT}\Big)n_l\right], \tag{2.16}$$

$$j_{p;k,l} = \frac{\mu_p k_B T}{h_{k,l}}\left[B\Big(\frac{q(\psi_l-\psi_k)}{k_BT}\Big)p_k - B\Big(-\frac{q(\psi_l-\psi_k)}{k_BT}\Big)p_l\right]. \tag{2.17}$$

$B(x)$ in the Eqs. 2.16- 2.17 is the Bernoulli function $B(x) = x/\left[\exp(x)-1\right]$. The above discretization scheme was proposed by Scharfetter and Gummel [12] [11], and it constitutes a system of equations that can be solved using the Newton-Raphson method, by ensuring convergence and conservation of currents (described in appendix 2.A). Furthermore, we simulate metallic contacts with boundary conditions that impose local charge neutrality for Poisson's equation,

$$\psi_1 = \psi_0(0) + U_1 \quad \text{and} \quad \psi_N = \psi_0(L) + U_2, \tag{2.18}$$

$$\varphi_{n;1} = U_1 \quad \text{and} \quad \varphi_{n;N} = U_2, \tag{2.19}$$

$$\varphi_{p;1} = U_1 \quad \text{and} \quad \varphi_{p;N} = U_2, \tag{2.20}$$

where ψ_0 represents the potential that imposes local charge neutrality everywhere, and $U_2 - U_1$ is the applied potential bias.

2.1.2 Results

We simulated a p-i-p nanostructure of length 100 µm as depicted in Fig. 2.3. The p-type silicon contacts were modeled as being 10 µm and the intrinsic (i-type) silicon was 80 µm in length. We choose such a structure since it is relevant to the study of nanostructures, as we will see in experiments described in Sec. 2.2.

First, we look at transport in the absence of recombination. The I-V plots in logarithmic scale (Fig 2.4) show the presence of an initial linear regime, followed by an asymptotic onset of a quadratic Mott-Gurney law. As examples, the quasi Fermi potentials along with the conduction and valence bands are plotted for 0.1 V and

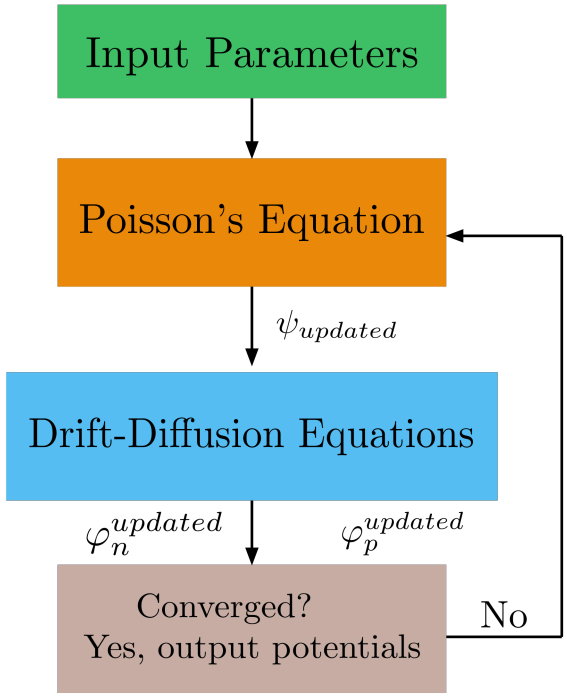

Figure 2.2: Flowchart for the computer program implementing the solver

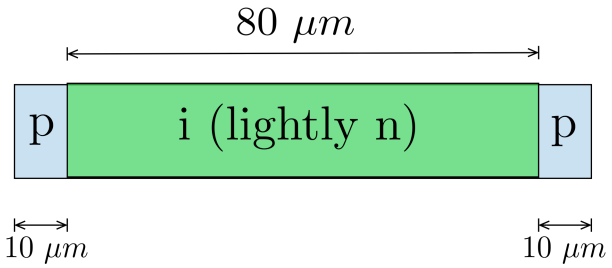

Figure 2.3: Representation of the p-i-p sample used in the simulations. The thickness of the sample t was 2 µm and the the width w was 100 µm.

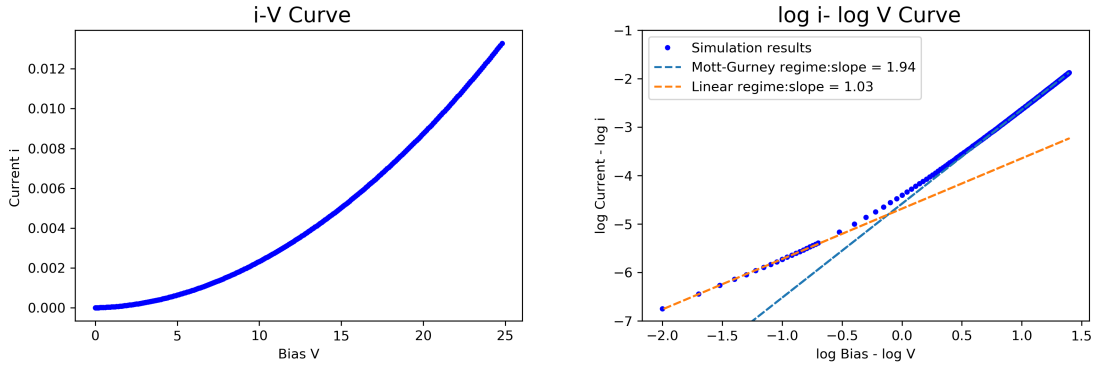

(a) The I-V curve

(b) log I-log V plot

Figure 2.4: Simulated I-V curve (a) and I-V curve in logarithmic scale (b) for the p-i-p structure in the absence of recombination. In this case, the currents are only carried by holes. In the log-log graph (b) we observe an initial linear regime till about 0.5 V and the onset of a quadratic regime from about 3 V. (Arbitrary units are used for the current in both plots.)

10 V in Fig 2.5. Our simulation results correspond to the expected behavior of a p-i-p sample according to previous numerical studies on the p-i-p structure in the absence of recombination [13].

The Mott-Gurney limit can be explained easily if one assumes a single type of carrier, electrons or holes (unipolar situation) and if one ignores the diffusion term while keeping only the drift term in the expression for current. Writing Poisson's equation and the expression for current in 1D, we have,

$$\frac{dE(x)}{dx} = -\frac{q}{\epsilon_r \epsilon_0} p(x), \tag{2.21}$$

$$J(x) = q\mu_p p(x) E(x). \tag{2.22}$$

In the absence of recombination, current conservation $\frac{dJ(x)}{dx} = 0$, gives us a current density independent of position, $J(x) = J$. The above equations can be simplified to give the following differential equation,

$$\frac{dE(x)}{dx} = -\frac{J}{\mu_p \epsilon_r \epsilon_0 E(x)}, \tag{2.23}$$

which when solved for the boundaries at $x = 0$ and $x = L$ with an applied bias of

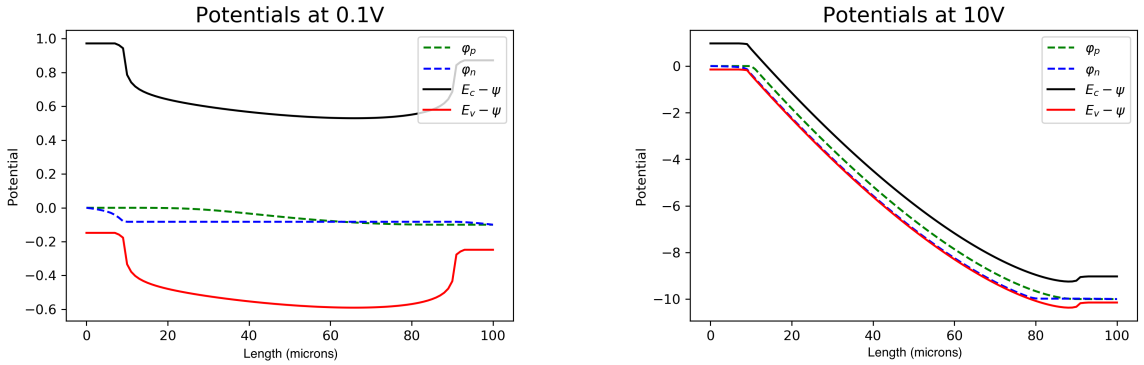

(a) 0.1 V (b) 10 V

Figure 2.5: The simulated quasi Fermi potentials at 0.1 V (a) and 10 V (b).

V gives

$$J = \frac{9}{8}\frac{\mu_p \epsilon_0 \epsilon_r}{L^3} V^2, \tag{2.24}$$

which is the Mott-Gurney result.

Recombination models

In this section, we consider the effects of recombination on the transport. To better study this, we set the intrinsic region of the p-i-p samples to be slightly n doped ($10^{13} - 10^{14}$ cm^{-3}) so as to introduce electrons into the system. The recombination term R in the current equations 2.8 -2.9 can be written as a function of the quasi Fermi potentials and carrier concentrations as follows [14],

$$R(n,p) = r(n,p)np\Big[1 - \exp\left(\frac{q\varphi_n - q\varphi_p}{k_B T}\right)\Big]. \tag{2.25}$$

where $r(n,p)$ is a model-dependent generation-recombination rate. In the Maxwell-Boltzmann approximation, this can be rewritten as

$$R(n,p) = r(n,p)(np - N_{int}^2), \tag{2.26}$$

where N_{int} is the intrinsic carrier concentration, and is given by $N_{int}^2 = N_c N_v e^{\frac{-E_g}{kT}}$. We have implemented three common types of recombination processes: spontaneous radiative recombination, Shockley-Read-Hall (SRH) recombination, and Auger re-

combination.

- The spontaneous radiative recombination rate is

$$R_{spont} = r_{spont}(np - N_{int}^2), \tag{2.27}$$

  where $r_{spont} = 10^{-14}$ cm^{3}s^{-1} for silicon.

- The SRH recombination rate is

$$R_{SRH} = \frac{1}{\tau_p(n + n_T) + \tau_n(p + p_T)}(np - N_{int}^2), \tag{2.28}$$

  where τ_p, τ_n are the characteristic recombination times for holes and electrons. E_T is the trap energy, located 0.44 eV below the conduction band, and p_T is the density of trapped carriers : $E_T = E_c - 0.44\,\text{eV}$, $p_T = N_v e^{-(E_t - E_v)/kT}$ and $n_T = N_c e^{-(E_c - E_t)/kT}$. (We set E_T as such because this is the relevant energy for the implanted defects in the silicon samples studied in section 2.2). For the biases considered in our simulations, the dominant recombination mechanism was the SRH type recombination.

- The Auger recombination rate

$$R_{Aug} = (C_n n + C_p p)(np - N_{int}^2), \tag{2.29}$$

  where $C_n = 0.11 \times 10^{-29}$ cm^{6}s^{-1} and $C_p = 0.03 \times 10^{-29}$ cm^{6}s^{-1} are the Auger coefficients for silicon.

The above described modifications change the behavior of the I-V curves significantly. We no longer see a linear regime followed by an asymptotic quadratic regime. The I-V curve in logarithmic scale (Fig. 2.6) now shows an initial $\sqrt{V}$ dependence up to about 25 V, then the current increases rapidly around 40 V, and shifts to a cubic dependence at 100 V. We were unable to find any simple physical explanation for the square-root and cubic dependence of the I-V curve. We are now able to observe a switch from bipolar transport at low bias to unipolar hole transport at high biases, and the rapid increase around 40 V corresponds to a situation where

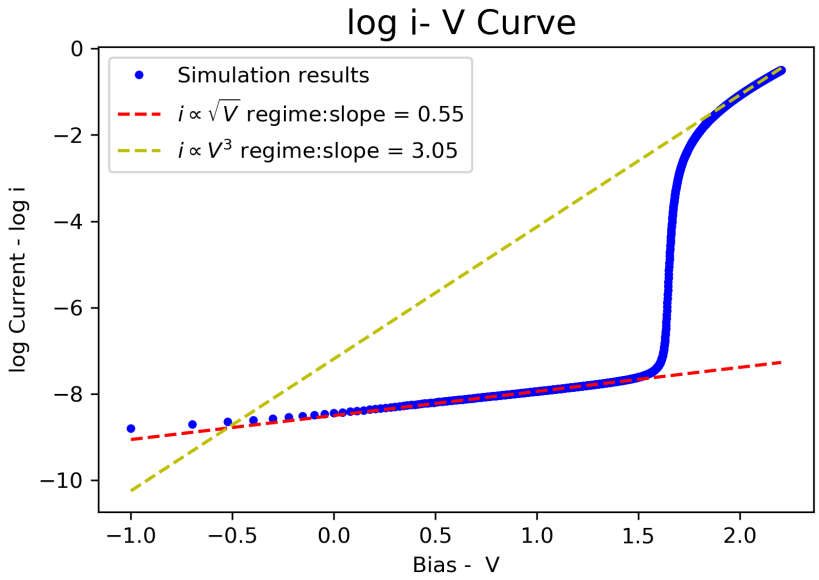

Figure 2.6: Simulated I-V curve in log scale for the p-i (weakly n)-p structure in the presence of recombination. SRH recombination is the dominant mechanism and the Shockley recombination parameters (as defined in section 2.1.2) $\tau_p = \tau_n = 10^{-7}$s with $E_T = E_c - 0.44\,\text{eV}$. The plot shows an initial $\sqrt{V}$ dependence, followed by a sharp increase at 40 V. We see the onset of V^3 dependence at 100 V.

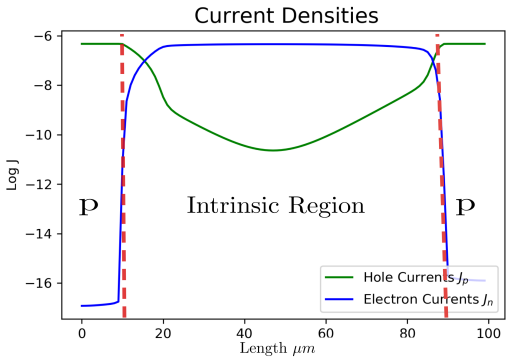

(a) 1 V

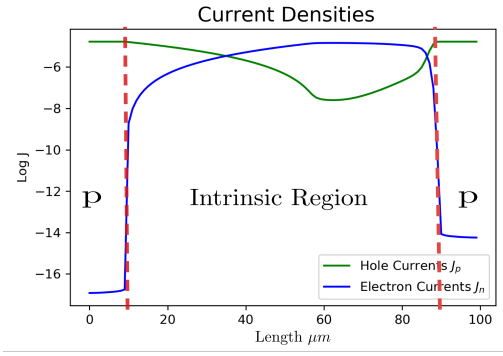

(b) 20 V

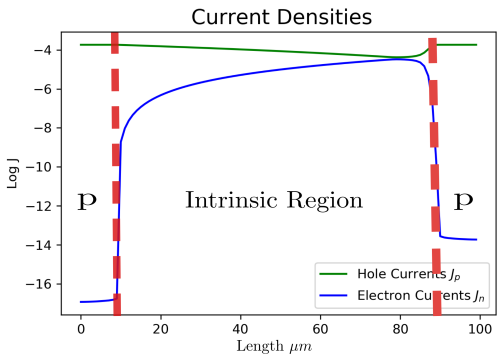

(c) 40 V

Figure 2.7: The electron and hole currents plotted as function of position x on the sample, for three different biases. In the intrinsic region, from 10 to 90 µm, we observe a transition in majority currents from electrons to holes, and the shift occurs for a bias of about 40 V. At the p-type ohmic contacts, it is always hole currents that dominate. (Arbitrary units are used for the current in all plots.)

the hole currents begin to dominate the electron currents across the entire intrinsic region (Fig 2.7).

Our simulations show that at all biases, hole currents dominate at the contacts because these are heavily p-doped compared to the intrinsic region of the p-i-p sample. However, at low biases, holes injected from the p-type contacts recombine with electrons when they enter the intrinsic region as can be seen in Fig. 2.8. As a result, electrons dominate the currents in the intrinsic region at low biases. When these electrons leave the intrinsic region, they recombine with the majority holes at the contacts, and so no electron current persists at the contacts. As the bias increases,

the injected holes begin to dominate the electrons despite the recombination, since they outnumber the electrons. We observe how the holes pervade into the intrinsic region in Fig. 2.8.

Furthermore, we noticed that the ability to observe the transition from electron currents to hole currents depends importantly on the Shockley Read Hall recombination parameters, namely the τ_p and τ_n, where $\tau_p = \tau_n = 10^{-7}$ s. Varying these time constants can change the ratio of electron to hole currents in the intrinsic region. For example, if τ_p and τ_n are much larger, say around 10^{-3} s, which is the experimentally measured value for intrinsic silicon in the weak injection limit, the electron currents are always lower than the hole currents at all biases. In addition, it is possible to shift the voltage at which the switch is observed by suitably varying these time constants. It is important to point out that τ_p, τ_n in the original Shockley-Read paper [15] are assumed independent of the concentrations, an assumption that breaks down in the space charge regime because the concentrations can vary quite dramatically, as can be seen in Fig. 2.9.

Finally, Fig. 2.10 suggests that the rapid increase in the current at a certain threshold voltage is purely a consequence of the electrostatics and not due to traps. This is because the p-i(weakly n) -p without recombination is qualitatively very similar to the p-i(weakly n)-p with recombination.

2.2 Experiments on piezoresistive silicon

In this section, we will use the numerical results developed above to interpret experimental observations in piezoresistive silicon. This work contributed in the publication of a paper titled "Piezoresistance in Defect-Engineered Silicon" [16]. Piezoresistance (PZR) is the change in electrical resistivity ρ of a solid due to a mechanical stress. One way to characterize this piezoresistive effect is by defining the π coefficient as a function of the applied stress (X),

$$\pi = \frac{\Delta\rho}{\rho}\frac{1}{X}. \tag{2.30}$$

The value of π depends both on the crystal axis along which the stress is applied and on the axis along which the resistance is measured, and is therefore a tensor.

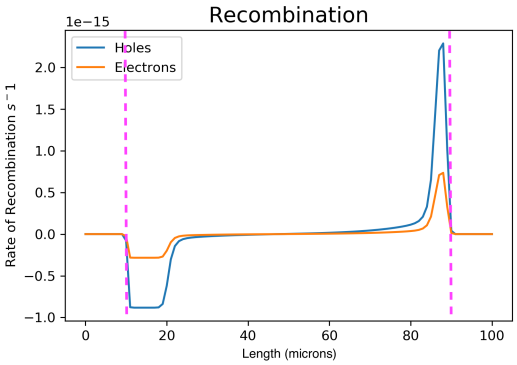

(a) 1 V

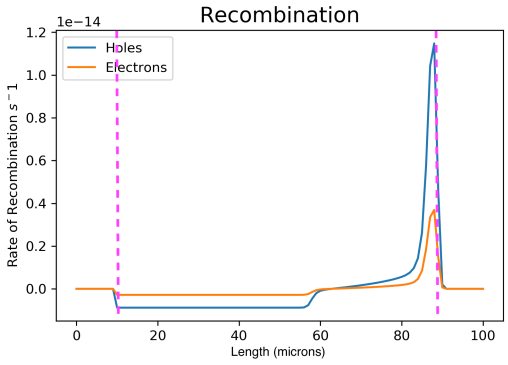

(b) 20 V

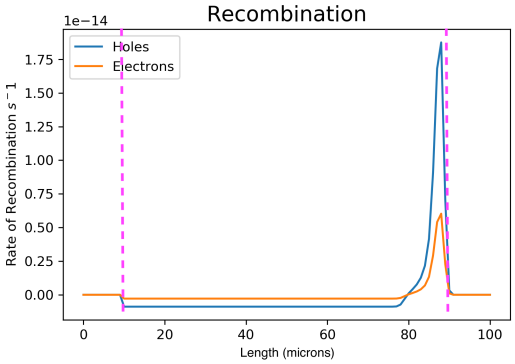

(c) 40 V

Figure 2.8: Recombination rates plotted for holes and electrons as a function of position x on the sample. It can be seen that recombination occurs at the interface between the contacts and the intrinsic region. Holes injected from the contacts into the intrinsic region recombine with electrons, and electrons that overcome the potential barrier recombine with holes at the right contact. This recombination pervades into the intrinsic region as the bias is increased.

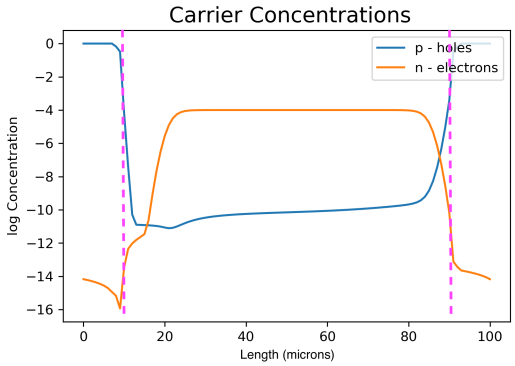

(a) 1 V

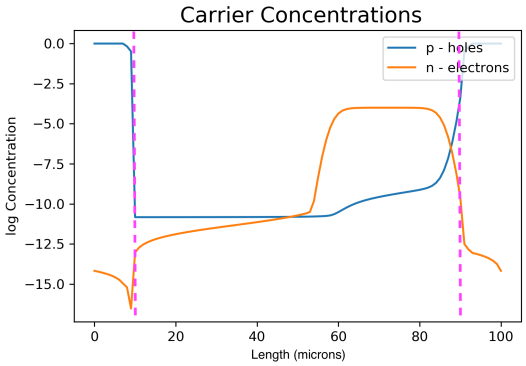

(b) 20 V

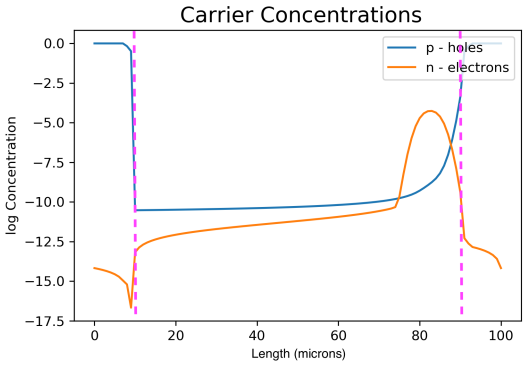

(c) 40 V

Figure 2.9: Concentrations plotted for holes and electrons as a function of position x on the sample. The relative concentrations can vary quite dramatically depending on the bias and the number of injected carriers, suggesting that recombination models that do not account for these varying concentrations would be erroneous.

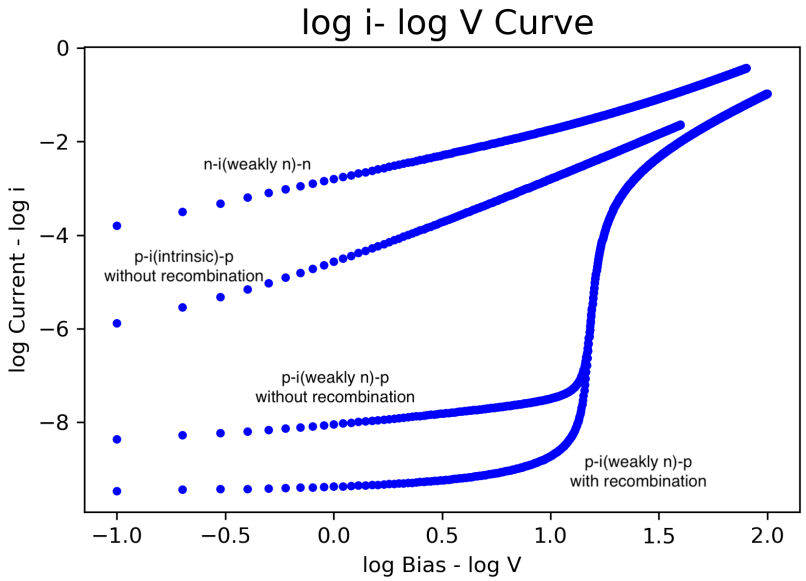

Figure 2.10: The I-V curves for different doping profiles as labeled. We observe that recombination is not required to have qualitatively similar behavior as is observed experimentally (Fig. 2.11), which can be attributed to the electrostatics. However, recombination does adjust the value of the currents in electron current regime. (Arbitrary units are used for the current.)

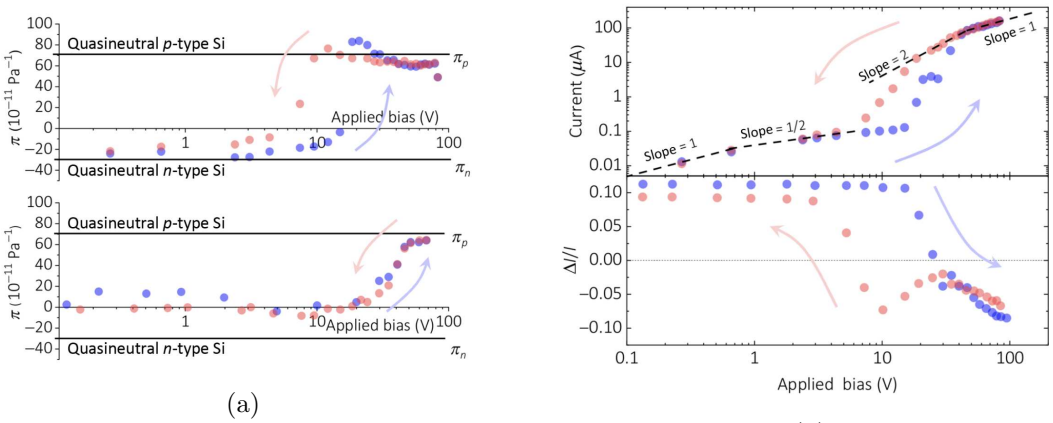

(a) (b)

Figure 2.11: a) PZR π coefficient measured under 20 MPa of uniaxial tensile stress parallel to the applied current along the $\langle 110 \rangle$ crystal direction. Up (blue circles and arrow) and down (red circles and arrow) sweeps are shown. (Top) Results from the defect-engineered sample whose characteristics are shown in Fig. 4. Near a threshold voltage, π changes sign and is approximately bounded by the known bulk silicon values. (Bottom) Results for a device prior to defect engineering. No anomalous (negative) PZR is observed. Note also that the hysteresis is only present in defect-engineered devices. b) (Top) Experimentally measured up-(blue circles and arrow) and down-(red circles and arrow) sweep current-voltage characteristics obtained on the defect engineered devices. The slopes indicated in the log-log plot are a guide to the eye. (Bottom) Relative current change induced by a +1 V change in the voltage applied to the wafer handle. The sign indicates a majority electron current below a threshold voltage and a majority hole current above this bias. A hysteresis in the threshold voltage is clearly visible between the up and down sweeps. (Figures from [16].)

Bulk silicon has a known PZR of $\pi_{<100>} = 6.6 \times 10^{-11}\,\mathrm{Pa}^{-1}$ and $\pi_{<110>} = 70 \times 10^{-11}\,\mathrm{Pa}^{-1}$ [17]. Giant PZR with π values up to $\sim 4000 \times 10^{-11}\,\mathrm{Pa}^{-1}$ have been reported, about 30-100 times those reported for bulk silicon [18]. In addition, several papers have reported an anomalous PZR where the π coefficient has the opposite sign, $\pi_{anom} = -70 \times 10^{-11}\,\mathrm{Pa}^{-1}$. These very different PZR values were reported in nominally identical nanostructures.

The onset of anomalous PZR measurements is still not well understood. Experiments from Ref. [16] suggest that an interplay of electrostatic effects and changes in recombination parameters could explain the switch in sign of the PZR coefficients.

In the experiments of Ref. [16], silicon samples of thickness $t = 2\,\mu\mathrm{m}$ were fabricated using photolithographic methods, to give structures that were p-i-p in nature. The small size of these structures makes them susceptible to space charge effects. The intrinsic region was unintentionally p-doped with a dopant concentration of $10^{13} - 10^{14}$ cm^{-3}. The p-type silicon Ohmic contacts were doped with boron using a doping concentration of $10^{18} - 10^{20}$ cm^{-3}. The length of the intrinsic region was about 100 µm as shown in Fig. 2.12. The same sample is later exposed to a 10 MeV beam of Si^{5+} ions with the aim of forming a desired density of silicon divacancy defects. Now the experimentally observed I-V curve is shown in Fig. 2.11b. There is an initial regime at low biases where the current varies linearly (or sub-linearly). There is a second regime where the log I-log V curve varies quite rapidly, and a third regime where the current again varies linearly. Our numerical results enable us to explain this trend. The defect implantation can induce secondary effects that render the intrinsic region slightly n-doped as has been previously reported in the literature [19]. The initial regime can be understood as bipolar regime, where the electron and hole currents are comparable, followed by a punch-through regime, where the holes begin to dominate the electrons across the sample, and then a unipolar hole regime. It is therefore tempting to explain the PZR measurements after defect implantation (Fig. 2.11a (Top)) as the switching from bipolar transport at low injection to unipolar hole transport at high injections. Moreover, an extension of this work that was pursued in Ref. [16] showed that the switching of PZR was dependent on the shifting of the trap level E_T in the SRH expression with stress. One can see how the magnitude of currents at low biases depends on whether there is recombination or not (Fig. 2.10) and this can be considered as an extreme case of varying the

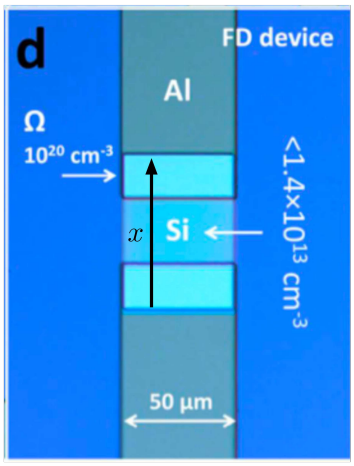

(a) Photo of the top view

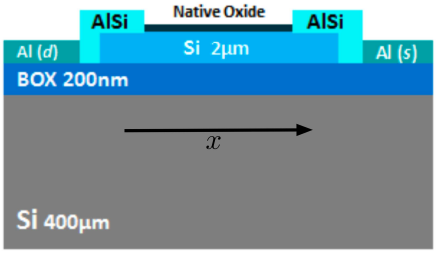

(b) Schematic representation of the side view

Figure 2.12: Photo of the silicon sample, with the x axis corresponding to the simulation marked. Figures taken from Ref. [20]

recombination parameters.

2.3 Conclusion and future work

In this chapter, we have implemented a numerical solver that solves the Poisson equation coupled with the drift-diffusion equations for electrons and holes in semiconductors. We have used the Scharfetter and Gummel discretization scheme to simulate the electronic transport, ensuring the solutions converge sufficiently and that they behave physically.

The solver was applied to the case of experimentally relevant p-i-p samples, and we were able to reproduce the I-V curves before and after defect implantation. The importance of the transport on the recombination parameters and on the electrostatic fields has been demonstrated, and this observation is an important part of Ref. [16].

We were able to qualitatively reproduce the I-V curves that were experimentally observed although there are clear differences. For better quantitative agreement, it was found necessary to model the device in two dimensions including the effects of the electrostatic field outside the device [16], which are not captured in a 1D model used here.

An initial motivation for this work was to model the impedance spectroscopy measurements (Fig. 2.C.1). Impedance spectroscopy consists in applying a small alternating signal v_{AC} of frequency ω around a fixed bias V_{DC}, as

$$V(t) = V_{DC} + v_{AC}e^{i\omega t}. \tag{2.31}$$

Impedance spectroscopy allows one to probe the characteristic time scales involved in carrier transport. This can be done by implementing a small signal analysis of the system, that we have outlined in appendix 2.C. An interesting question is whether the model described will be able to reproduce the characteristic trapping times experimentally.

Future directions for this project could be to include spin dependent trapping and recombination effects in semiconductors such as GaAsN [21].

Appendix

2.A Newton-Raphson method

To solve the system of coupled non-linear equations 2.12 - 2.15, we use the Newton-Raphson method to find the roots of a function $f(x)$. To solve

$$f(x) = 0, \tag{2.32}$$

we begin with an approximation for the root x_0.

$$f(x) = f(x_0) + f'(x_0)(x - x_0) + \cdots = 0 \tag{2.33}$$

gives us a new approximation for the root

$$x = x_0 - \frac{f(x_0)}{f'(x_0)} \tag{2.34}$$

Repeating the above step iteratively, provided $f(x)$ is reasonably well behaved, we converge to the solution of $f(x) = 0$. In our problem, we must solve an equation of the form

$$\vec{f}(\vec{\psi}) = 0, \tag{2.35}$$

where

$$\vec{f}(\vec{\psi}) = \begin{bmatrix} f_1(\vec{\psi}) \\ f_2(\vec{\psi}) \\ \vdots \\ f_{N-1}(\vec{\psi}) \end{bmatrix}, \tag{2.36}$$

and $\vec{\psi} = \psi_1, \psi_2 \ldots \psi_{N-1}$. When the argument of f is multidimensional we can write the expansion 2.34 in term of a gradient as

$$-f(\vec{\psi_0}) = \vec{\nabla} f.\delta\vec{\psi} \tag{2.37}$$

But we have $N-1$ such equations (for $N+1$ node points) so this can be written in the matrix form as

$$\begin{bmatrix} -f_1(\vec{\psi}) \\ \vdots \\ -f_{N-1}(\vec{\psi}) \end{bmatrix} = \begin{bmatrix} \frac{\partial f_1}{\partial \psi_1} & \frac{\partial f_1}{\partial \psi_2} & \cdots & \frac{\partial f_1}{\partial \psi_{N-1}} \\ \vdots & \vdots & \ldots & \vdots \\ \frac{\partial f_{N-1}}{\partial \psi_1} & \frac{\partial f_{N-1}}{\partial \psi_2} & \cdots & \frac{\partial f_{N-1}}{\partial \psi_{N-1}} \end{bmatrix} \begin{bmatrix} \delta\psi_1 \\ \vdots \\ \delta\psi_{N-1} \end{bmatrix}. \tag{2.38}$$

Substituting Poisson's equation for f, we can rewrite the above expression as

$$-(K\vec{\psi} + F(\vec{\psi})) = (K + \nabla F)\delta\vec{\psi}, \tag{2.39}$$

where K is a matrix that represents the differential linear part of the equation and $F = p(\psi) - n(\psi) + C$ and ∇F is the Jacobian of F with respect to $\vec{\psi}$. The above expression can be solved iteratively to get $\delta\vec{\psi}$ which is a better approximation of the solution. A similar set of equations can be calculated for equations 2.14 and 2.15 and a flowchart for the program is shown in Fig. 2.2.

2.B The p-n junction

Before simulating the more pertinent case of a p-i-p structure, we chose to test the program on the better understood case of a p-n junction. The I-V behavior of an ideal p-n junction in forward bias is given by the Shockley equation as

$$I = I_0(e^{\frac{qV}{kT}} - 1) \tag{2.40}$$

In the log I - V plot in Fig. 2.B.3, we observe an initial exponential regime, and a kink that is consistent with the Shockley Read Hall recombination, and a gradual tapering off at higher voltages. This is the expected behavior of a p-n junction, and the Fermi potentials are plotted for three voltage biases. (Fig. 2.B.2)

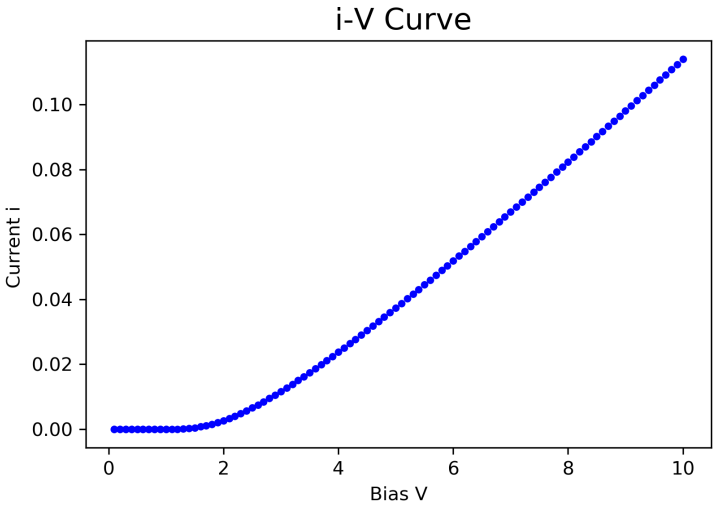

Figure 2.B.1: Simulated I-V curve for a p-n junction. (Arbitrary units are used for the current.)

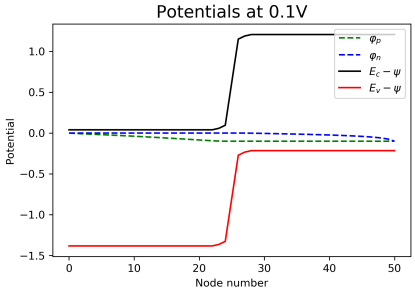

(a) 0.1 V

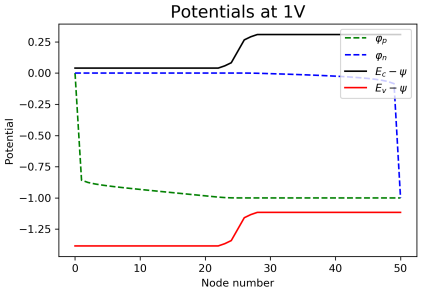

(b) 1 V

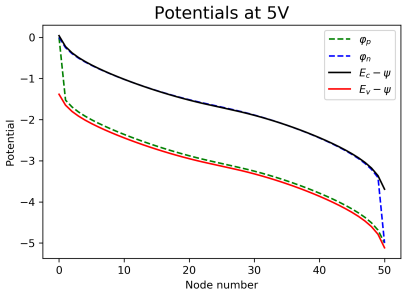

(c) 5 V

Figure 2.B.2: Simulated potentials for the p-n junction at different biases

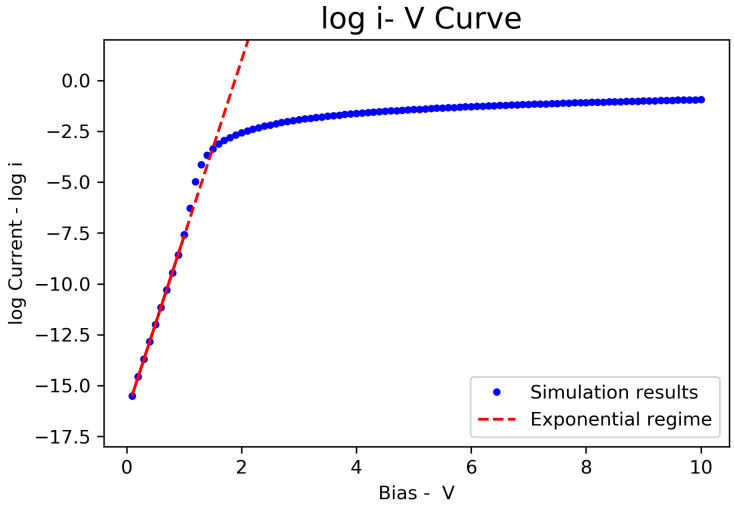

Figure 2.B.3: Simulated Log I - V curve for a p-n junction. (Arbitrary units are used for the current.)

2.C Small signal analysis

The above equations describe the steady state behavior of the devices considered. To model non-steady state equations, we must introduce the time into the equations, and consider the variation of the concentrations with respect to time. These are given as

$$-\frac{d}{dx}\left(\epsilon_r\epsilon_0\frac{d}{dx}\psi\right) - q\left(C + p(\psi,\varphi_p) - n(\psi,\varphi_n)\right) = 0, \tag{2.41}$$

$$\frac{d}{dx}j_n - qR(\psi,\varphi_p,\varphi_n) = q\frac{\partial n(\psi,\varphi_n)}{\partial t}, \tag{2.42}$$

$$\frac{d}{dx}j_p + qR(\psi,\varphi_p,\varphi_n) = q\frac{\partial p(\psi,\varphi_p)}{\partial t}. \tag{2.43}$$

To model the behavior of semi-conductor devices when a small alternating signal v_{AC} is applied around a DC offset V_{DC}

$$V(t) = V_{DC} + v_{AC}e^{i\omega t}. \tag{2.44}$$

The response of the system to this alternating signal, in the small signal limit, (when

$|v_{ac}| \ll |V_{DC}|$) can be written as

$$\psi(x,t) = \psi_0(x) + \tilde{\psi}(x)e^{i\omega t}, \tag{2.45}$$

$$\varphi_n(x,t) = \varphi_{n0}(x) + \tilde{\varphi_n}(x)e^{i\omega t}, \tag{2.46}$$

$$\varphi_p(x,t) = \varphi_{p0} + \tilde{\varphi_p}(x)e^{i\omega t}. \tag{2.47}$$

Equations 2.41 - 2.43 can be written compactly as

$$F(X) = \frac{\partial A(X)}{\partial t} \tag{2.48}$$

where X is the set of $\{\psi, \varphi_p, \varphi_n\}$ and is the sum of the stationary solution and a time varying part as follows $X = X_0 + \tilde{X}e^{i\omega t}$. Expanding equation 2.48 and keeping only linear terms gives us the following matrix equation

$$\left[\nabla F(X_0) - (i\omega)\nabla A(X_0)\right]\tilde{X} = 0 \tag{2.49}$$

where $\nabla F(X_0)$ and $\nabla A(X_0)$ are the Jacobian matrices for F and A with respect to X evaluated at X_0. Solving Eq. 2.49 for non-trivial $\tilde{X}$ would give us the small signal components of $\{\psi, \varphi_p, \varphi_n\}$, thereby helping us evaluate the small signal response of the circuit.

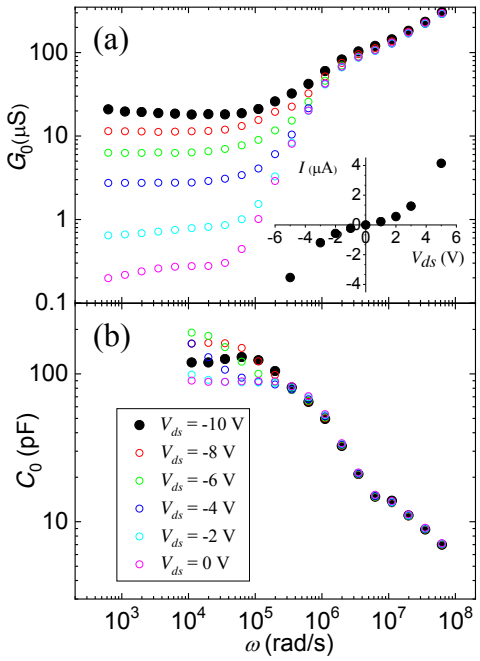

Figure 2.C.1: Zero-stress measurements of the conductance G_0 (top) and capacitance C_0 (bottom) as a function of the frequency ω and gate voltage V_{ds}. The frequency variation of G_0 and C_0 are consistent with a SCLC in the presence of fast traps [22]. Figures taken from [20].

References

[1] C. D. Child. "Discharge From Hot Cao". en. In: *Physical Review (Series I)* 32.5 (May 1911), pp. 492–511. ISSN: 1536-6065. DOI: 10.1103/PhysRevSeriesI.32.492.

[2] M. A. Lampert. "Simplified Theory of Space-Charge-Limited Currents in an Insulator with Traps". en. In: *Physical Review* 103.6 (Sept. 1956), pp. 1648–1656. ISSN: 0031-899X. DOI: 10.1103/PhysRev.103.1648.

[3] W. Shockley and R. C. Prim. "Space-Charge Limited Emission in Semiconductors". en. In: *Physical Review* 90.5 (June 1953), pp. 753–758. ISSN: 0031-899X. DOI: 10.1103/PhysRev.90.753.

[4] P. A. Leighton. "Electronic Processes in Ionic Crystals (Mott, N. F.; Gurney, R. W.)" In: *Journal of Chemical Education* 18.5 (May 1941), p. 249. ISSN: 0021-9584. DOI: 10.1021/ed018p249.1.

[5] A. Carbone, B. K. Kotowska, and D. Kotowski. "Space-Charge-Limited Current Fluctuations in Organic Semiconductors". In: *Physical Review Letters* 95.23 (Nov. 2005), p. 236601. DOI: 10.1103/PhysRevLett.95.236601.

[6] H. C. F. Martens et al. "Crossover from space-charge-limited to recombination-limited transport in polymer light-emitting diodes". en. In: *Physical Review B* 63.12 (Mar. 2001). ISSN: 0163-1829, 1095-3795. DOI: 10.1103/PhysRevB.63.125328.

[7] T. Kirchartz et al. "Understanding the Thickness-Dependent Performance of Organic Bulk Heterojunction Solar Cells: The Influence of Mobility, Lifetime, and Space Charge". In: *The Journal of Physical Chemistry Letters* 3.23 (Dec. 2012), pp. 3470–3475. ISSN: 1948-7185. DOI: 10.1021/jz301639y.

[8] S. C. Jain et al. "Injection- and space charge limited-currents in doped conducting organic materials". In: *Journal of Applied Physics* 89.7 (Mar. 2001), pp. 3804–3810. ISSN: 0021-8979. DOI: 10.1063/1.1352677.

[9] A. C. H. Rowe. "Silicon nanowires feel the pinch". In: *Nature Nanotechnology* 3 (June 2008), p. 311.

[10] Z.-M. Liao et al. "Surface effects on photoluminescence of single ZnO nanowires". en. In: *Physics Letters A* 372.24 (June 2008), pp. 4505–4509. ISSN: 03759601. DOI: 10.1016/j.physleta.2008.04.013.

[11] P. Farrell et al. *Numerical Methods for Drift-diffusion Models*. en. Google-Books-ID: CxP3uQEACAAJ. Weierstraß-Institut für Angewandte Analysis und Stochastik Leibniz-Institut im Forschungsverbund Berlin e.V., 2016.

[12] H. Gummel. "A self-consistent iterative scheme for one-dimensional steady state transistor calculations". en. In: *IEEE Transactions on Electron Devices* 11.10 (Oct. 1964), pp. 455–465. ISSN: 0018-9383. DOI: 10.1109/T-ED.1964.15364.

[13] A. A. Grinberg and S. Luryi. "Space-charge-limited current and capacitance in double-junction diodes". en. In: *Journal of Applied Physics* 61.3 (Feb. 1987), pp. 1181–1189. ISSN: 0021-8979, 1089-7550. DOI: 10.1063/1.338165.

[14] E. Rosencher and B. Vinter. *Optoelectronics*. Trans. by P. G. Piva. Cambridge: Cambridge University Press, 2002. ISBN: 978-0-521-77129-0. DOI: 10.1017/CBO9780511754647.

[15] W. Shockley and W. T. Read. "Statistics of the Recombinations of Holes and Electrons". en. In: *Physical Review* 87.5 (Sept. 1952), pp. 835–842. ISSN: 0031-899X. DOI: 10.1103/PhysRev.87.835.

[16] H. Li et al. "Piezoresistance in Defect-Engineered Silicon". In: *Physical Review Applied* 15.1 (Jan. 2021), p. 014046. DOI: 10.1103/PhysRevApplied.15.014046.

[17] C. S. Smith. "Piezoresistance Effect in Germanium and Silicon". In: *Physical Review* 94.1 (Apr. 1954), pp. 42–49. DOI: 10.1103/PhysRev.94.42.

[18] A. C. H. Rowe. "Piezoresistance in silicon and its nanostructures". en. In: *Journal of Materials Research* 29.6 (Mar. 2014), pp. 731–744. ISSN: 0884-2914, 2044-5326. DOI: 10.1557/jmr.2014.52.

[19] H. Iwata et al. "Change of Majority-Carrier Concentration in p-Type Silicon by 10 MeV Proton Irradiation". In: (2004), p. 5.

[20] H. Li et al. "Giant, Anomalous Piezoimpedance in Silicon-on-insulator". In: *Physical Review Applied* 11.4 (Apr. 2019), p. 044010. DOI: 10.1103/PhysRevApplied.11.044010.

[21] A. Ulibarri et al. "A Systematic Study of Spin-Dependent Recombination in GaAs1-xNx as a Function of Nitrogen Content". In: *physica status solidi (b)* n/a.n/a (). ISSN: 1521-3951. DOI: 10.1002/pssb.202200361.

[22] R. Kassing. "Calculation of the frequency dependence of the admittance of SCLC diodes". en. In: *physica status solidi (a)* 28.1 (Mar. 1975), pp. 107–117. ISSN: 1521-396X. DOI: 10.1002/pssa.2210280110.

Chapter 3

Localization landscape theory

3.1 Introduction

Very generally, the localization properties of a linear vibrational system governed by a second-order elliptical operator L are contained in its eigenvalues and eigenvectors. The eigenvalue problem defined over a domain Ω is

$$L\psi = E\psi \tag{3.1}$$

with appropriate boundary conditions, where ψ is the eigenvector with eigenvalue E. The localization landscape (LL) theory was introduced by Filoche and Mayboroda in 2012 as a way to understand wave localization in disordered systems [1]. In LL theory, the localization properties of such systems are determined by the function u, which is the solution to the associated Dirichlet problem

$$Lu = 1, \tag{3.2}$$

with the same boundary conditions as in Eq. 3.1. Over the years, many properties of the LL have been elucidated, and we summarize the main ones here. First, mathematically, any eigenvector ψ of energy E satisfies the inequality

$$\frac{\psi(\boldsymbol{r})}{\|\psi\|_\infty} \leq Eu(\boldsymbol{r}) \qquad \forall \boldsymbol{r} \in \Omega \tag{3.3}$$

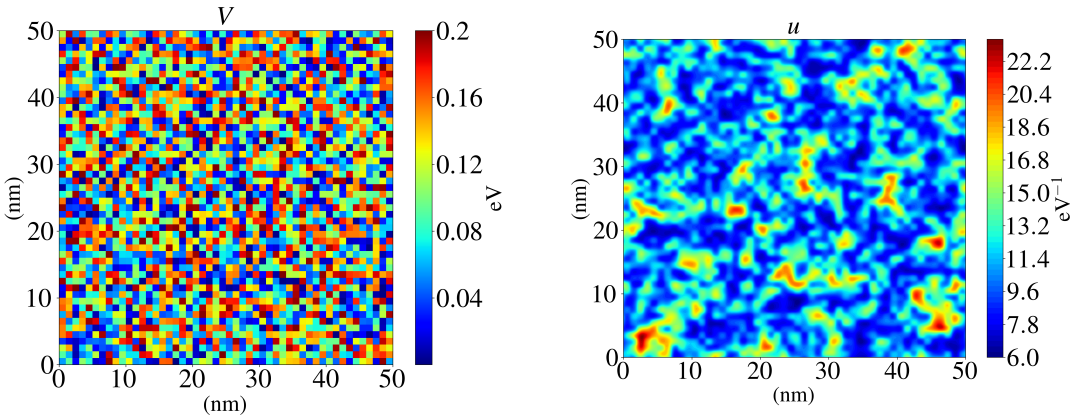

(a) (b)

Figure 3.1.1: a) A disordered potential V where a square domain of side 50 nm is divided into squares of size 1 nm, and the potential takes values uniformly distributed between 0 and 0.2 eV on each of the smaller squares. b) The landscape function u calculated for the potential in a).

where $\|\psi\|_\infty$ refers to the $\mathcal{L}^\infty$ norm of ψ or $\sup_{\boldsymbol{r}\in\Omega}|\psi(\boldsymbol{r})|$. Roughly speaking, the above inequality implies that $\psi(\boldsymbol{r})$ is "small" when $u(\boldsymbol{r})$ is small. The locations where u is small correspond to the valley lines of the graph of u as shown in Fig. 3.1.2. These valley lines (which are hyper-surfaces of dimension $d-1$ in dimension d) partition the graph into a set of sub-regions that house the localized eigenstates.

The inequality in Eq. 3.3 can be obtained by first considering the zero energy Green's function of the operator L defined as

$$LG(\boldsymbol{r},\boldsymbol{r'}) = \delta(\boldsymbol{r}-\boldsymbol{r'}) \tag{3.4}$$

where $\delta(\boldsymbol{r}-\boldsymbol{r'})$ is the Dirac delta distribution centered at $\boldsymbol{r'}$ and observing that the landscape function u can be expressed as a convolution of the Green's function with 1,

$$u(\boldsymbol{r}) = \int_\Omega G(\boldsymbol{r},\boldsymbol{r'}).1d\boldsymbol{r'}. \tag{3.5}$$

Rewriting the eigenfunction ψ, we have

$$\psi(\boldsymbol{r}) = \int_\Omega \psi(\boldsymbol{r'})LG(\boldsymbol{r},\boldsymbol{r'})d\boldsymbol{r'} = \int_\Omega L\psi(\boldsymbol{r'})G(\boldsymbol{r},\boldsymbol{r'})d\boldsymbol{r'} = \int_\Omega E\psi(\boldsymbol{r'})G(\boldsymbol{r},\boldsymbol{r'})d\boldsymbol{r'}. \tag{3.6}$$

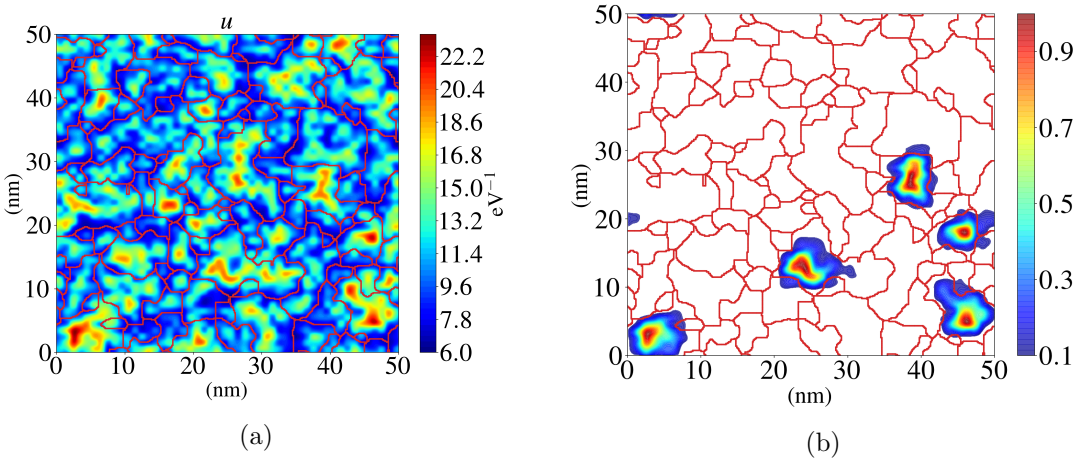

Figure 3.1.2: 2D color representation of the a) landscape function u; the valley lines superimposed in red. b) The valley lines of u and the first 5 eigenstates.

If one considers the absolute value of the eigenstate ψ, we have

$$|\psi(\boldsymbol{r})| \leq E\|\psi\|_\infty \int_\Omega |G(\boldsymbol{r}, \boldsymbol{r'})| d\boldsymbol{r'}. \tag{3.7}$$

If the Green's function is positive then we have from Eq. 3.5,

$$|\psi(\boldsymbol{r})| \leq E\|\psi\|_\infty u(\boldsymbol{r}), \tag{3.8}$$

which is the desired inequality. The above theory is universal and can be applied to any type of vibrational system that is governed by a second order elliptic operator, and for which consequently the Green's function is positive. In the work presented in this thesis, we consider the operator L to be the Hamiltonian $\hat{H}$ for a quantum particle

$$\hat{H} = -\frac{\hbar^2}{2m}\Delta + V(\boldsymbol{r}) \tag{3.9}$$

where Δ refers to the Laplacian operator $\sum_i^d \frac{\partial^2}{\partial x_i^2}$ in d dimensions, and for which the Green's function is positive if V is positive.

3.1.1 Localization sub-regions

The first important observation is that the valleys of u form a network that partitions the domain into a disjoint set of sub-regions. If the reciprocal of E is larger than u, then the inequality 3.3 is trivially satisfied, as the eigenstates are normalized by their maximum value. At a given energy E, only the parts of the valley network that satisfy $u(\boldsymbol{r}) \leq 1/E$ correspond to an effective constraint on the amplitude of $\psi(\boldsymbol{r})$. This subset of the valley network is called the *effective valley network* and is denoted $\mathcal{N}(E)$, depicted in Fig. 3.1.3 for a few examples of eigenstates.

- At low E, $\mathcal{N}(E)$ is essentially the initial valley network and the modes are confined with the regions delimited by $\mathcal{N}(E)$, as can be seen for modes 0, 1 and 2 in Fig. 3.1.3
- At higher values of E, openings begin to appear in the network as the higher parts of $\mathcal{N}(E)$ are removed. The modes are still localized, but in larger regions which are the results of the merging of the smaller initial subregions (modes 35, 36 and 37).
- At very high energies, $\mathcal{N}(E)$ is mostly disconnected. The eigenstates are free to percolate through the whole domain and delocalized states progressively appear (modes 97, 98 and 99).

3.1.2 Effective confining potential

Another way to interpret the landscape function, and probably the most important one, is to transform the original Schrödinger equation by introducing an auxiliary function ψ_1 such that $\psi \equiv u\psi_1$, which yields

$$-\frac{\hbar^2}{2m}\left[\frac{1}{u^2}\nabla.(u^2\nabla\psi_1)\right] + \frac{1}{u}\psi_1 = E\psi_1 \tag{3.10}$$

One can see that the auxiliary function $\psi_1 = \psi/u$ obeys a new Schrödinger-type equation in which the original potential $V(\boldsymbol{r})$ has been replaced by $1/u(\boldsymbol{r})$ which plays the role of an "effective confining potential" $W(\boldsymbol{r}) = 1/u(\boldsymbol{r})$. The valleys of u, which are the boundaries of the localization subregions now correspond to the crest

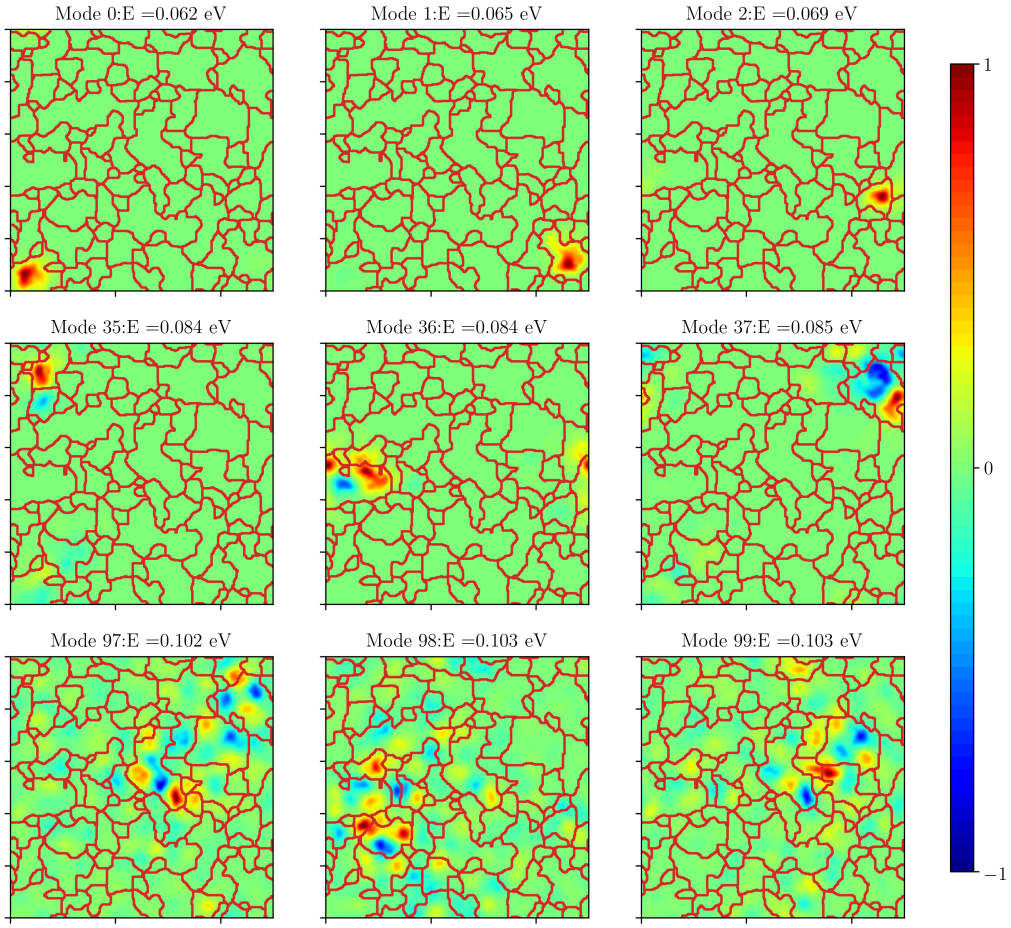

Figure 3.1.3: The spatial representation of several eigenstates for the potential depicted in Fig. 3.1.1 with the effective valley network $\mathcal{N}(E)$ depicted in red.

lines (or watershed lines) of W and thus act as barriers to the auxiliary function ψ_1. The localized eigenstates are now found in the basins of the effective potential $1/u$. The role of an effective potential is exemplified in the following identity satisfied by any quantum state $|\psi\rangle$ [2]:

$$\langle\psi|\hat{H}|\psi\rangle = \frac{\hbar^2}{2m}\langle u\nabla\Big(\frac{\psi}{u}\Big)|u\nabla\Big(\frac{\psi}{u}\Big)\rangle + \langle\psi|\hat{W}|\psi\rangle\,. \tag{3.11}$$

The above expression shows the original Hamiltonian now expressed as the sum of an effective kinetic energy operator and an effective potential energy operator $1/u$. This identity shows that the energy E of any quantum state $|\psi\rangle$ can never be smaller than the one it would have in a potential $W(\boldsymbol{r})$. We will show in the next section that the new effective potential energy accounts for the majority of the total energy of a localized fundamental state (a "bump"), thereby absorbing the kinetic and potential energy contributions of the original Hamiltonian into a largely potential energy term, describing it essentially as a classical system.

Eigenvalue and eigenvector approximation

The LL is able to determine precisely the position of the localized wave functions. Moreover, simple calculations using the properties of the landscape show that the fundamental eigenenergy and eigenfunction in each localization region can be assessed with a very good precision without solving the Schrödinger equation. To that end, the first step consists in decomposing the landscape function u on the orthonormal basis of the eigenvectors ψ_i of the Hamiltonian $\hat{H}$.

$$u = \sum_i \alpha_i\psi_i, \text{ where } \alpha_i = \langle u|\psi_i\rangle = \int u(\boldsymbol{r})\psi_i(\boldsymbol{r})d\boldsymbol{r} \tag{3.12}$$

The self-adjointness of the Hamiltonian leads to:

$$\alpha_i = \langle u|\psi_i\rangle = \frac{1}{E_i}\langle u|\hat{H}\psi_i\rangle = \frac{1}{E_i}\langle\hat{H}u|\psi_i\rangle = \frac{1}{E_i}\langle 1|\psi_i\rangle \tag{3.13}$$

and so u can be finally expressed as

$$u = \sum_i \frac{1}{E_i} \langle 1|\psi_i\rangle \, \psi_i \tag{3.14}$$

The claim is now that u is mostly a weighted sum of the fundamental localized modes of the system. To see why this is the case, we observe that the valley lines of u divide the domain Ω into a set of sub-regions Ω_j. One can distinguish three contributions to the value of u at any point $\boldsymbol{r}$ in one of these subregions Ω_j:

- Eigenstates that are localized outside the subregion Ω_j. The contribution of these eigenstates to the sum in Eq. 3.14 is then negligible.

- Eigenstates that are delocalized over the domain Ω, or that are higher excited states with several oscillations over Ω_j . The amplitudes α_i are inversely proportional to the energy of their associated eigenstate, and furthermore the quantity $\langle 1|\psi_i\rangle$ will tend to be smaller for states with several oscillations. The contribution due to such states can also be neglected.

- Fundamental modes that are localized within the subregion Ω_j and resemble a bump. These will be the states with the lowest energy in Ω_j and that will have the least number of oscillations in Ω_j. They will therefore be the dominant contributors in Eq. 3.14.

Consequently, one can assume that in each sub-region Ω_j that is able to host a localized state, the fundamental mode in that region is proportional to u restricted to that sub-region. We can thus use the same index i for the sub-region and the eigenstate to reflect this. We therefore have in sub-region Ω_i,

$$u \approx \frac{\langle 1|\psi_i^0\rangle}{E_i^0}\psi_i^0 \tag{3.15}$$

which leads to

$$\psi_0^i \approx \frac{u}{||u||} \tag{3.16}$$

Furthermore the energy E_i^0 is approximated by

$$E_i^0 = \langle \psi_i^0 | \hat{H} | \psi_i^0 \rangle \approx \frac{\langle u | \hat{W} | u \rangle}{||u||^2} = \frac{\langle u | 1 \rangle}{||u||^2} = \frac{\int_{\Omega_i} u(\boldsymbol{r}) d\boldsymbol{r}}{\int_{\Omega_i} u^2(\boldsymbol{r}) d\boldsymbol{r}} \tag{3.17}$$

In the above equations, $\hat{H}$ was replaced by $\hat{W}$ because the effective kinetic energy term in Eq. 3.11 has a negligible contribution as ψ_i^0/u is mostly constant and the gradient is small. This justifies our claim in the previous section that the effective potential contains the dominant contribution to the total energy. The above relation along with the effective potential was used to deduce a useful approximation for the energies of the eigenstates located and the value of the effective potential at the corresponding minima [3]. If we assume that the localized eigenfunction in a sub-region has the shape of a bump which can be approximated as the positive part of a quadratic function defined below,

$$u = u_{max} \left[1 - \sum_{k=1}^{d} \left(\frac{x_k}{a_k} \right)^2 \right] \text{ on } \Omega = \{ x \in R^d | \sum_{k=1}^{d} \left(\frac{x_k}{a_k} \right)^2 \leq 1 \} \tag{3.18}$$

the sum being over all spatial directions d. Inserting the above expression into Eq. 3.17, we get

$$E_i^0 \approx \frac{1}{u_{max}} \frac{\int_{\Omega_i} \left[1 - \sum_{k=1}^{d} (\frac{x_k}{a_k})^2 \right] d^d r}{\int_{\Omega_i} \left[1 - \sum_{k=1}^{d} (\frac{x_k}{a_k})^2 \right]^2 d^d r} \approx \left(1 + \frac{d}{4} \right) W_{min}^i \tag{3.19}$$

which is a useful result since it turns out the ratio between the energy of the fundamental eigenstate in a sub-region is related to the value of the minimum of the effective potential in the same region, and is independent of the other details of the state.

Exponential Decay and Agmon Distance

The effective potential provides also an estimate of the exponential decay of the localized eigenstate outside its main existence region through a metric defined from W. Inspired by the work by Agmon [4], at any given energy E, the function $W(\boldsymbol{r}) - E$

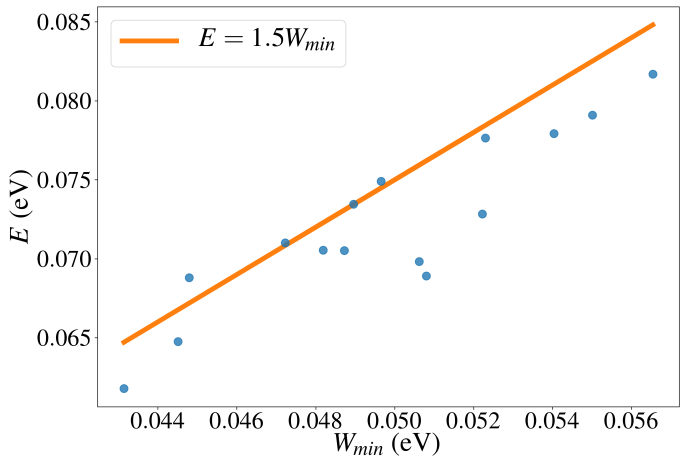

Figure 3.1.4: Ratio of E_i to W_{min}, the minimum of $W = 1/u$ in the basin Ω_i, for the fundamental localized modes for the potential in Fig. 3.1.1.

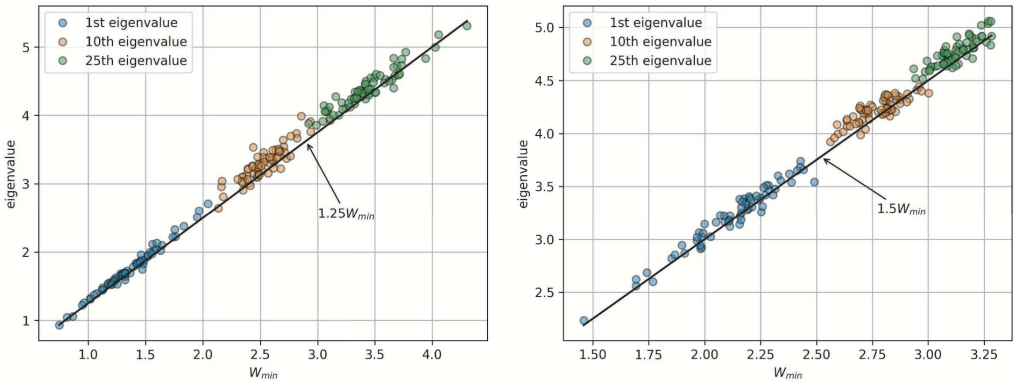

Figure 3.1.5: The 1st, 10th, and 25th eigenvalues versus the corresponding minima values of the effective potential, for 64 independent realizations of a random potential. Left, in one dimension where the black line shown is $E = 1.25W_{min}$. Right, in two dimensions with $E = 1.5W_{min}$. Taken from [3].

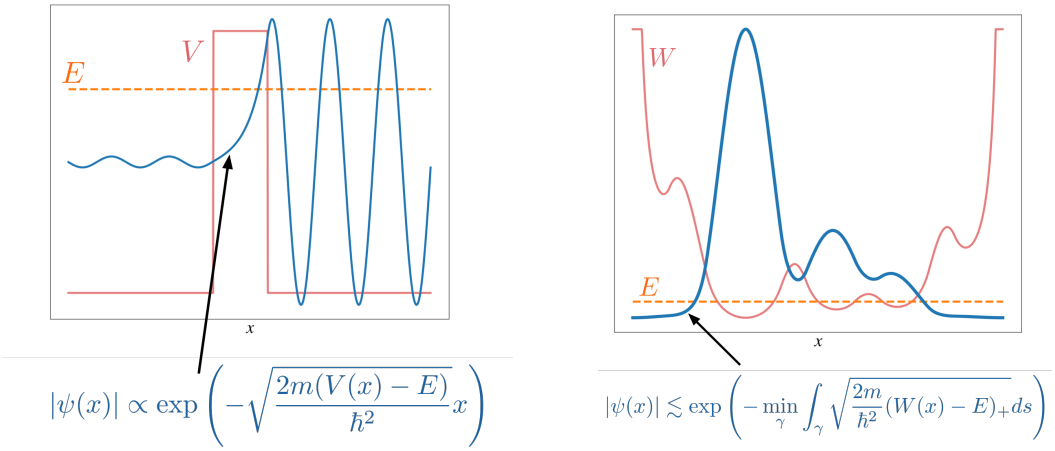

(a) (b)

Figure 3.1.6: (a) Quantum tunneling through a barrier. (b) Analogous W-based Agmon distance defined for a disordered potential.

defines a distance $\rho_E(\boldsymbol{r}_1, \boldsymbol{r}_2)$ between any pair of points $\boldsymbol{r}_1$, $\boldsymbol{r}_2$. The distance is defined as

$$\rho_E(\boldsymbol{r_1}, \boldsymbol{r_2}) = \min_{\gamma} \int_{\gamma} \sqrt{\frac{2m}{\hbar^2}\left[W(\boldsymbol{r}) - E\right]_+} ds \tag{3.20}$$

where $[x]_+$ is $\max(x, 0)$, and the minimum is taken over all paths γ connecting $\boldsymbol{r}_1$ to $\boldsymbol{r}_2$. The effective potential thus controls the exponential decay of the eigenfunction via the inequality

$$|\psi(\boldsymbol{r})| \lesssim e^{-\rho_E(\boldsymbol{r}, \boldsymbol{r_0})} \tag{3.21}$$

where $\boldsymbol{r}_0$ is the point corresponding to the maximum of the localized eigenstate and $\boldsymbol{r}$ is any point outside this region. The above metric can be thought of as a generalization of the exponential decay of the wavefunction when it tunnels through a barrier, as depicted in Fig. 3.1.6. In the case of quantum tunneling through a barrier, the wave function decays exponentially at a rate that is proportional to $\sqrt{\frac{2m}{\hbar^2}\left[V(\boldsymbol{r}) - E\right]}$, when $V(\boldsymbol{r}) > E$. Eqs. 3.20-3.21 prescribe a similar exponential decay for disordered potentials. In Fig. 3.1.8, we compare the eigenstate and the effective potential based approximation in log scale.

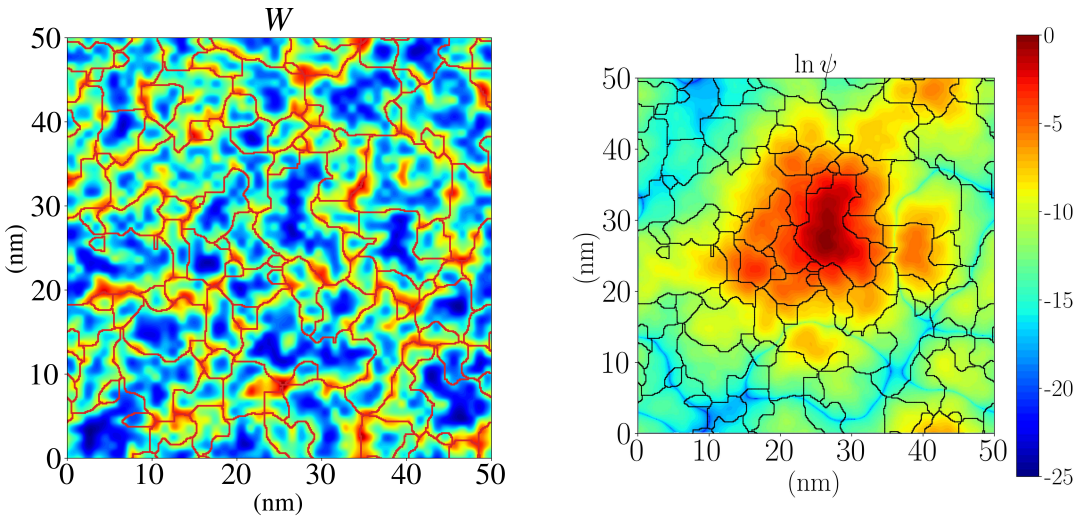

(a) (b)

Figure 3.1.7: a) The effective potential W for the disordered potential in Fig. 3.1.1 with the watershed lines in red. b) An eigenstate in natural log scale to visualize the exponential decay of the states.

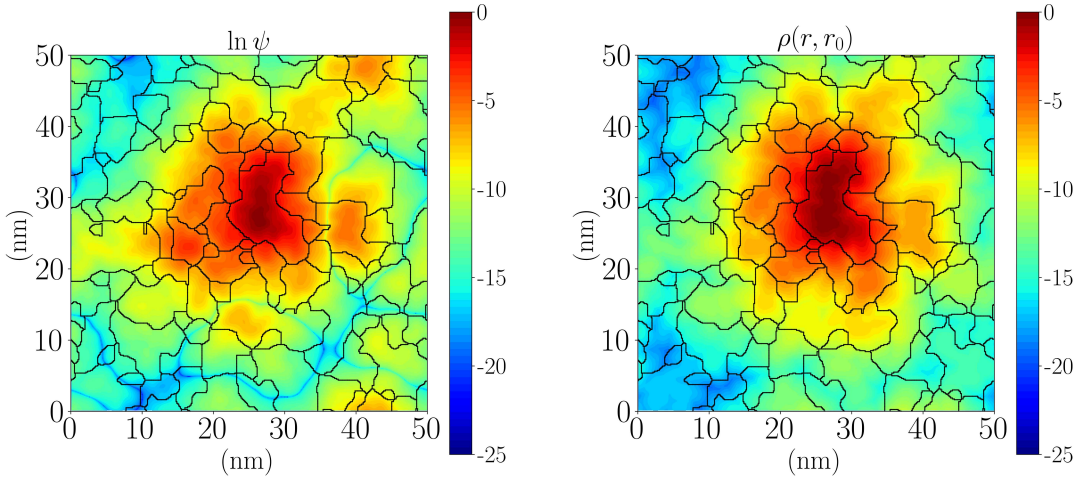

(a) True eigenstate (b) W based Agmon distance

Figure 3.1.8: a) An eigenstate in natural log scale and b) the W based Agmon distance.

Integrated Density of States

Not only does the effective potential provide spatial information about the eigenstates but it can also be used to get an estimate of the integrated density of states of the system or the counting function $N_V(E)$ which is defined as the number of states of the system smaller than E. This is done through a straightforward extension of the Weyl law [5], which states that the counting function $N_V(E)$ can be approximated in the asymptotic limit $E \to +\infty$ by the volume in phase space $(\boldsymbol{r}, \boldsymbol{k})$ that can be explored by a classical particle of mechanical energy smaller than E,

$$N_V(E) \approx \frac{1}{(2\pi)^d} \iint_{H(\boldsymbol{r},\boldsymbol{k})\leq E} d\boldsymbol{r} d\boldsymbol{k}. \tag{3.22}$$

For the Schrödinger Hamiltonian operator of Eq. 3.9, the associated Hamiltonian function $H(\boldsymbol{r}, \boldsymbol{k})$ appearing in Eq. 3.22 is given by the Weyl transform of the Hamiltonian operator and reads $H(\boldsymbol{r}, \boldsymbol{k}) = \frac{\hbar^2 k^2}{2m} + V(\boldsymbol{r})$. Thus, we have

$$N_V(E) \approx \frac{1}{(2\pi)^d} \iint_{\frac{\hbar^2 k^2}{2m}+V(\boldsymbol{r})\leq E} d\boldsymbol{r} d\boldsymbol{k}. \tag{3.23}$$

Integrating over $\boldsymbol{k}$, we have

$$N_V(E) \approx \frac{v_d}{(2\pi)^d} \Big(\frac{2m}{\hbar^2}\Big)^{d/2} \int (E - V(\boldsymbol{r}))_+^{\,d/2} d\boldsymbol{r}, \tag{3.24}$$

where v_d is the volume of the unit ball in d dimensions. The above expression may appear daunting but is a rather simple integration of the potential over space. It turns out that the above expression does not work so well at low energies for disordered potentials. However, if one replaces the original potential in the above expression by the effective potential W, we get a better estimate as can be seen for the 2D potential in Fig. 3.1.9 and for various different 1D potentials described in Ref. [2] in Fig. 3.1.10. Replacing the original potential V by the effective potential W will be a common thread in many of the following sections.

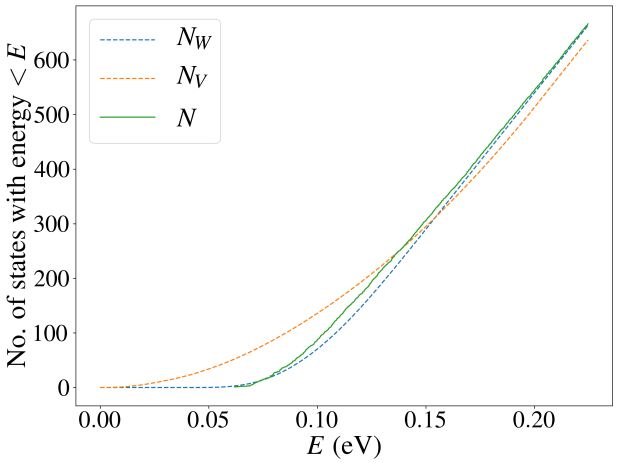

Figure 3.1.9: For the 2D potential in Fig. 3.1.1, the counting function N (the solid green line) is represented, together with N_V (the orange dotted line), Weyl's approximation using the original potential V [as defined in Eq. 3.23], and N_W (the blue dotted line), the same with W.

3.2 LL theory in semiconductors

The LL theory was further developed to be applied to semiconductor systems and to account for quantum localization effects in transport and absorption measurements. To this end, in semiconductor structures, two Schrödinger equations are written down, one for electrons and one for holes respectively,

$$-\frac{\hbar^2}{2m_e^*}\Delta\psi_e(\boldsymbol{r}) + E_c(\boldsymbol{r})\psi_e(\boldsymbol{r}) = E\psi_e(\boldsymbol{r}) \tag{3.25}$$

$$-\frac{\hbar^2}{2m_h^*}\Delta\psi_h(\boldsymbol{r}) + E_v(\boldsymbol{r})\psi_h(\boldsymbol{r}) = E\psi_h(\boldsymbol{r}) \tag{3.26}$$

where m_e^*, m_h^* are the effective masses of the electrons and holes respectively, $E_c(\boldsymbol{r}), E_v(\boldsymbol{r})$ are the conduction and valence band potentials, ψ_e, ψ_h are the envelope functions of the electron and hole wavefunctions. Once the electron and hole wave functions and energies are known, they are used to compute the carrier concentrations

$$n(\boldsymbol{r}) = \sum_i \left(\frac{1}{1+e^{\frac{E_i^e - E_F}{k_B T}}}\right)|\psi_e^i(\boldsymbol{r})|^2 \tag{3.27}$$

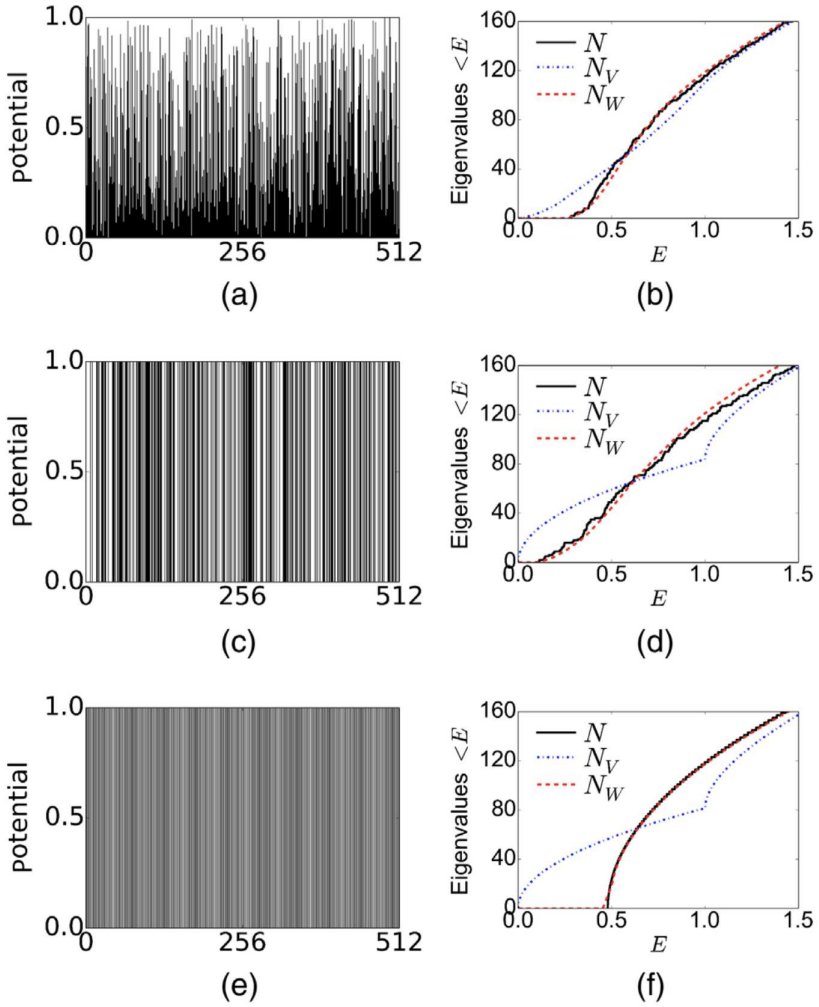

Figure 3.1.10: (Left panels) Three different types of potentials: (a) random with uniform law on $[0, 1]$, (c) random Boolean (0 or 1), and (e) periodic with 256 periods, $V = 0$ on the first half of the period, $V = 1$ on the second half. (Right panels) For each potential, the counting function N (the solid black line) is represented, together with N_V (the blue dash-dotted line), Weyl's approximation using the original potential V [as defined in Eq. 3.23], and N_W (the red dotted line), the same with W. Notice in all cases the remarkable agreement between N and N_W. Taken from [2]

$$p(\boldsymbol{r}) = \sum_i \left(\frac{1}{1 + e^{\frac{E_F - E_i^h}{k_B T}}} \right) |\psi_h^i(\boldsymbol{r})|^2 \tag{3.28}$$

where E_F is the Fermi level of the system, k_B is the Boltzmann constant and T is the temperature of the system. The above expressions represent a sum of the probability distributions for each state weighted by the Fermi-Dirac statistics. These carrier concentrations are then used to calculate the electric field due to the presence of charge via the Poisson equation

$$\nabla.(\epsilon_r \nabla\phi) = \frac{q}{\epsilon_0}(n - p - N_D^+ + N_A^-) \tag{3.29}$$

where ϕ is the electrostatic potential, ϵ_r is the relative permittivity of the medium. The N_D^+, N_A^- refer to the concentrations of the ionized donors and acceptors for the given system. The electrostatic potential is then fed back to get an updated version of the conduction and valence bands,

$$E_c(\boldsymbol{r}) = -e\phi(\boldsymbol{r}) + \delta E_c(\boldsymbol{r}) \tag{3.30}$$

$$E_v(\boldsymbol{r}) = e\phi(\boldsymbol{r}) + \delta E_v(\boldsymbol{r}) \tag{3.31}$$

where $\delta E_c(\boldsymbol{r}), \delta E_v(\boldsymbol{r})$ are the band offsets of the material in question. We note therefore that in the absence of charge transport, the above equations must be solved self-consistently to obtain the carrier concentrations as is shown in Fig. 3.2.1 (blue arrows).

The above scheme thus requires solving the Schrödinger equations for the holes and electrons to evaluate the carrier concentrations. One important simplification can be made by using landscape theory to arrive at the carrier concentrations without solving the eigenvalue problem. This is done by first noticing the form of the expression of the integrated density of states (IDOS)

$$IDOS(E) \approx \frac{2}{(2\pi)^3} \iint_{H(\boldsymbol{r},\boldsymbol{k}) \leq E} d\boldsymbol{r} d\boldsymbol{k} \tag{3.32}$$

which can be represented as a spatial integral of a local quantity called the local

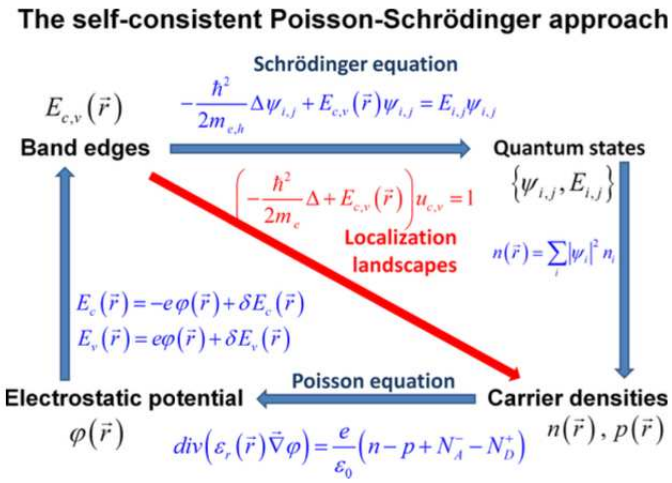

Figure 3.2.1: Schematic structure of the self-consistent Poisson-LL model allowing us to bypass solving the Schrödinger equation. From [6].

integrated density of states (LIDOS)

$$IDOS(E) = \int LIDOS(\boldsymbol{r}, E)d\boldsymbol{r} \tag{3.33}$$

As a specific example, for the conduction band, the $LIDOS_n$ (the subscript n denotes electrons) in 3D is

$$LIDOS_n(E, \boldsymbol{r}) = \frac{1}{3\pi^2}\left(\frac{2m_e^*}{\hbar^2}\right)^{3/2}[E - E_c(\boldsymbol{r})]^{3/2} \tag{3.34}$$

Differentiating with respect to $\boldsymbol{r}$ gives us the local density of states $LDOS_n(\boldsymbol{r}, E)$

$$LDOS_n(E, \boldsymbol{r}) = \frac{1}{2\pi^2}\left(\frac{2m_e^*}{\hbar^2}\right)^{3/2}\sqrt{[E - E_c(\boldsymbol{r})]} \tag{3.35}$$

Similar expressions can be written down for holes and the valence band. The expression for the carrier concentrations in Eq. 3.27 is now replaced by integrating the

LDOS over energy and we have

$$n(\boldsymbol{r}) = \int \left(\frac{1}{1 + e^{\frac{E - E_F}{k_B T}}} \right) LDOS_n(E, \boldsymbol{r}) dE \tag{3.36}$$

$$p(\boldsymbol{r}) = \int \left(\frac{1}{1 + e^{\frac{E_F - E}{k_B T}}} \right) LDOS_p(E, \boldsymbol{r}) dE. \tag{3.37}$$

An important simplification comes by remembering once again that the effective potential derived by solving the LL equation better accounts for the IDOS and therefore for the LDOS as well. $E_c(\boldsymbol{r})$ in Eq. 3.35 is thus replaced by the effective potential $W_c(\boldsymbol{r})$ as

$$LDOS_n(E, \boldsymbol{r}) = \frac{1}{2\pi^2} \left(\frac{2m_e^*}{\hbar^2} \right)^{3/2} \sqrt{[E - W_c(\boldsymbol{r})]} \tag{3.38}$$

In the presence of an external electric field, we are no longer at thermal equilibrium, and therefore cannot define a unique Fermi level for both electrons and holes. The quasi-Fermi levels must be introduced in the expressions of the carrier concentrations.

$$n(\boldsymbol{r}) = \int \left(\frac{1}{1 + e^{\frac{E - E_{Fn}}{k_B T}}} \right) LDOS_n(E, \boldsymbol{r}) dE \tag{3.39}$$

$$p(\boldsymbol{r}) = \int \left(\frac{1}{1 + e^{\frac{E_{Fp} - E}{k_B T}}} \right) LDOS_p(E, \boldsymbol{r}) dE. \tag{3.40}$$

Furthermore, we can write expressions for the carrier currents flowing through the system as gradients of this quasi-Fermi levels

$$\boldsymbol{J}_n = n\mu_n \nabla E_{F_n} \tag{3.41}$$

$$\boldsymbol{J}_p = p\mu_p \nabla E_{F_p} \tag{3.42}$$

where μ_n, μ_p are the electron and hole mobilities, respectively. The current conservation is expressed as

$$\nabla \cdot \boldsymbol{J}_n = R + G_n \tag{3.43}$$

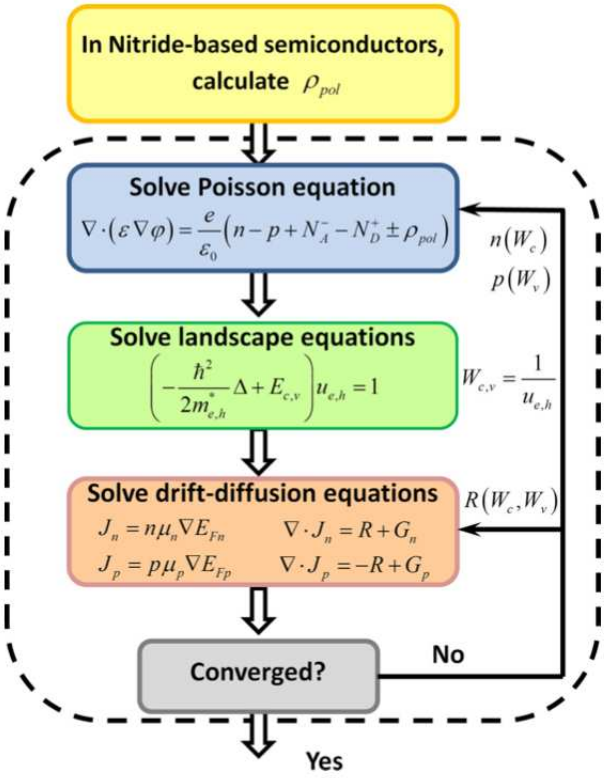

Figure 3.2.2: Flow chart solving the Poisson and drift-diffusion equations with the LL theory. Taken from [6].

$$\nabla \cdot \boldsymbol{J}_p = -R + G_p \tag{3.44}$$

where R is the recombination rate, and G_n, G_p are the carrier generation rates for electrons and holes, respectively.

The above system of equations must be solved self-consistently. It is described in the flow chart of Fig. 3.2.2, and was applied to calculation of the transport and absorption characteristics of quantum well structures in disordered alloys of InGaN in Refs. [6, 7, 8]. Most dramatically, it was showed that the Poisson-LL loop was 100-1000 times faster than the Poisson-Schrödinger loop. [8].

3.3 Wigner-Weyl formalism

We saw in the previous section that the effective potential better accounts for the local density of states in quantum systems, as it better captures the volume of the system in phase space, especially at low energies. A natural extension would be to seek a phase space formalism of quantum mechanics. This is the Wigner-Weyl formalism. The Wigner function f_W for a pure state ψ as previously defined in Chapter 1, is introduced in phase space $(\boldsymbol{r}, \boldsymbol{k})$ [9]

$$f_W(\boldsymbol{r}, \boldsymbol{k}) \equiv \int \psi^*\Big(\boldsymbol{r} + \frac{\boldsymbol{x}}{2}\Big)\psi\Big(\boldsymbol{r} - \frac{\boldsymbol{x}}{2}\Big)\ \exp(-i\boldsymbol{k}\cdot\boldsymbol{x})d\boldsymbol{x}. \tag{3.45}$$

The Wigner function satisfies many important properties. It can be understood, in particular, as being close to a probability distribution in phase space. This last statement comes from the fact that the two marginal integrals along $\boldsymbol{r}$ and $\boldsymbol{k}$ satisfy

$$\frac{1}{(2\pi)^d}\int f_W(\boldsymbol{r}, \boldsymbol{k})d\boldsymbol{k} = |\psi(\boldsymbol{r})|^2 \tag{3.46}$$

$$\frac{1}{(2\pi)^d}\int f_W(\boldsymbol{r}, \boldsymbol{k})d\boldsymbol{r} = |\chi(\boldsymbol{k})|^2 \tag{3.47}$$

where $\chi(\boldsymbol{k})$ is the Fourier transform of the wave function ψ defined as $\chi(\boldsymbol{k}) = \frac{1}{(2\pi)^{d/2}}\int e^{-i\boldsymbol{k}.\boldsymbol{x}}\psi(\boldsymbol{x})d\boldsymbol{x}$. In addition, the Hermitian inner product in Hilbert space is transported into the inner product on distributions in phase space through the Moyal formula satisfied by any pair of quantum states (ψ_1, ψ_2):

$$\frac{1}{(2\pi)^d}\iint f_W^{\psi_1}(\boldsymbol{r}, \boldsymbol{k})f_W^{\psi_2}(\boldsymbol{r}, \boldsymbol{k})d\boldsymbol{r}d\boldsymbol{k} = |\ \langle\psi_1|\psi_2\rangle\ |^2 \tag{3.48}$$

One should note, however, that $f_W(\boldsymbol{r}, \boldsymbol{k})$ is not a genuine probability distribution over phase space. For instance, it can take negative values. Consequently, one should be careful in the physical interpretation of this quantity. This formalism is completed on the operator side by the Weyl transform. The Weyl transform of any operator $\hat{O}$ acting on quantum states is defined as

$$\tilde{O}(\boldsymbol{r}, \boldsymbol{k}) = \int e^{-i\boldsymbol{k}.\boldsymbol{y}}\left\langle \boldsymbol{r} + \frac{\boldsymbol{y}}{2}\right|\hat{O}\left|\boldsymbol{r} - \frac{\boldsymbol{y}}{2}\right\rangle d\boldsymbol{y} \tag{3.49}$$

For instance, the Weyl transform of the Hamiltonian $\hat{H}$ is $\tilde{H}(\boldsymbol{r},\boldsymbol{k}) = \frac{\hbar^2 k^2}{2m} + V(\boldsymbol{r})$. (One can define in a similar fashion the Weyl transform of the effective Hamiltonian $\tilde{H}_{\text{eff}} \approx \frac{\hbar^2 k^2}{2m} + W(\boldsymbol{r})$). The main property of the Weyl transform, in conjunction with the Wigner function, is that it provides a measure on phase space which can be used to compute the expectation of any observable through the following identity:

$$\langle O \rangle_\psi = \langle \psi | \hat{O} | \psi \rangle = \frac{1}{(2\pi)^d} \iint f_W(\boldsymbol{r},\boldsymbol{k})\ \tilde{O}(\boldsymbol{r},\boldsymbol{k}) d\boldsymbol{r} d\boldsymbol{k} \tag{3.50}$$

To understand how the formalism captures the behavior of our system in phase space, we evaluate the quantity defined as

$$F(\boldsymbol{r},\boldsymbol{k},E) = \sum_i f_W^{\psi_i}(\boldsymbol{r},\boldsymbol{k})\ \Theta(E - E_i) \tag{3.51}$$

which is the sum of the Wigner functions of all the eigenstates up to a certain energy E. In Fig 3.3.1, the quantity $F(\boldsymbol{r},\boldsymbol{k},E)$ is plotted for a disordered potential along with the contour lines of Weyl transform for $\tilde{H}(\boldsymbol{r},\boldsymbol{k}) = E$ and $\tilde{H}_{\text{eff}}(\boldsymbol{r},\boldsymbol{k}) = E$. It can be noted in Fig. 3.3.1 that the solid contour lines corresponding to the effective potential accurately capture the distribution of the states in phase space. These observations were used to calculate the absorption in semiconductor structures [10] and spectral functions for cold atomic systems [11].

3.4 Summary

In this chapter, we have described the major concepts and previous developments in LL theory. The LL based effective potential allows us to assess the locations and energies of localized states in response to a disordered potential. We outlined an application of LL theory in modeling electronic localization and transport in disordered semiconductors through a Poisson-drift-diffusion-LL loop.

We described the effective potential based Agmon distance and its ability to bound the exponential decay of the eigenstates. So far, this metric has not been used to address electronic transport. In the following chapter, we will assess the applicability of modeling hopping transport using the Agmon metric.

In addition, we outlined the LL based Wigner-Weyl approach which gives us a

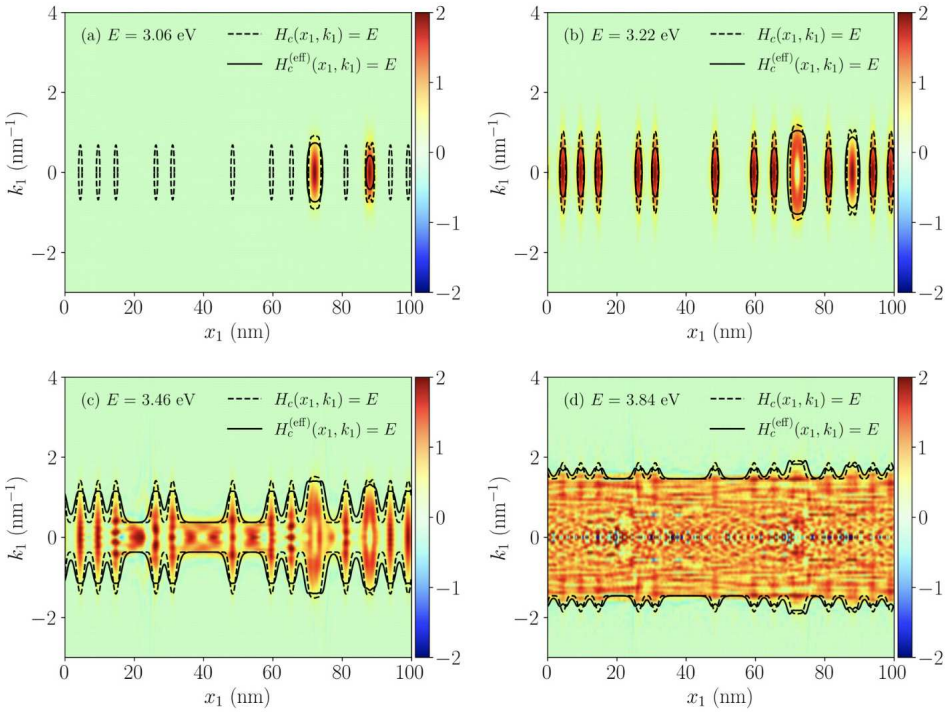

Figure 3.3.1: The sum of the Wigner transforms $f_W^{\psi_i}$ of eigenstates whose eigenenergy lies below a given energy E for a one-dimensional disordered potential. Taken from [10].

phase space description of the eigenstates in a disordered potential. This could be a potential method to address the higher excited states that are not accessible by the current method. Furthermore, it could be interesting perspective to integrate this approach in a Wigner-Weyl theory of transport described in chapter 1. The Wigner-Weyl approach is not developed further in this manuscript but can be envisioned to develop a full model of transport in semiconductors, that would be the equivalent to the drift-diffusion model but accounting for quantum effects at the nanoscale.

Appendix

3.A Watershed algorithm

In the following section, we describe the adapted watershed algorithm [12], which is used to identify the basins of the effective potential W capable of hosting localized eigenstates. The effective potential contains set of minima, as shown in Fig. 3.A.1. However as can be seen in 3.A.1, not all these minima necessarily correspond to a peak of a localized eigenstate. In fact, it can be observed that if one partitions the domain into a set of sub-regions that follow the crest lines of the effective potential, the domain is over-partitioned. It is therefore important to be able to identify which of these minima correspond to the localized eigenstates, and to merge the over partitioned sub-regions. Furthermore, there are also several sub-regions that do not correspond to a localized eigenstate at all, and these are referred to spurious regions.

Previous work [12] has outlined a procedure to accomplish this task. We will outline the key steps below. The first step is to partition the domain into sub-regions based on all the minimia of W. This is achieved via the standard watershed algorithm. The watershed algorithm emulates the gradual filling of basins with water and draws a crest line whenever water from two neighboring basins meet as depicted in Fig. 3.A.2.

We now have a set of watershed regions each separated by a boundary. There are three possible cases:

- The basin is deep enough to host a localized eigenstate, which means that the boundaries are high enough (to be defined below) compared to the minimum.
- The basin is not deep enough and can be merged with a neighboring basin

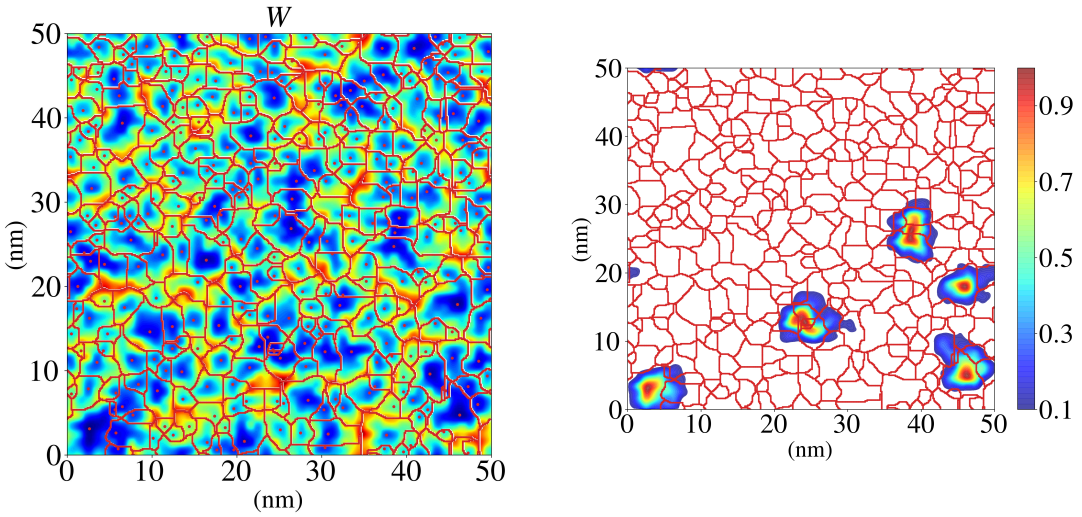

Figure 3.A.1: 2D color representation of the a) effective potential W; the naive watershed valley lines superimposed in red. b) The naive watershed valley lines of W and the first 5 eigenstates.

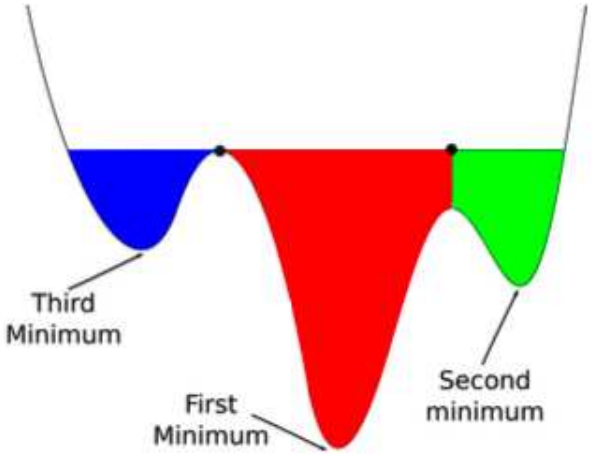

Figure 3.A.2: A schematic representation of how the watershed lines are computed. From [12].

which allows it to now host an eigenstate.

- The basin is not deep enough and it cannot be merged with any of the neighboring wells, since they are all independent wells or it does not satisfy the merging condition. This corresponds to a spurious basin.

The criteria to determine whether a basin is deep enough to host a localized eigenstate is based on the $1 + \frac{d}{4}$ rule introduced in section 3.1.2. If the value of the effective potential at the boundaries of a minimum is greater than the energy of the eigenstate, the eigenstate will be confined to that basin. Mathematically this translates to

$$E_i^0 < \min_{\partial\Omega_i} W \implies \left(1 + \frac{d}{4}\right) \times \min_{\Omega_i} W < \min_{\partial\Omega_i} W. \tag{3.52}$$

Furthermore, this allows us to specify the merging condition for two sub-regions as

$$\min_{\partial\Omega_i \cap \partial\Omega_j} W < \left(1 + \frac{d}{4}\right) \times \min_{\Omega_i \cup \Omega_j} W \tag{3.53}$$

where the inequality should be satisfied by the minima of both sub-regions. Below we outline an algorithm that was implemented to merge different sub-regions and to rank them as independent (capable of hosting a localized state) or spurious.

1. Have 3 lists – working, viable and spurious. Working initially contains all the minima in ascending order, viable and spurious are initially empty.
2. Find independent wells; wells that can host states by themselves without being merged, put these in the viable list, and remove from working.
3. Look at the lowest minimum remaining in the working list.
4. Check if this well is independent; if yes, remove from working, and add to viable.
5. If not, see if there are non-independent wells in the neighbors. If no; remove from working and add to spurious.
6. If there are non-independent neighbors, check whether the well can be merged.
7. If yes, merge and go to step 4.

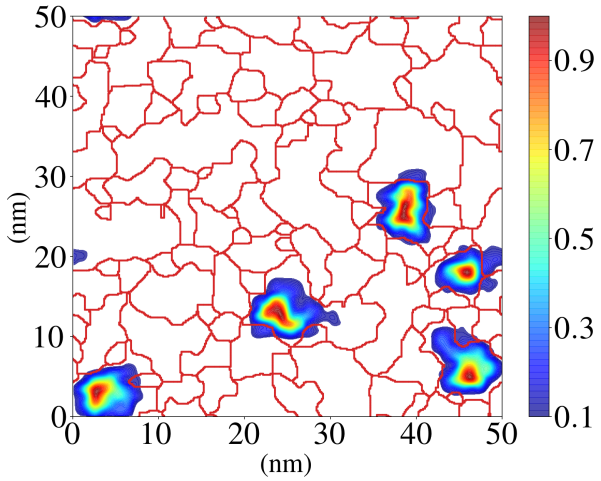

Figure 3.A.3: The adapted watershed lines of W and the first 5 eigenstates.

8. If no, remove from working, add to spurious and go to step 3.

The result is depicted in Fig. 3.A.3, where we can see that the eigenstates are more accurately partitioned by the crest lines. It is important to mention that this procedure which is based on the $1 + \frac{d}{4}$ rule is not perfect and one can sometimes overparition or underpartition the domain. Further improvements were suggested in Ref. [12] that relaxed the condition in Eq. 3.53 by replacing the minimum of the boundary by the minimum over an average over a certain length scale that corresponded to the wavelength of the modes. We assess the efficacy of the above algorithm at identifying the relevant sub-regions of localization for our domain. The sub-regions that are partitioned by the algorithm correspond to the locations of the localized fundamental modes of each basin. These "fundamental" modes are identified by the fact that they are 1. localized in the basin 2. do not oscillate in the basin, since that would correspond to an excited states. We therefore first identify such fundamental modes among the calculated eigenstates of the potential and evaluate how many can be correctly assigned to an identified sub-region. To that end, we evaluate the probability of the state to be confined in a given sub region Ω_i

$$P_i = \int_{\Omega_i} |\psi|^2 dr \tag{3.54}$$

We claim that an eigenstate is localized in Ω_i if $P_i > 0.9$ and furthermore, we

assign only one fundamental eigenstate to a sub-region, which helps us identify an underpartitioning of the domain or when multiple eigenstates are located in the same sub-region. Then we proceed to compare, what fraction of states are correctly assigned to their sub-regions before and after the merging process. We find for the potential in Fig. 3.1.1, that before the merging process, 12.5 % of the fundamental modes are correctly assigned to their sub-regions and after merging, 75 % of the fundamental modes are correctly assigned.

References

[1] M. Filoche and S. Mayboroda. "Universal Mechanism for Anderson and Weak Localization". In: *Proceedings of the National Academy of Sciences* 109.37 (Sept. 11, 2012), pp. 14761–14766. ISSN: 0027-8424, 1091-6490. DOI: 10.1073/pnas.1120432109.

[2] D. N. Arnold et al. "Effective Confining Potential of Quantum States in Disordered Media". In: *Phys. Rev. Lett.* 116.5 (Feb. 5, 2016), p. 056602. DOI: 10.1103/PhysRevLett.116.056602.

[3] D. N. Arnold et al. "Computing Spectra without Solving Eigenvalue Problems". In: *SIAM Journal on Scientific Computing* 41.1 (Jan. 2019), B69–B92. ISSN: 1064-8275, 1095-7197. DOI: 10.1137/17M1156721.

[4] S. Agmon. *Lectures on Exponential Decay of Solutions of Second-Order Elliptic Equations: Bounds on Eigenfunctions of N-Body Schrodinger Operations. (MN-29)*. en. ISBN: 978-1-4008-5307-6.

[5] P. D. Hislop and I. M. Sigal. *Introduction to Spectral Theory: With Applications to Schrödinger Operators*. Applied Mathematical Sciences. New York: Springer-Verlag, 1996. ISBN: 978-0-387-94501-9. DOI: 10.1007/978-1-4612-0741-2.

[6] M. Filoche et al. "Localization Landscape Theory of Disorder in Semiconductors. I. Theory and Modeling". In: *Physical Review B* 95.14 (Apr. 18, 2017). ISSN: 2469-9950, 2469-9969. DOI: 10.1103/PhysRevB.95.144204.

[7] M. Piccardo et al. "Localization Landscape Theory of Disorder in Semiconductors. II. Urbach Tails of Disordered Quantum Well Layers". In: *Physical Review B* 95.14 (Apr. 18, 2017). ISSN: 2469-9950, 2469-9969. DOI: 10.1103/PhysRevB.95.144205.

[8] C.-K. Li et al. "Localization landscape theory of disorder in semiconductors. III. Application to carrier transport and recombination in light emitting diodes". en. In: *Physical Review B* 95.14 (Apr. 2017). ISSN: 2469-9950, 2469-9969. DOI: 10.1103/PhysRevB.95.144206.

[9] E. Wigner. "On the Quantum Correction For Thermodynamic Equilibrium". In: *Physical Review* 40.5 (June 1932), pp. 749–759. DOI: 10.1103/PhysRev.40.749.

[10] J.-P. Banon et al. "Wigner-Weyl Description of Light Absorption in Disordered Semiconductor Alloys Using the Localization Landscape Theory". In: *Phys. Rev. B* 105.12 (Mar. 31, 2022), p. 125422. DOI: 10.1103/PhysRevB.105.125422.

[11] P. Pelletier et al. "Spectral Functions and Localization-Landscape Theory in Speckle Potentials". In: *Phys. Rev. A* 105.2 (Feb. 14, 2022), p. 023314. DOI: 10.1103/PhysRevA.105.023314.

[12] P. Desforges. "Analysis of the Spatial and Spectral Structures of Localized Eigenfunctions in Anderson Models through the Localization Landscape Theory". These de Doctorat. Institut polytechnique de Paris, Apr. 2021.

Chapter 4

Hopping transport

4.1 Introduction

Charge transport in semiconductors can be broadly classified into two regimes based on the degree of localization of the electronic states involved in the process, namely, *band transport* and *hopping transport*. If the electrons involved in the transport are delocalized Bloch waves, the transport mechanism is called band transport. If the electronic states involved in the transport are localized, and the charge carrier therefore hops between localized states, the mechanism is called hopping transport. Transport can also occur through a combination of both processes, and the dominant mechanism depends on the concentration of the carriers, the temperature of the sample, the degree of disorder, to name a few important parameters. Hopping transport is the relevant transport mechanism at low carrier concentrations and at low temperatures in disordered semiconductors, when an electron cannot be excited to a delocalized state and therefore must hop from one localized state to another [1].

Experimentally, the two mechanisms have different signatures. For example, the mobilities vary differently as functions of temperature and the applied electric field. Hopping mobilities often increase with temperature since the hopping is assisted by the vibrations of the crystal, whereas band transport mobilities often decrease with temperature since this process is inhibited by scattering on the crystal [2].

Disorder can induce localization of electronic states, a famous example of which

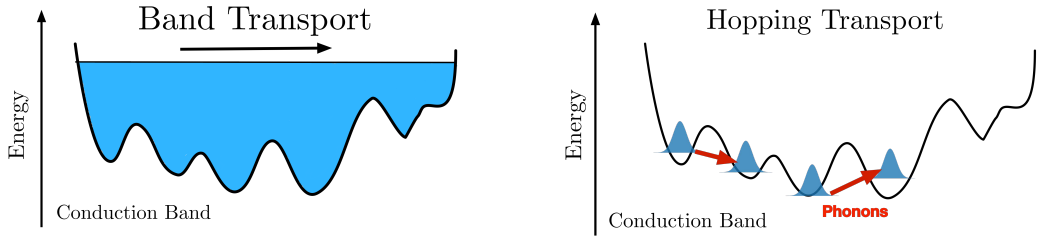

Figure 4.1.1: Sketches of the various modes of electronic transport: (Left) At high carrier concentrations and high temperatures, the electronic states are delocalized contributing to band transport. (Right) At low carrier concentrations and low temperatures, the electron hops from one localized state to another.

is Anderson localization [3], produced by a static disordered potential. In semiconductors, localization of electronic states can be induced by several mechanisms. A charge carrier can be localized by the interaction with its surrounding medium, thus forming a polaron [4, 5, 6]. Interactions between electrons [7, 8, 9], dynamic disorder, i.e., disorder induced by the thermal fluctuations of the lattice [10, 11] and static disorder [12], i.e., fluctuations in the potential are all possible origins for electronic localization.

Hopping transport is modeled by associating with each state an average occupation probability and between each pair of states, a hopping rate [13]. The dynamics of the process is governed by a master equation that tracks the rate of change of the average occupation probability for each state. The master equation must be solved for the steady state occupation probabilities, and for evaluating a steady state current. The hopping rates are computed by evaluating the electron-phonon interaction between each pair of states. This requires knowledge of the position and spatial extent of the wave functions for the electronic states, and of their respective energies. It also requires a suitable description of the phonons of the system. When the hops are due to acoustic phonons, the atomic displacements are described as long wavelength acoustic waves that can be related to the elastic strain of the crystal, as is described in deformation potential theory [14].

The above described quantities can be computed via *ab-initio* atomistic methods [15, 16, 17, 18] but these can be computationally intensive for systems of rea-

sonable size. It is more common to model such transport by assuming a certain distribution of electronic states in energy and space, and by assuming a certain functional form for the hopping rates between the localized states [19, 20, 21, 22, 23]. Traditionally the hopping rates are assumed to decrease exponentially with the distance between localized states, which is known as the Miller-Abrahams' (MA) model [24, 25] and the free parameters in the model are fitted against experimental mobility curves. One drawback of such an approach is that it assumes a single isotropic characteristic length for all electronic states at all energies. Vukmirovic et al. [26] showed via *ab-initio* calculations that the hopping rates can deviate significantly from the MA model because the MA model does not account for the complex overlaps between the wave functions of the associated electronic states.

In this chapter, we present an application of the Localization Landscape (LL) theory to model hopping transport in disordered semiconductors that bridges the gap between *ab-initio* atomistic calculations and empirical models such as the MA model. Our approach takes into account the static disorder of the potential, and allows us to access the localized wave functions without significant computational cost. As was seen in chapter 3, the solution to the LL equation enables us to define an *effective potential*, the valleys of which predict the regions of localization of the eigenstates, their energies and the exponential decay of the wave functions. This enables us to compute hopping rates between the localized states and consequently the mobility of the charge carrier as a function of the underlying disordered potential. We compare these computed mobilities with mobilities based on exact eigenstate computations for 2D disordered potentials and analyze the differences.

4.2 Hopping transport model

4.2.1 Master equation

Hopping transport is modeled as a series of jumps or hops between different hopping sites. Let us suppose that our system is composed of N sites and the state of the system is characterized by $n = \{n_1, n_2, .., n_N\}$, a set of N occupation numbers where n_i can either take a value of 1 or 0, referring to whether the ith site is occupied or unoccupied respectively. We consider the probability $P_n(t)$ to find the system at

time t in the state n. The rate of change of this probability is given by a master equation

$$\frac{dP_n(t)}{dt} = \sum_{n'} -W_{nn'}P_n(t) + W_{n'n}P_{n'}(t), \tag{4.1}$$

where $W_{nn'}$ are transition rates from state n to state n' that do not depend on time. The above master equation describes the dynamics of a Markov process, i.e, without memory. We have briefly outlined the derivation of such a master equation from the Schrödinger equation in chapter 1. The average occupation number $\bar{n}_i$ of any site i is given by

$$\bar{n}_i = \sum_n n_i P_n(t), \tag{4.2}$$

and the rate of change of the average occupation number is given by differentiating Eq. 4.2 and using Eq. 4.1

$$\frac{d\bar{n}_i}{dt} = \sum_{n,n'} W_{nn'}(n_i - n'_i)P_n(t). \tag{4.3}$$

We represent $W_{nn'}$ in terms of single particle transition rates w_{rs} between any two sites r, s and we have

$$W_{nn'} = \sum_{r,s} w_{rs}n_r(1-n'_r)(1-n_s)n'_s \prod_{l\neq r,s} \delta_{n_l n'_l} \tag{4.4}$$

where we impose that a transition occurs only between an occupied site r to an unoccupied site s and all other sites remain unchanged. Inserting 4.4 into 4.3, it is shown [27] that

$$\frac{d\bar{n}_i}{dt} = \sum_j -w_{ij}\overline{n_i(1-n_j)} + w_{ji}\overline{n_j(1-n_i)}, \tag{4.5}$$

where w_{ij} is the hopping rate from state i to state j. In what follows, we ignore correlations between the occupations of different sites assuming that $\overline{n_i.n_j} = \overline{n_i}.\overline{n_j}$ and we rename $\overline{n_i} = f_i$ which gives us

$$\frac{df_i}{dt} = \sum_j -w_{ij}f_i(1-f_j) + w_{ji}f_j(1-f_i) \tag{4.6}$$

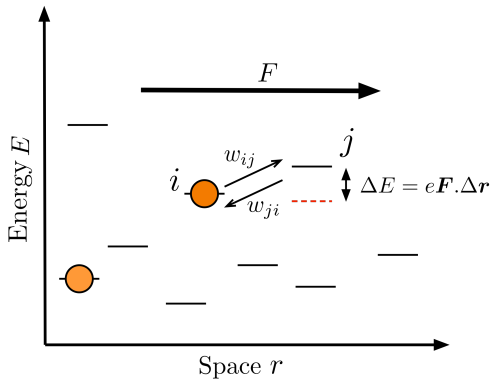

Figure 4.2.1: A schematic of the hopping states. The presence of a small field F shifts the energy difference between the states by an amount proportional to F.

At small carrier concentrations, it is unlikely for charges to interact with each other and so it is unlikely for the occupation probability at different sites to be correlated with each other. Ref. [28] has argued that there are small changes to the mobility if one accounts for the correlations between pairs of sites at large carrier densities. In this work, we limit ourselves to small carrier densities and therefore the above approximation is reasonable.

In the absence of an electric field, the above master equation is satisfied by the Fermi-Dirac statistics, and detailed balance is also verified. The presence of a small uniform field $\boldsymbol{F}$ shifts the energy difference between any two states as $\Delta E = E_j - E_i - e\boldsymbol{F} \cdot \boldsymbol{r}_{ij}$, where $\boldsymbol{r}_{ij} = \boldsymbol{r}_j - \boldsymbol{r}_i$ is the difference in positions of the two states and e is the charge of the carrier. In general, $e\boldsymbol{F} \cdot \boldsymbol{r}_{ij}$ is just the potential difference of the field $\boldsymbol{F}$ between the two sites. This results in a greater number of hops in the direction of the field, and the emergence of a net current. The steady state current passing through a surface s (assumed perpendicular to the x direction here) is calculated by solving for the steady state occupation probabilities $\{\bar{f}_i\}$, by setting the left-hand side of Eq. 4.6 to zero and then evaluating the current density J through

$$J = neL \sum_{\substack{i \\ x_i < x_s}} \sum_{\substack{j \\ x_j > x_s}} -w_{ij}\bar{f}_i(1-\bar{f}_j) + w_{ji}\bar{f}_j(1-\bar{f}_i). \tag{4.7}$$

where n is the carrier density and L is the length of the sample. The mobility μ is then given by $\mu = J/neF$. An equivalent expression for the mobility is obtained via

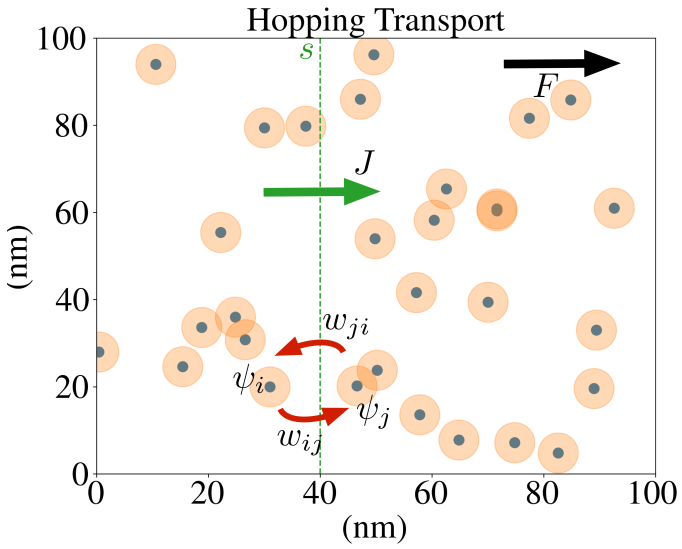

Figure 4.2.2: Schematic of hopping transport: the net current passing through the surface s (depicted by the green dotted line) is calculated by subtracting the net flow of charge to the left from the net flow of charge to the right.

the expression [29],

$$\mu = \frac{\langle v \rangle}{F} = \frac{\sum_i w_{ij} \bar{f}_i (1 - \bar{f}_j)(x_j - x_i)}{F \sum_i \bar{f}_i}. \tag{4.8}$$

4.2.2 Hopping rates

The hopping rates w_{ij} between any two states i and j in Eq. 4.6 is given by the Fermi golden rule

$$w_{ij} = \frac{2\pi}{\hbar} |\langle \Psi_j | \hat{H}_{el-ph} | \Psi_i \rangle|^2 \delta(E^j - E^i), \tag{4.9}$$

where Ψ_i refers to the wave function of the combined electron-phonon system. The complete Hamiltonian of the system can be written as follows

$$\hat{H} = \hat{H}_e + \hat{H}_p + \hat{H}_{ep}, \tag{4.10}$$

where $\hat{H}_e$ refers to the Hamiltonian for the electrons, $\hat{H}_p$ refers to the Hamiltonian of the phonons and $\hat{H}_{ep}$ refers to the Hamiltonian of the electron-phonon interaction. In second quantization, the Hamiltonian reads [30, 31]

$$\hat{H}_e = \sum_i E_i \hat{c}_i^\dagger \hat{c}_i, \tag{4.11}$$

$$\hat{H}_p = \sum_{\boldsymbol{q}} \hbar\omega_{\boldsymbol{q}} \hat{b}_{\boldsymbol{q}}^\dagger \hat{b}_{\boldsymbol{q}}, \tag{4.12}$$

$$\hat{H}_{ep} = \sum_{\boldsymbol{q}} \rho(\boldsymbol{q}) V_{ei}(\boldsymbol{q}) \boldsymbol{q} \cdot \zeta_{\boldsymbol{q}} \sqrt{\frac{\hbar}{2\rho_m V \omega_{\boldsymbol{q}}}} (\hat{b}_{\boldsymbol{q}} + \hat{b}_{-\boldsymbol{q}}^\dagger), \tag{4.13}$$

where $c_i^\dagger, c_i$ are the creation and annihilation operators for the electronic states, E_i is the energy of the electronic state, $\hat{b}_{\boldsymbol{q}}^\dagger \hat{b}_{\boldsymbol{q}}$ are the creation and annihilation operators for the phonon states, $\rho(\boldsymbol{q})$ is the particle density operator, $V_{ei}(\boldsymbol{q})$ is the electron-ion interaction potential, $\boldsymbol{\zeta_q}$ is the polarization vector of the phonon, ρ_m is the mass density, V is the volume of the crystal, $\omega_{\boldsymbol{q}}$ is the phonon angular frequency. The particle density operator is more explicitly

$$\rho(\boldsymbol{q}) = \sum_{i,j} \hat{c}_i^\dagger \hat{c}_j \int d\boldsymbol{r}\ e^{-i\boldsymbol{q}.\boldsymbol{r}}\ \psi_i^*(\boldsymbol{r}) \psi_j(\boldsymbol{r}). \tag{4.14}$$

We denote the integral in the above equation with $M_{ij}^{\boldsymbol{q}}$,

$$M_{ij}^{\boldsymbol{q}} = \int d\boldsymbol{r}\ e^{-i\boldsymbol{q}.\boldsymbol{r}}\ \psi_i^*(\boldsymbol{r}) \psi_j(\boldsymbol{r}) \tag{4.15}$$

The matrix element thus becomes

$$\langle \Psi_j | \hat{H}_{el-ph} | \Psi_i \rangle = \frac{1}{\sqrt{V}} \langle \Psi_j | \sum_{\boldsymbol{q},i,j} M_{ij}^{\boldsymbol{q}} V_{ei}(\boldsymbol{q}) \boldsymbol{q}.\zeta_{\boldsymbol{q}} \sqrt{\frac{\hbar}{2\rho_m \omega_{\boldsymbol{q}}}} \hat{c}_i^\dagger \hat{c}_j (\hat{b}_{\boldsymbol{q}} + \hat{b}_{-\boldsymbol{q}}^\dagger) | \Psi_i \rangle \,. \tag{4.16}$$

The initial and final states of the electron-phonon system, Ψ_i and Ψ_j can be written as $\Psi_i = |n_{\boldsymbol{q}}, \psi_i\rangle$ and $\Psi_j = |n_{\boldsymbol{q}} \pm 1, \psi_j\rangle$, where $n_{\boldsymbol{q}}$ refers to the quantum number of the phonon states. The phonon part of the Hamiltonian only has non vanishing

matrix elements for

$$\langle n_{\boldsymbol{q}} - 1|\hat{b}_{\boldsymbol{q}}|n_{\boldsymbol{q}}\rangle = \sqrt{n_{\boldsymbol{q}}}, \tag{4.17}$$

$$\langle n_{\boldsymbol{q}} + 1|\hat{b}^{\dagger}_{\boldsymbol{q}}|n_{\boldsymbol{q}}\rangle = \sqrt{n_{\boldsymbol{q}} + 1}. \tag{4.18}$$

Evaluating the sum in Eq. 4.16 gives us for the hopping rate

$$w_{ij} = \frac{2\pi}{\hbar}\frac{1}{V}\sum_{\boldsymbol{q}} \frac{\hbar}{2\rho_m \omega_{\boldsymbol{q}}}|M^{\boldsymbol{q}}_{ij}|^2 |V_{ei}(\boldsymbol{q})\boldsymbol{q}\cdot\boldsymbol{\zeta_q}|^2 \Big\{n_B + \frac{1}{2} \pm \frac{1}{2}\Big\}\delta(E_j - E_i \pm \hbar\omega_q). \tag{4.19}$$

In the above expression, weassume Bose-Einstein statistics for the phonons, implying

$$\bar{n}_{\boldsymbol{q}} = n_B = \frac{1}{e^{\beta\hbar\omega_{\boldsymbol{q}}} - 1}, \tag{4.20}$$

where $\beta = 1/k_B T$ and k_B is the Boltzmann constant and T is the temperature of the system. Acoustic phonons follow a linear dispersion relation

$$\omega_q = c_s q, \tag{4.21}$$

where c_s is the speed of sound in the system. In deformation potential theory [14]

$$V_{ei}(\boldsymbol{q})\boldsymbol{q}\cdot\zeta_{\boldsymbol{q}} = \sum_{ij} D_{ij}(q_i\zeta_j), \tag{4.22}$$

where D_{ij} is the deformation potential associated with the various components of the strain tensor. Here we consider the simplest case of an isotropic crystal with scattering in Γ valley. The above expression can be written as [32]

$$V_{ei}(\boldsymbol{q})\boldsymbol{q}\cdot\zeta_q = Dq. \tag{4.23}$$

Converting the sum over $\boldsymbol{q}$ into an integral, we have

$$\lim_{V\to\infty}\frac{1}{V}\sum_{\boldsymbol{q}} f(\boldsymbol{q}) = \int \frac{d\boldsymbol{q}}{(2\pi)^3} f(\boldsymbol{q}). \tag{4.24}$$

Plugging the above expression into Eq. 4.19 we get for the hopping rate in 2D

$$w_{ij} = \frac{D^2 q_0^2}{8\pi^2 \rho_m^{2D} \hbar c_s^2} |M_{ij}^{q_0}|^2 \Big\{ n_B + \frac{1}{2} \pm \frac{1}{2} \Big\} \tag{4.25}$$

and in 3D

$$w_{ij} = \frac{D^2 q_0^3}{8\pi^2 \rho_m^{3D} \hbar c_s^2} |M_{ij}^{q_0}|^2 \Big\{ n_B + \frac{1}{2} \pm \frac{1}{2} \Big\}, \tag{4.26}$$

where $q_0 = |E_j - E_i|/\hbar c_s$. We are interested in understanding how the quantity $M_{ij}^{q_0}$ behaves for localized states, and whether this behaviour can be reproduced using predictions from LL theory.

4.2.3 Miller-Abrahams' model

Hopping transport was initially studied in the context of hopping between impurity states in silicon by Miller and Abrahams (MA) [24, 33]. The localized states were assumed to be hydrogen-like envelope functions of the form

$$F(\boldsymbol{r}) = \sqrt{\frac{1}{\pi a^3}} e^{-\frac{r}{a}} \tag{4.27}$$

where $a = \frac{\hbar^2 \kappa}{me^2}$ is an effective Bohr radius, κ is the dielectric constant of the medium and m is the effective mass of the charge carrier. The hopping rates between donors due to acoustic phonons were calculated via deformation potential theory,

$$w_{ij} = w_0 \exp\left(-\frac{2r_{ij}}{a} \right) n_B(E_j - E_i), \tag{4.28}$$

where n_B again refers to the Bose-Einstein statistics, and

$$w_0 = \frac{D^2 |E_j - E_i|}{\pi \rho c^5 \hbar^4} \left(\frac{2e^2}{3\kappa a} \right)^2 \frac{r_{ij}^2}{a^2}, \tag{4.29}$$

where the symbols have the same signification as in Eq. 4.25. We stress that one major difference in the above expression as derived by Miller and Abrahams, and the current work is that we consider eigenstates of the same Hamiltonian and therefore we have $\langle \psi_i | \psi_j \rangle = 0$, whereas in the MA model $\langle \psi_i | \psi_j \rangle \neq 0$. In fact, the MA

derivation neglects the integral $\langle\psi_i|e^{i\boldsymbol{q}.\boldsymbol{r}}|\psi_j\rangle$, which in our derivation is the only contribution. The MA model is often used in other kinds of systems [19, 20, 21, 22, 23] to describe hopping transport between localized states where the average transition rate w_{ij} between any two localized states i and j is given by

$$w_{ij} = \begin{cases} w_0 \exp\{-\dfrac{2r_{ij}}{a} - \dfrac{E_j - E_i}{k_B T}\} & \text{if } E_j > E_i \\ w_0 \exp\{-\dfrac{2r_{ij}}{a}\} & \text{else.} \end{cases} \tag{4.30}$$

One notes that the above expression has two principal contributions, one spatial due to the distance r_{ij} between hopping states, and the other energetic, due to the difference of energies $E_j - E_i$ between the states. In the absence of an electric field, the above master equation is satisfied by the Fermi-Dirac statistics, and furthermore, detailed balance is verified for the MA rates, which implies $w_{ij} f_i(1-f_j) = w_{ji} f_j(1-f_i)$ for every pair of sites. In the presence of a small electric field F (small compared to the potential responsible for the localization), we assume that the localized states are not altered, and that the energies are modified by $e\boldsymbol{F}\cdot\boldsymbol{r}_i$, giving us a modified transition rate of

$$w_{ij}^F = w_0 \exp\{-\frac{2r_{ij}}{a} - \frac{E_j - E_i - e\boldsymbol{F}\cdot\boldsymbol{r_{ij}}}{k_B T}\}. \tag{4.31}$$

The above asymmetry in hopping rates gives rise to a net current in the presence of a field.

4.3 LL theory

In this section, we illustrate how we use predictions from LL theory to assess the above described hopping transport parameters. First, we consider a 2D disordered potential as depicted in Fig. 4.3.1 for which we compute the exact eigenstates and energies by solving the Schrödinger eigenvalue problem and then proceed to calculate the hopping rates and mobility. We then compute the effective potential derived from LL theory to assess the locations and energies of the localized eigenstates. We proceed to compute the effective potential-based Agmon distance to estimate the

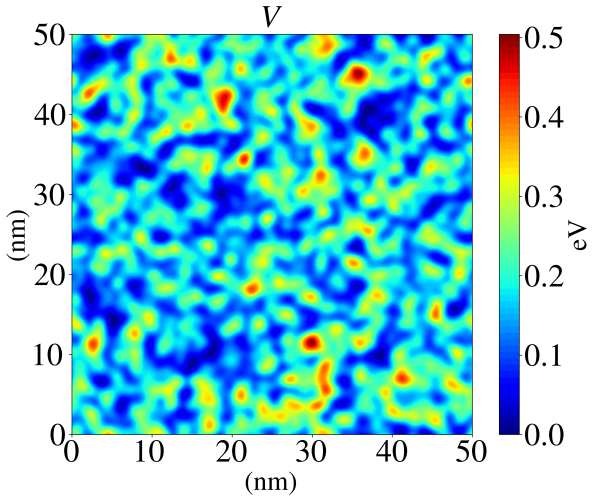

Figure 4.3.1: A 2D alloy-type disordered potential on a square of size 50 nm with a maximum potential value of 500 meV. The details of how this potential was generated is given in Appendix 4.A.

exponential decay of the localized states. The hopping network thus recreated using LL theory is compared with the exact eigenstate-based hopping network.

4.3.1 Eigenstate computations

The disordered potential in Fig. 4.3.1 was generated using a procedure outlined in Appendix 4.A. The maximum potential amplitude is 500 meV over a 2D domain of 50 nm x 50 nm. The eigenvalue problem was discretized using the finite element method [34], and the eigenstates and eigenvalues of the potential in Fig. 4.3.1 were calculated using the SLEPc solver [35], which implemented the Krylov-Schur method. The system was solved with polynomials of degree 1 on a mesh of size [400 x 400] and in Fig. 4.3.2, we plot a few examples of the eigenstates. We notice that the eigenstates are very localized to begin with and as the energy increases, they tend to delocalize.

One way to characterize the localization or delocalization of an eigenstate is by looking at the inverse participation ratio (IPR) defined as

$$IPR = \frac{\int |\psi(\boldsymbol{r})|^4 d\boldsymbol{r}}{|\int |\psi(\boldsymbol{r})|^2 d\boldsymbol{r}|^2}. \tag{4.32}$$

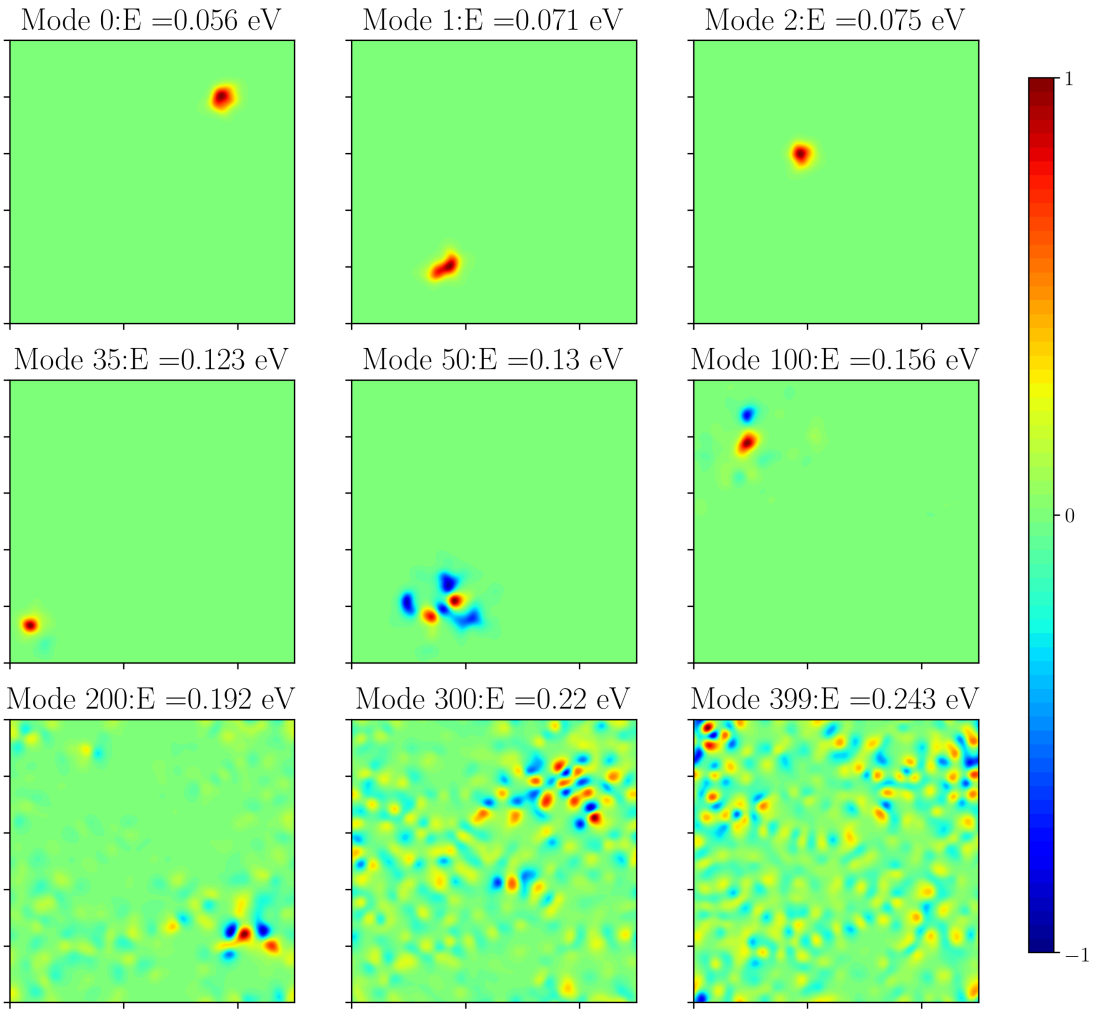

Figure 4.3.2: A few eigenstates of the potential in Fig. 4.3.1.

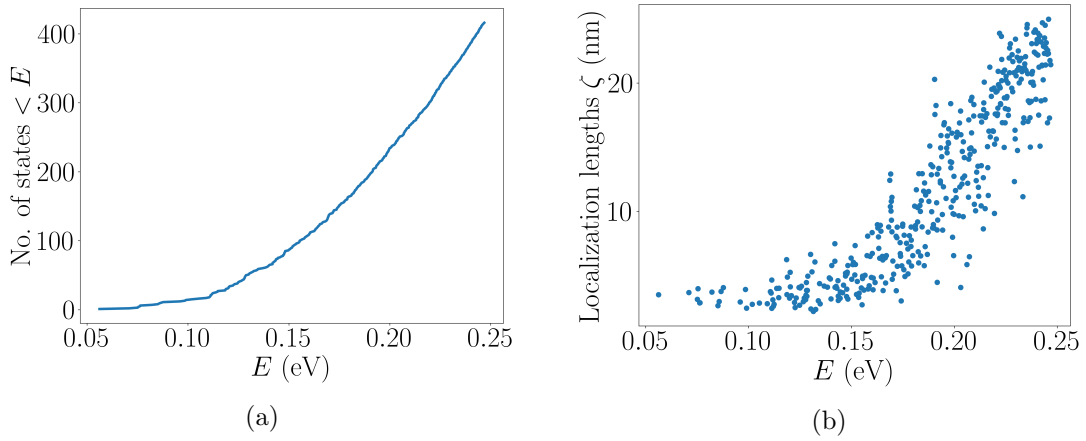

Figure 4.3.3: a) The integrated density of states for the potential in Fig. 4.3.1. b) The localization length of the eigenstates as a function of their energy.

If the wave function in the above expression is $\mathcal{L}^2$ normalized, the IPR is just $\int |\psi(\boldsymbol{r})|^4 d\boldsymbol{r}$. If an eigenstate is completely delocalized, say a constant over the entire domain, the IPR will take a minimum value of L^{-d}, where L is the lateral size of the domain. Conversely, if an eigenstate is very localized, essentially supported over the length scale of the discretization of the mesh, it will take a maximum value of δL^{-d} where δL is the length scale of the mesh. The IPR is thus related to the localization length ζ in 2D as $\zeta = \sqrt{1/IPR}$. In Fig. 4.3.3 we plot the localization lengths of the first 400 eigenstates. We notice that the states delocalize with increasing energy.

We use these eigenstates to compute the hopping rates for each pair of states. In Fig 4.3.4, we plot the hopping rates for the first 100 and first 400 eigenstates as a function of the distance r_{ij} between the states. We note that the hopping rates decrease exponentially with the distance between the states, which reflects the exponential decay of the localized eigenstates. Furthermore, one notes a larger mass of points towards the upper right corner for the plot with 400 states. This is because the hopping rates decrease slower with distance for the states with higher energy which again reflects the fact that the eigenstates delocalize with energy.

4.3.2 Effective potential W

We are interested in seeing how much of the information about the energies, localization lengths and hopping rates can be extracted by the LL-based effective potential

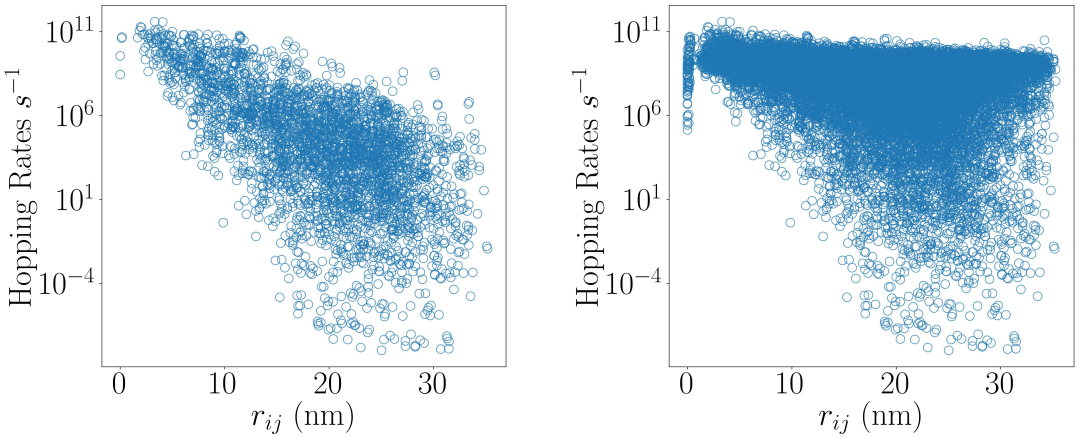

(a) First 100 eigenstates

(b) First 400 eigenstates

Figure 4.3.4: The hopping rates computed using Eq. 4.25 as a function of the distance between the exact eigenstates. The distance between the states is defined as the distance between the positions of the maxima of the eigenstates considered. The quantities are calculated for the following parameters as defined in Eq. 4.25 : $D = 8.3\,\text{eV}$, $c_s = 10^4\,\text{ms}^{-1}$, $\rho_{2D} = 6150\,\text{kgm}^{-3} \times 50\text{nm}$.

W. The LL equation ($\hat{H}u = 1$) is solved using the finite element method and in Fig. 4.3.5, we plot the effective potential $W = 1/u$. The basins of this effective potential correspond to the locations of the eigenstates. We first determine how many eigenmodes are accounted for, using the adapted watershed algorithm, described in the appendix of the previous chapter. Indeed, assuming that there is one eigenstate at each minimum leads to poor results since there are many spurious minima, as can be seen in Fig. 4.3.6.

We wish to estimate how many states can be reliably predicted with the minima of the effective potential. Since we can only predict the fundamental modes, we first count how many of the 400 eigenstates are fundamental modes. There is no rigorous definition of what constitutes a fundamental mode but one way to define such a mode is to solve the Schrödinger equation over the reduced sub-region Ω_i, and calculate the fundamental mode of $\hat{H}$ over this sub-domain. However since this would be cumbersome to calculate, we instead use a simpler heuristic, which is based on the observation that the fundamental modes are usually mostly positive or negative bumps which only oscillate outside the sub-region, as can be seen for mode 0, 1, 2 and 35, and which is clearly not the case for mode 100, 200, 300 and 399

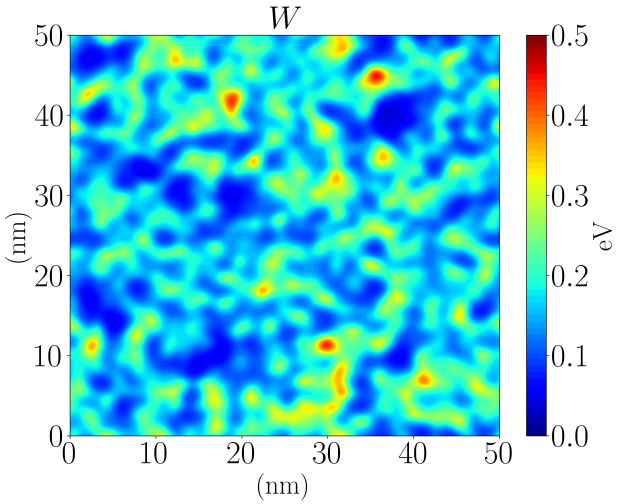

Figure 4.3.5: The effective potential W for the potential depicted in Fig. 4.3.1

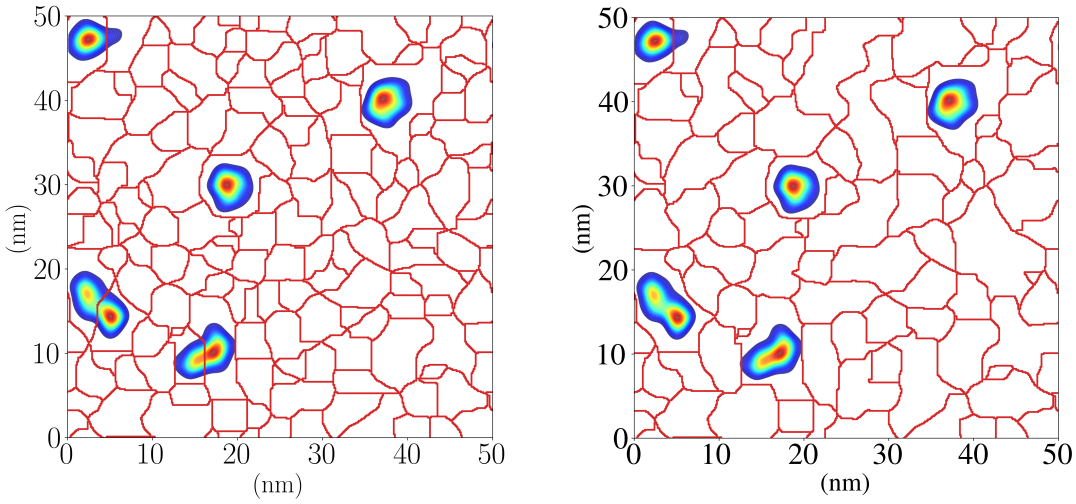

Figure 4.3.6: a) The naive watershed algorithm that over-partitions the domain b) Adapted watershed algorithm that merges basins that host localized eigenstates.

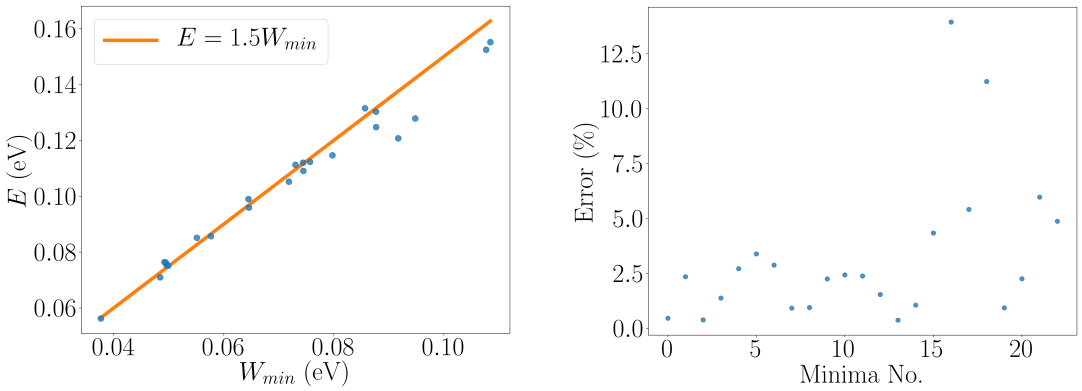

(a) (b)

Figure 4.3.7: a) Energies of the eigenstates as a function of the corresponding minimum of the effective potential. b) The error defined as $|E - (1.5 \times W_{min})|/E$ for the different states.

in Fig. 4.3.2. A quick and dirty heuristic for identifying a fundamental mode is if $0.1 \max \psi > \min |\psi|$. We identify 27 (23 were correctly identified by W) fundamental modes by applying the above criterion. The key point is the formalism described below applies only to the fundamental modes of the basin delineated by the valley lines of the effective potential, and these fundamental modes are essentially bumps.

We verify the $1 + \frac{d}{4}$ rule in Fig. 4.3.7, where the ratio of the energy of eigenstate to the value of the minima at the effective potential are plotted. In Fig. 4.3.8, we plot the same for 10 different realizations of the alloy-type potential. The error in the exact energy and the energy estimate predicted by the effective potential differ by around 10 percent.

Now we proceed to calculate the shapes of the eigenstates and the exponential decay with the Agmon distance $\rho_E(\boldsymbol{r}, \boldsymbol{R})$, computed from each minimum $\boldsymbol{R}$ to every other point $\boldsymbol{r}$ in the domain. The Agmon distance is defined as a minimum over all paths connecting $\boldsymbol{R}$ to $\boldsymbol{r}$ of the integral of $\sqrt{[W - E]_+}$. This can be efficiently calculated using the fast marching method [36, 37], which is explained in more detail in Appendix 4.B. The Agmon distance constraints eigenstate through the inequality

$$|\psi(\boldsymbol{r})| \lesssim e^{-\rho_E(\boldsymbol{r}, \boldsymbol{R})}. \tag{4.33}$$

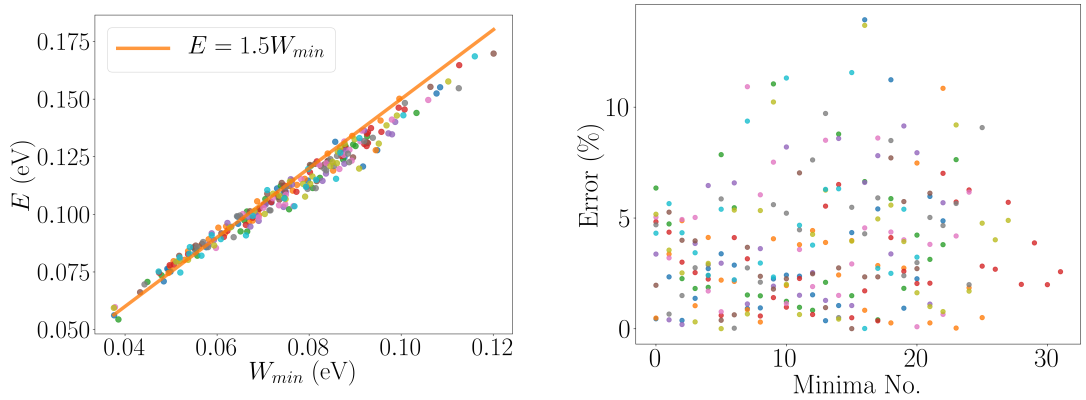

Figure 4.3.8: a) The energies of the eigenstates as a function of the corresponding minimum of the effective potential for 10 different realizations of alloy-type disordered potential. b) The error defined as $|E - (1.5 \times W_{min})|/E$ for the states in (a). The different colors correspond to different realizations.

We use the Agmon distance to construct estimations of the eigenstates ψ_i^W as follows

$$\psi_i^W(\boldsymbol{r}) = \begin{cases} u(\boldsymbol{r}) & \text{where } W(\boldsymbol{r}) < \bar{E}_i \text{ in the} \\ & \text{basin containing } \boldsymbol{R}_i. \\ \dfrac{1}{\bar{E}_i} e^{-\rho_{\bar{E}_i}(\boldsymbol{r}, \boldsymbol{R}_i)} & \text{else,} \end{cases} \tag{4.34}$$

with a suitable normalization constant. The central bump of the localized state ψ_i is proportional to $u(\boldsymbol{r}) = 1/W(\boldsymbol{r})$ in the corresponding basin of $W(\boldsymbol{r})$. To the corresponding basin, we stitch the exponential tail derived from the Agmon distance. We plot an example of the first eigenstate in Fig. 4.3.9.

To quantify the error in the exact eigenstate wave function and the effective potential based state, we compute the $\mathcal{L}^2$ norm of the difference $\psi - \psi^W$ (themselves being $\mathcal{L}^2$ normalized) and we plot this in Fig. 4.3.11. The discrepancy in the wave functions is very large and even approaches the maximal value of $\sqrt{2} \approx 1.41$, which would be the case for two orthogonal functions. In Fig. 4.3.12, we plot an example of such a poorly reproduced state where the discrepancy is rather evident, even if the location and general shape of the state is still reproduced. We also compare the hopping rates thus calculated with the hopping rates from the exact eigenstates.

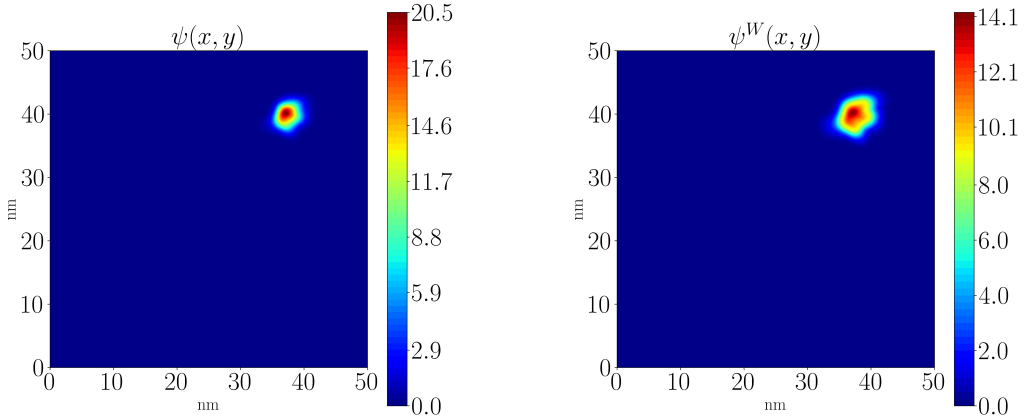

(a) First eigenstate

(b) The W-based estimate of the first eigenstate

Figure 4.3.9: Comparison of the first eigenstate and its W-based estimate according to Eq. 4.34.

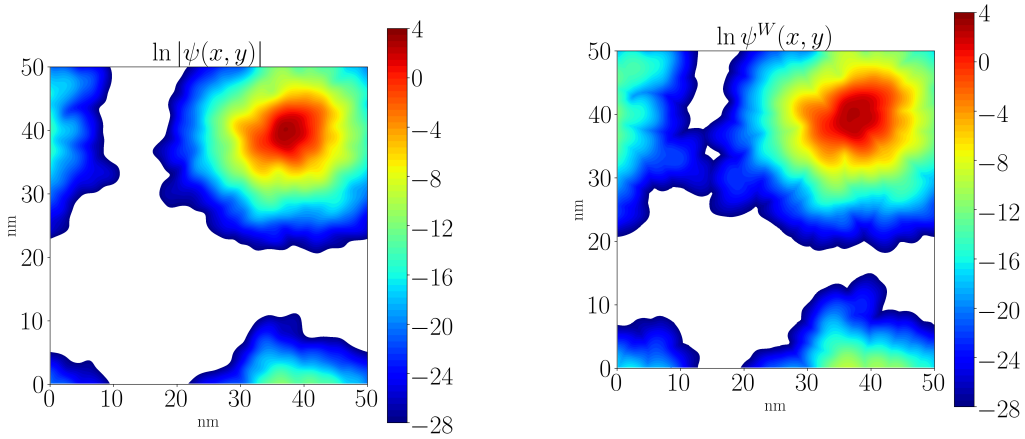

(a) The first eigenstate

(b) The W-based estimate estimate of the first eigenstate

Figure 4.3.10: Comparison of the first eigenstate and its W-based estimate according to Eq. 4.34 in log scale.

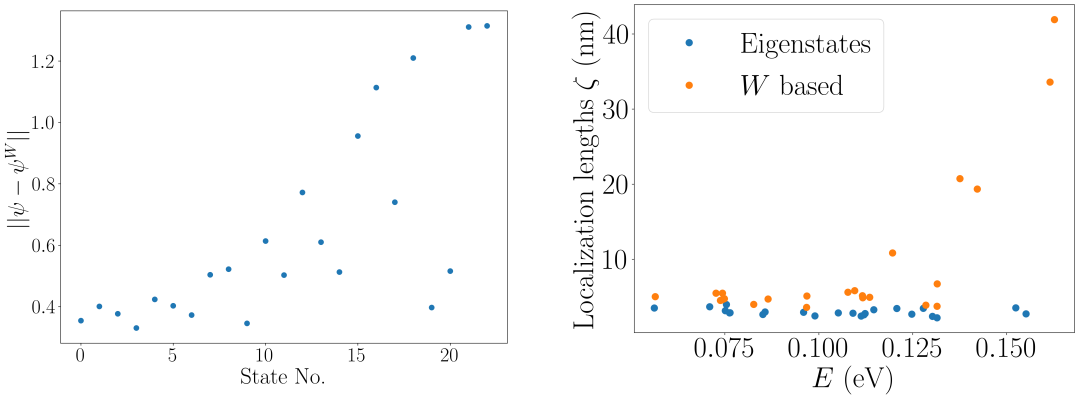

Figure 4.3.11: a) The norm of the error in the eigenstate and the effective potential based state. b) Comparison of the localization lengths of the eigenstates and their corresponding effective potential based state.

As can be seen from Fig 4.3.13, the distribution of states is much larger than the cloud for the exact eigenstates, and this is because in general the Agmon estimates from the effective potential are much more delocalized compared to the eigenstates, which can be confirmed in Fig. 4.3.11 where we have plotted the localization lengths of the states.

To explain this error, we point out that the Agmon distance bounds the exponential decay based on the path that minimizes the integral of $\sqrt{[W-E]_+}$, whereas a more accurate bound might be obtained by having a weighted sum of the different paths through a path integral formulation. The degree to which the reconstructed state "sees" the effective potential depends on the energy of the state, in the $\sqrt{[W(\boldsymbol{r})-E]_+}$ term. If the energy is too high, the effective potential has little confining effect and will consequently be far too delocalized, which is the case for $E = 1.5 \times W_{min}$. Strictly speaking, Agmon's inequality only holds when E_i is the exact energy of the state which is well approximated by $E = 1.5 \times W_{min}$. Numerically, we observe one can get a tighter bound by using a smaller value for the energy. We thus draw a distinction between the energy E_i of the state and the energy $\bar{E}_i$ that goes into the Agmon distance expression. We have opted to label different $\bar{E}_i$ as a factor with respect to the corresponding minima of the effective potential $W(\boldsymbol{R}_i)$. In Figs. 4.3.14-4.3.16, we plot the error in the wave functions for six different values

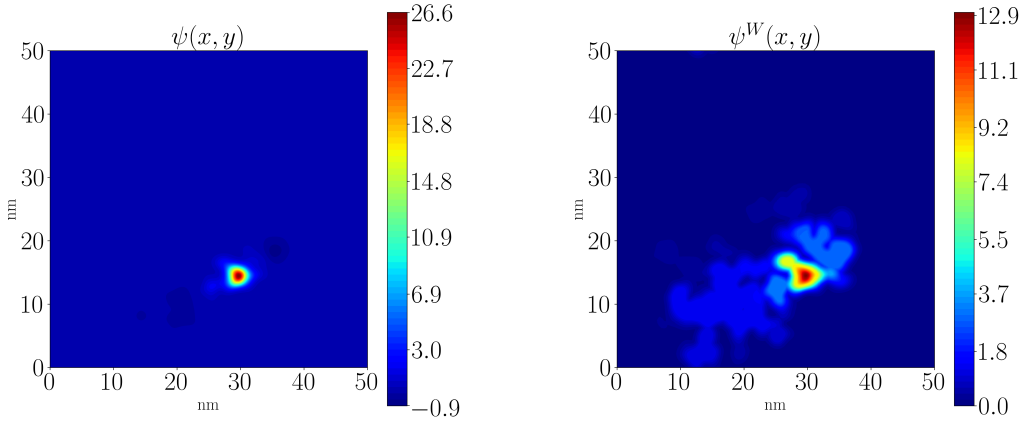

(a) The 39th eigenstate

(b) The W-based estimate

Figure 4.3.12: Comparison of the 39th eigenstate and its W-based estimate. One can observe that the W-based estimate is much more delocalized compared to the exact eigenstate.

of the factor = 1.0, 1.1, 1.2, 1.3, 1.4 and 1.5. We observe that the difference in the norm of $\mathcal{L}^2$ norm is lowest for $\bar{E}_i = 1.0 \times W(\boldsymbol{R}_i)$. However the hopping rates are best reproduced by $\bar{E}_i = 1.2 \times W(\boldsymbol{R}_i)$. These seemingly contradictory observations can be explained by the fact the $\mathcal{L}^2$ norm is sensitive to the part of the eigenfunction that is large (the "bumps") whereas the hopping rates also depend on the exponential tails. We will therefore proceed below by using $\bar{E}_i = 1.2 \times W(\boldsymbol{R}_i)$ since the hopping rates are more relevant while trying to reproduce the hopping network.

At this point, we emphasize the importance of the Agmon distance as the more relevant metric in understanding the spatial dependence of the exact hopping rates. We evaluate the quantity M_{ij} defined as

$$M_{ij} = \int d\bar{\boldsymbol{q}} | \int d\boldsymbol{r} e^{-iq_0 \bar{\boldsymbol{q}}.\boldsymbol{r}} \psi_i^*(\boldsymbol{r}) \psi_j(\boldsymbol{r})|^2 \tag{4.35}$$

where $\bar{\boldsymbol{q}}$ is a unit vector along the wave vector $\boldsymbol{q}$. The hopping rate is given by

$$w_{ij} = \frac{D^2 q_0^2}{8\pi^2 \rho_m^{2D} \hbar c^2} M_{ij} \Big\{ n_B + \frac{1}{2} \pm \frac{1}{2} \Big\} \tag{4.36}$$

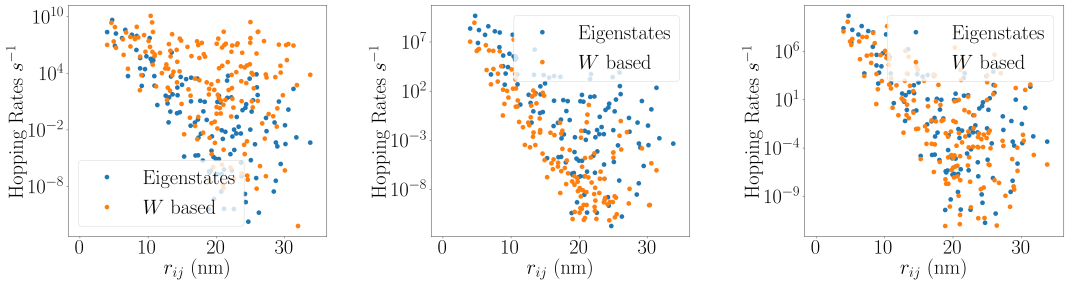

(a) $\bar{E} = 1.5 \times W_{min}$ (b) $\bar{E} = 1.0 \times W_{min}$ (c) $\bar{E} = 1.2 \times W_{min}$

Figure 4.3.13: A comparison of the hopping rates calculated for the eigenstates and their corresponding effective potential based approximations for different factors in $\bar{E} = factor \times W_{min}$.

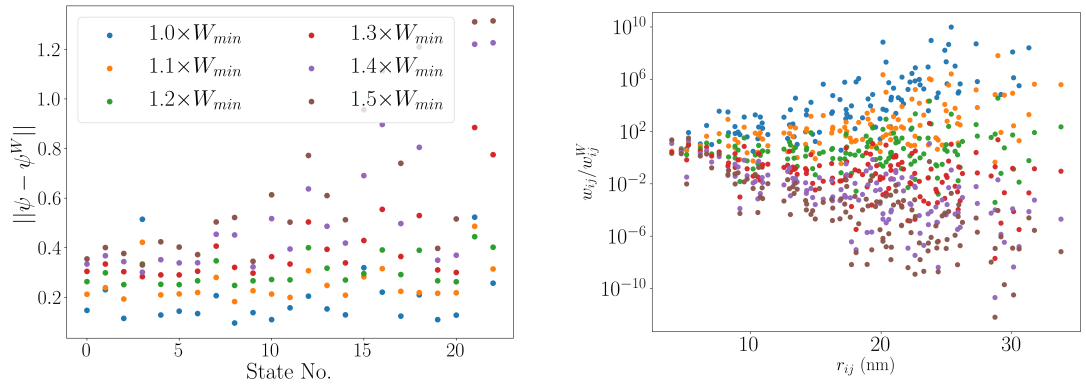

(a) (b)

Figure 4.3.14: a) The norm of $\psi - \psi^W$ for different factors in $\bar{E} = factor \times W_{min}$. b) The ratio of hopping rates $\frac{w_{ij}}{w_{ij}^W}$ as a function of the distance between the states for different factors. The legend is the same as in Fig. 4.3.14a.

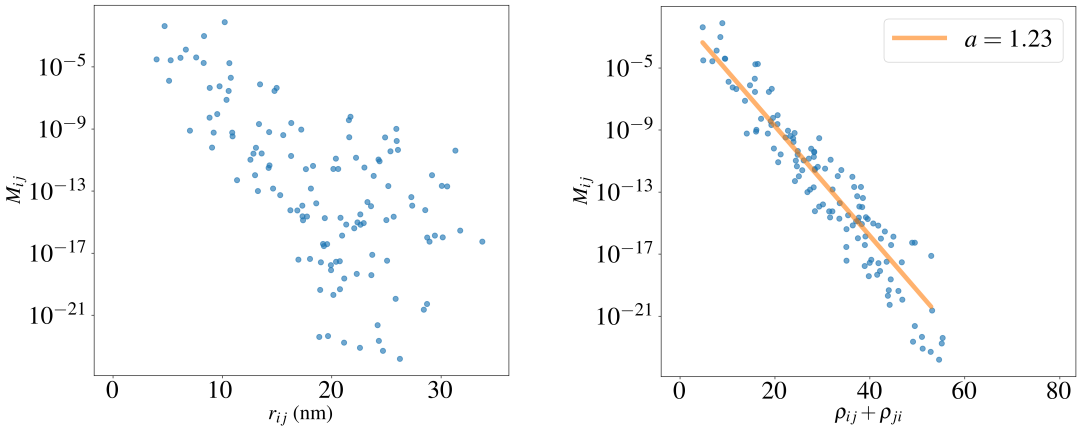

(a) (b)

Figure 4.3.15: The spatial part of the coupling term M_{ij} calculated for the exact eigenstates plotted as a) a function of the distance and b) as a function of the sum of the effective potential based Agmon distances.

and so M_{ij} as defined in Eq. 4.35 represents the spatial overlap of the eigenstates in the expression for the hopping rate. In Fig. 4.3.15 we plot M_{ij} for the exact eigenstates as a function of the real distance r_{ij} and the sum of the Agmon distances between the two corresponding minima, $\rho_{\bar{E}_i}(\boldsymbol{R}_j, \boldsymbol{R}_i) + \rho_{\bar{E}_j}(\boldsymbol{R}_i, \boldsymbol{R}_j)$. We observe that the variation of M_{ij} plotted as a function of the Agmon distance is much lesser than the variation of M_{ij} plotted as a function of the true distance r_{ij}. In Fig. 4.3.15, we plot M_{ij} for one realization and in Fig. 4.3.16 for 10 realizations.

Furthermore, we perform an exponential fit between the M_{ij} and the sum of the Agmon distances, a being the fitting parameter,

$$M_{ij} = \exp\left\{ -\frac{\rho_{\bar{E}_i}(\boldsymbol{R}_i, \boldsymbol{R}_j) + \rho_{\bar{E}_j}(\boldsymbol{R}_j, \boldsymbol{R}_i)}{a} \right\} \tag{4.37}$$

as shown in Figs. 4.3.15, 4.3.16.

4.3.3 Mobility computations

Now that we have established that the hopping rates computed from the exact eigenstates and W agree best for $\bar{E} = 1.2 \times W_{min}$, we proceed to calculate the carrier mobility for a given disordered potential. This involves solving the master

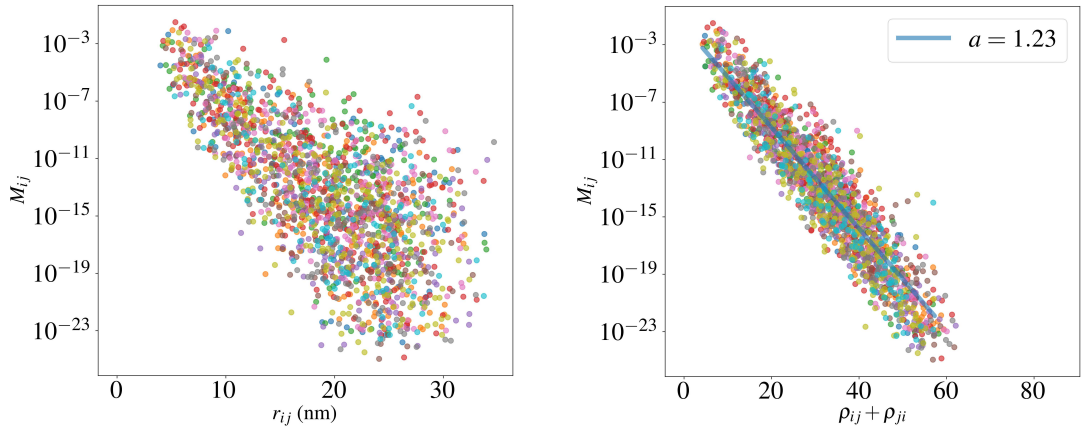

(a) (b)

Figure 4.3.16: The spatial part of the coupling term M_{ij} calculated for the exact eigenstates for 10 realizations plotted as a) a function of the distance, and b) as a function of the sum of the effective potential based Agmon distances. The different colors correspond to different realizations.

equation for $\{\bar{f}_i\}$ such that

$$\sum_j -w_{ij}\bar{f}_i(1-\bar{f}_j) + w_{ji}\bar{f}_j(1-\bar{f}_i) = 0. \tag{4.38}$$

Furthermore, an initial carrier concentration needs to be specified. This is done by specifying a Fermi level E_F, which fixes the carrier concentration of the system at a given temperature via the Fermi-Dirac statistics as

$$\sum_i f_i^0 = \sum_i \frac{1}{1+e^{\beta(E_i-E_F)}}. \tag{4.39}$$

The steady state occupation probabilities in Eq. 4.38 can be solved by several approaches. The first is to explicitly solve the above system of equations, which are non-linear in f_i, using the Newton-Raphson method [29]. This approach can be memory-intensive for large systems. A second approach is to reach the steady state statistics of the involved states using a Monte-Carlo simulation. This approach can be extended to larger systems as it is less memory-intensive but may require longer simulation time to converge. A third approach to calculate the mobility is to reformulate the master equation to represent an effective resistor network, and therefore

to calculate the resistance of the hopping network, currents and mobility [24].

In this work, we will use the first and third approach. First, the master equation is solved using the Newton-Raphson method. The Newton-Raphson method involves finding the vector $\bar{\boldsymbol{f}} = \{\bar{f}_1, \bar{f}_2, .., \bar{f}_n\}$ such that

$$\boldsymbol{G}(\bar{\boldsymbol{f}}) = 0, \tag{4.40}$$

where $\boldsymbol{G}$ designates the system of master equations described in Eq. 4.38. The current at arbitrary points on the domain is calculated as

$$J = neL \sum_{\substack{i \\ x_i<x_s}} \sum_{\substack{j \\ x_j>x_s}} -w_{ij}\bar{f}_i(1-\bar{f}_j) + w_{ji}\bar{f}_j(1-\bar{f}_i). \tag{4.41}$$

The mobility is evaluated through

$$\mu = \frac{\langle v \rangle}{F} = \frac{J}{neF}. \tag{4.42}$$

We must also understand the number of states involved in the hopping process. The periodic boundary conditions impose that any pair of states cannot be separated by a distance greater than $L/2$ since, otherwise, the direction of the hop would be ambiguous. This imposes a maximum localization length of the state $\sim L/2$. Beyond this length, one would need to go to larger domain sizes. In Fig 4.3.17, we plot the computed mobility as a function of the temperature for different number of states. We note that computing the mobility at the highest temperatures requires at least 200 eigenstates. Furthermore, we point out that the mobility calculated for only the fundamental modes is much lower than the mobility calculated using the 200 states for $T > 30K$. At higher temperatures the excited states also contribute to the transport, and are therefore not accounted for by the aforementioned effective potential based states described above.

In addition, we plot in Fig. 4.3.17b the mobility as a function of the temperature for 10 different realizations of the alloy-type potential profile. We note the large variance of the mobility curves especially at low temperatures. This occurs because the system is not large enough to capture the hops at low temperatures. The simulations are extremely sensitive to the few states involved and also to the particular

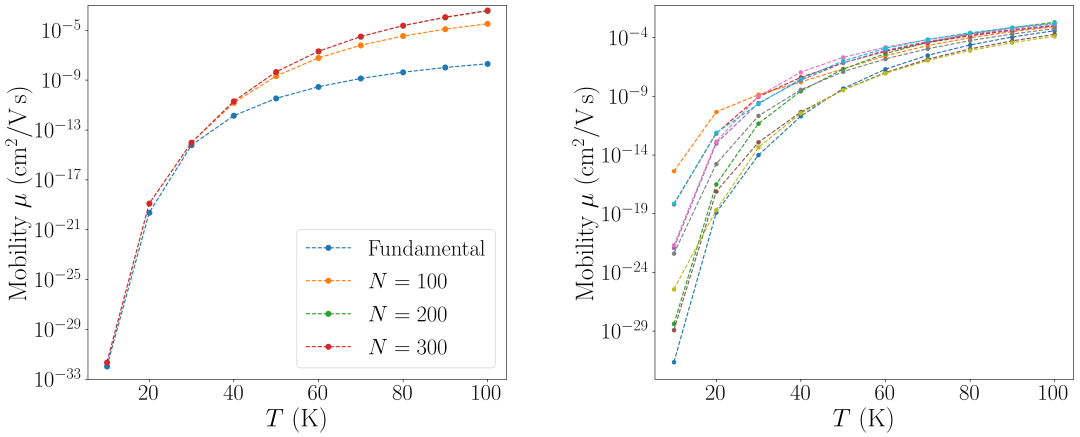

(a) Exact eigenstates

(b) Exact eigenstates

Figure 4.3.17: a) The computed hopping mobility as a function of the temperature for a varying number of eigenstates considered. We note the difference in mobility for the fundamental modes and for $N = 200$. b) The mobility as a function of temperature for 10 different realizations of the disordered potential.

details of each realization. To understand why this would be more pronounced at lower temperatures, it helps to consider the Miller-Abrahams' model in Eq. 4.30. The hopping rate contains two primary contributions, the exponential dependence in spatial coordinates and the exponential dependence in energy. When the temperature is low, the hopping rate is no longer dominated by the spatial coordinates, since the exponential decay of the energy term becomes comparable with the spatial term. Therefore, a hop can occur further away than the nearest neighbors, and this regime is called variable-range hopping. To obtain reliable mobility curves at such low temperatures, one must consider much larger systems, for example domains of size 500 nm [31]. However, for such large systems it becomes progressively more difficult to compare the exact eigenstates.

Since we are interested in whether we are able to reproduce the hopping network correctly, we now turn to the third approach described above, which is to compute the effective resistor network. In this section, we consider a larger square domain of size 100 nm in order to study a larger network. The presence of a small electric field induces a small shift in the occupation probabilities $\bar{f}_i = f_i^0 + \delta f_i$, altering the hopping rates such that $w_{ij} = w_{ij}^0 + \delta w_{ij}$. Putting these expressions into Eq. 4.38,

and only keeping terms linear in F yields

$$\sum_j \{w_{ij}^0(1-f_i^0)+w_{ji}^0 f_i^0\}\delta f_j - \{w_{ji}^0(1-f_j^0)+w_{ij}^0 f_j^0\}\delta f_i = \frac{w_{ij}^0 f_i^0(1-f_j^0)}{k_B T}(e\boldsymbol{F}\cdot\boldsymbol{r}_{ij}). \tag{4.43}$$

The left-hand side can be interpreted as the net current that flows between sites i and j, while the right-hand side is proportional to the potential difference between sites i and j. The conductance between sites i and j can be therefore read as

$$G_{ij} = \frac{e^2 w_{ij}^0 f_i^0(1-f_j^0)}{k_B T}. \tag{4.44}$$

The overall conductance of the network is often evaluated using percolation arguments. The conductance of the network will be dominated by the critical conductance G_c, which is the largest value of the conductance such that the subset of resistors with $G_{ij} > G_c$ still contains a connected network which spans the domain from left to right [38]. The critical conductance determines the conductance of the network because the resistors with $G_{ij} \gg G_c$ will form isolated regions of high conductivity. These isolated regions will be connected by a small network of resistors of order G_c to span the entire system, thereby limiting the conductance. The resistors with $G_{ij} \ll G_c$ will not affect the total conductance much. In Fig. 4.3.18, we show that the critical conductance is 10^{-23} Sm, below which the domain is disconnected. In Fig. 4.3.18-4.3.19 we plot the critical conductance for the exact eigenstates and the W-based states as a function of temperature, for one realization of the potential. We plot the ratio of critical conductances computed from the exact eigenstates to the W-based states as a function of the temperature in Fig. 4.3.20.

4.4 Conclusion

In this chapter, we have addressed the applicability of modeling hopping transport using the LL theory. We have performed exact eigenstate-computations for a disordered potential and calculated the corresponding hopping rates. Then we compared these hopping rates with hopping rates computed for states estimated with the LL-based effective potential W. We noted that the states thus reconstructed were able

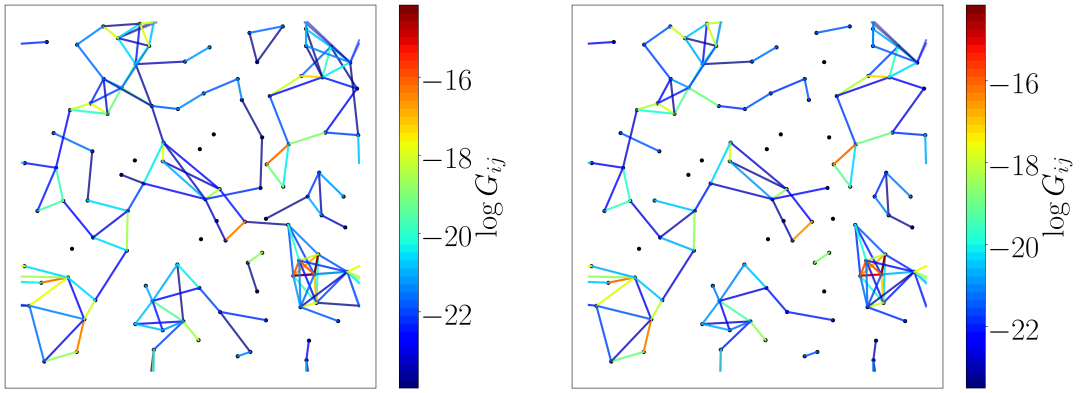

(a) Exact eigenstates (b) Exact eigenstates

Figure 4.3.18: a) The hopping network G_{ij} plotted in log scale for $T = 30\,\mathrm{K}$. The critical conductance $G_c = 10^{-23}\,\mathrm{Sm}$. We plot all resistors with $G_{ij} \geq G_c$ b) The same network as a) but plotted with for $G_{ij} > G_c$. One can see that the network is no longer percolating.

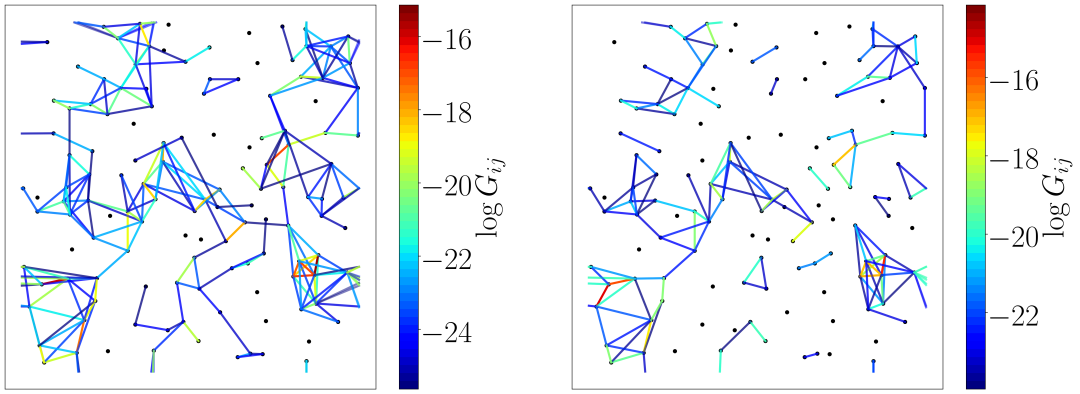

(a) W-based states (b) W-based states

Figure 4.3.19: a) The W-based hopping network corresponding to the network in Fig. 4.3.18. The critical conductance $G_c = 10^{-25}\,\mathrm{Sm}$. b) The same network plotted as a) but with the same scale as Fig. 4.3.18a.

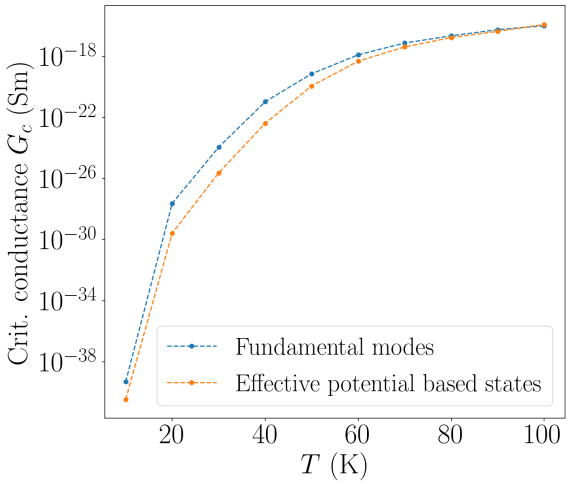

Figure 4.3.20: The critical conductance as a function of temperature computed for the eigenstate and W-based hopping network.

to reproduce the exponential decay of the localized states, and we quantified the error in this approximation. Furthermore, it seems that the W-based Agmon metric required a slightly lower energy to better account for the exponential decay. The above defined procedure was applicable only to the fundamental modes of the disordered potential. We then computed the hopping mobility for the exact eigenstates and we first showed that for the disordered potentials considered, at temperatures $T > 40\,\mathrm{K}$, the excited states (which are not accounted for by our W-based approximation) are involved in the hopping process. We then compared the effective conductance network for the exact eigenstate fundamental modes and the W-based states. We were able to qualitatively reproduce the hopping network using LL theory, however we do not expect this to work particularly well quantitatively. As described in the chapter, at low temperatures, the hops tend to be further away and the error in the W-based rates was showed to increase with the distance between the states. However, the W-based states correctly account for the states involved, since at low temperatures, we expect only the fundamental modes to contribute to the transport. At higher temperatures, the excited states will dominate the transport, and these are not accounted for by W-based method presented here.

Appendix

4.A Alloy type potential

In this part, I describe how the given disordered potentials are generated. This kind of potential simulates an alloy of type A_pB_{1-p} where A and B refers to the two different chemical species of the alloy, and p refers to the probability of finding species A. Using this, one can construct a 2D lattice as shown in Fig. 4.A.1 with lattice constant a where each lattice point $r_i = (x_i, y_i) = (a_0 + ma, a_0 + na)$ is either an atom A with probability p or an atom B with probability $1 - p$. The subset of indices i for which r_i is an atom of A is X_A and the set of indices of all latice points is X. The local concentration of A is defined as

$$C_A(r) = \frac{\sum_{i \in X_A} \exp -\frac{(r-r_i)^2}{\sigma^2}}{\sum_{i \in X} \exp -\frac{(r-r_i)^2}{\sigma^2}} \tag{4.45}$$

where σ is a smoothing length scale. The potential $V(r)$ is a linear scaling to this

$$V(r) = V_0 \times C_A(r) \tag{4.46}$$

For the potentials presented in this chapter, we use the parameters as follows: lattice constant $a = 0.5\,\mathrm{nm}$, $p = 0.2$, and $V_0 = 0.5\,\mathrm{eV}$.

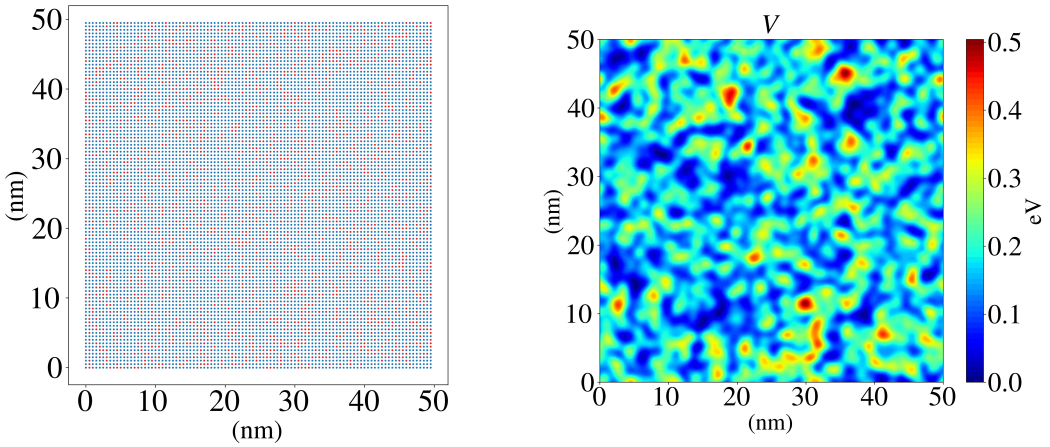

(a) (b)

Figure 4.A.1: a) Representation of a lattice of a binary alloy A_pB_{1-p} with lattice constant $a = 0.5\,\text{nm}$ and $p = 0.2$. b) The potential V generated with the procedure described in Sec. 4.A.

4.B Agmon distance computation

In the following section, we present some details for the Agmon distance computations. The Agmon distance between two points $\boldsymbol{x_0}, \boldsymbol{x_1}$ is defined as

$$\rho_E(\boldsymbol{x_0}, \boldsymbol{x_1}) = \min_{\gamma} \int_{\gamma} \sqrt{\frac{2m}{\hbar^2}(W(\boldsymbol{x}) - E)_+} ds \tag{4.47}$$

where γ is a path connecting $\boldsymbol{x_0}$ to $\boldsymbol{x_1}$. The level set $\rho_E(\boldsymbol{x_0}, \boldsymbol{x_1}) = C$ is the set of all points in the domain that can be reached with an Agmon distance of C. The minimal paths are orthogonal to the level curves, which gives us

$$|\nabla \rho_E(\boldsymbol{x_0}, \boldsymbol{x})| = \sqrt{\frac{2m}{\hbar^2}(W(\boldsymbol{x}) - E)_+}. \tag{4.48}$$

The above expression takes the form of an eikonal equation, which is typically encountered in wave propagation problems. Generally, the eikonal equation is of the form,

$$|\nabla u(\boldsymbol{x})| T(\boldsymbol{x}) = 1, \tag{4.49}$$

where $u(\boldsymbol{x}) = 0$ defines the shape of the initial wavefront, and $T(\boldsymbol{x})$ is the speed of the wavefront. We therefore use an eikonal equation solver that implements the fast marching method to compute the Agmon distance. One can rewrite the Agmon distance expression in the form defined above as,

$$|\nabla \rho_E(\boldsymbol{x_0}, \boldsymbol{x})| \frac{1}{\sqrt{\frac{2m}{\hbar^2}(W(\boldsymbol{x}) - E)_+}} = 1. \tag{4.50}$$

Since the form in equation 4.49 is the standard implementation of eikonal equation solvers, it impossible to have $\sqrt{(W(\boldsymbol{x}) - E)_+} = 0$ in equation 4.50 because this gives a divide by 0 error. This is the case for a point x_0 inside the zero level set for $W(\boldsymbol{x}) - E$. We therefore define ρ_E^{num} as

$$\rho_E^{num}(\boldsymbol{x_0}, \boldsymbol{x_1}) = \min_{\gamma} \int_{\gamma} \sqrt{\frac{2m}{\hbar^2}(g(W(\boldsymbol{x}) - E))} ds \tag{4.51}$$

where

$$g(x) = \begin{cases} c & \text{where } x < c \\ x & \text{else} \end{cases} \tag{4.52}$$

for some small positive c (In this work, we use $c = 10^{-3}$. This allows us to circumvent the divide by zero problem but introduces a small but negligible error in the computation for the distance.

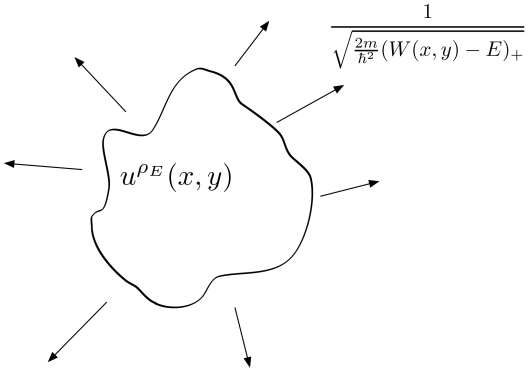

Figure 4.B.1: A schematic of the Agmon distance as a propagating wave front.

References

[1] S. Baranovskii and O. Rubel. "Charge Transport in Disordered Materials". en. In: *Springer Handbook of Electronic and Photonic Materials*. Ed. by S. Kasap and P. Capper. Cham: Springer International Publishing, 2017, pp. 1–1. ISBN: 978-3-319-48931-5 978-3-319-48933-9. DOI: 10.1007/978-3-319-48933-9_9.

[2] S. Giannini, A. Carof, and J. Blumberger. "Crossover from Hopping to Band-Like Charge Transport in an Organic Semiconductor Model: Atomistic Nonadiabatic Molecular Dynamics Simulation". en. In: *The Journal of Physical Chemistry Letters* 9.11 (June 2018), pp. 3116–3123. ISSN: 1948-7185. DOI: 10.1021/acs.jpclett.8b01112.

[3] P. W. Anderson. "Absence of Diffusion in Certain Random Lattices". In: *Physical Review* 109.5 (Mar. 1, 1958), pp. 1492–1505. ISSN: 0031-899X. DOI: 10.1103/PhysRev.109.1492.

[4] T. Holstein. "Studies of polaron motion: Part II. The "small" polaron". en. In: *Annals of Physics* 8.3 (Nov. 1959), pp. 343–389. ISSN: 0003-4916. DOI: 10.1016/0003-4916(59)90003-X.

[5] B. Rice et al. "Polaron States in Fullerene Adducts Modeled by Coarse-Grained Molecular Dynamics and Tight Binding". en. In: *The Journal of Physical Chemistry Letters* 9.22 (Nov. 2018), pp. 6616–6623. ISSN: 1948-7185. DOI: 10.1021/acs.jpclett.8b02320.

[6] H. Oberhofer, K. Reuter, and J. Blumberger. "Charge Transport in Molecular Materials: An Assessment of Computational Methods". en. In: *Chemical Reviews* 117.15 (Aug. 2017), pp. 10319–10357. ISSN: 0009-2665, 1520-6890. DOI: 10.1021/acs.chemrev.7b00086.

[7] A. L. Efros and B. I. Shklovskii. "Coulomb Gap and Low Temperature Conductivity of Disordered Systems". In: *J. Phys. C: Solid State Phys.* 8.4 (Feb. 21, 1975), pp. L49–L51. ISSN: 0022-3719. DOI: 10.1088/0022-3719/8/4/003.

[8] T. Giamarchi and H. J. Schulz. "Anderson localization and interactions in one-dimensional metals". en. In: *Physical Review B* 37.1 (Jan. 1988), pp. 325–340. ISSN: 0163-1829. DOI: 10.1103/PhysRevB.37.325.

[9] P. Sierant, D. Delande, and J. Zakrzewski. "Many-body localization due to random interactions". en. In: *Physical Review A* 95.2 (Feb. 2017), p. 021601. ISSN: 2469-9926, 2469-9934. DOI: 10.1103/PhysRevA.95.021601.

[10] A. Troisi, D. L. Cheung, and D. Andrienko. "Charge Transport in Semiconductors with Multiscale Conformational Dynamics". en. In: *Physical Review Letters* 102.11 (Mar. 2009), p. 116602. ISSN: 0031-9007, 1079-7114. DOI: 10.1103/PhysRevLett.102.116602.

[11] A. Troisi and D. L. Cheung. "Transition from dynamic to static disorder in one-dimensional organic semiconductors". en. In: *The Journal of Chemical Physics* 131.1 (July 2009), p. 014703. ISSN: 0021-9606, 1089-7690. DOI: 10.1063/1.3167406.

[12] M. Filoche et al. "Localization Landscape Theory of Disorder in Semiconductors. I. Theory and Modeling". In: *Physical Review B* 95.14 (Apr. 18, 2017). ISSN: 2469-9950, 2469-9969. DOI: 10.1103/PhysRevB.95.144204.

[13] B. I. Shklovskii and A. L. Efros. *Electronic Properties of Doped Semiconductors*. Red. by M. Cardona, P. Fulde, and H.-J. Queisser. Vol. 45. Springer Series in Solid-State Sciences. Berlin, Heidelberg: Springer Berlin Heidelberg, 1984. ISBN: 978-3-662-02405-8 978-3-662-02403-4. DOI: 10.1007/978-3-662-02403-4.

[14] J. Bardeen and W. Shockley. "Deformation Potentials and Mobilities in Non-Polar Crystals". In: *Phys. Rev.* 80.1 (Oct. 1, 1950), pp. 72–80. ISSN: 0031-899X. DOI: 10.1103/PhysRev.80.72.

[15] M. Mladenović and N. Vukmirović. "Charge Carrier Localization and Transport in Organic Semiconductors: Insights from Atomistic Multiscale Simulations". In: *Adv. Funct. Mater.* 25.13 (Apr. 2015), pp. 1915–1932. ISSN: 1616301X. DOI: 10.1002/adfm.201402435.

[16] J. A. Chan, J. Z. Liu, and A. Zunger. "Bridging the Gap between Atomic Microstructure and Electronic Properties of Alloys: The Case of (In,Ga)N". In: *Phys. Rev. B* 82.4 (July 15, 2010), p. 045112. DOI: 10.1103/PhysRevB.82.045112.

[17] A. Massé et al. “Ab Initio Charge-Carrier Mobility Model for Amorphous Molecular Semiconductors”. In: *Phys. Rev. B* 93.19 (May 19, 2016), p. 195209. DOI: 10.1103/PhysRevB.93.195209.

[18] A. Massé et al. “Effects of Energy Correlations and Superexchange on Charge Transport and Exciton Formation in Amorphous Molecular Semiconductors: An *Ab Initio* Study”. In: *Phys. Rev. B* 95.11 (Mar. 31, 2017), p. 115204. ISSN: 2469-9950, 2469-9969. DOI: 10.1103/PhysRevB.95.115204.

[19] J. O. Oelerich et al. “Field Dependence of Hopping Mobility: Lattice Models against Spatial Disorder”. In: *Phys. Rev. B* 96.19 (Nov. 21, 2017), p. 195208. ISSN: 2469-9950, 2469-9969. DOI: 10.1103/PhysRevB.96.195208.

[20] A. V. Nenashev et al. “Percolation Description of Charge Transport in Amorphous Oxide Semiconductors”. In: *Phys. Rev. B* 100.12 (Sept. 12, 2019), p. 125202. ISSN: 2469-9950, 2469-9969. DOI: 10.1103/PhysRevB.100.125202.

[21] W. F. Pasveer et al. “Unified Description of Charge-Carrier Mobilities in Disordered Semiconducting Polymers”. In: *Phys. Rev. Lett.* 94.20 (May 23, 2005), p. 206601. ISSN: 0031-9007, 1079-7114. DOI: 10.1103/PhysRevLett.94.206601.

[22] S. D. Baranovskii et al. “Charge-Carrier Transport in Disordered Organic Solids”. In: *Phys. Rev. B* 62.12 (Sept. 15, 2000), pp. 7934–7938. DOI: 10.1103/PhysRevB.62.7934.

[23] M. C. J. M. Vissenberg and M. Matters. “Theory of the Field-Effect Mobility in Amorphous Organic Transistors”. In: *Phys. Rev. B* 57.20 (May 15, 1998), pp. 12964–12967. DOI: 10.1103/PhysRevB.57.12964.

[24] A. Miller and E. Abrahams. “Impurity Conduction at Low Concentrations”. In: *Phys. Rev.* 120.3 (Nov. 1, 1960), pp. 745–755. ISSN: 0031-899X. DOI: 10.1103/PhysRev.120.745.

[25] T. Kasuya and S. Koide. “A Theory of Impurity Conduction. II”. In: *Journal of the Physical Society of Japan* 13.11 (1958), pp. 1287–1297. DOI: 10.1143/JPSJ.13.1287.

[26] N. Vukmirović and L.-W. Wang. "Carrier Hopping in Disordered Semiconducting Polymers: How Accurate Is the Miller–Abrahams Model?" In: *Appl. Phys. Lett.* 97.4 (July 26, 2010), p. 043305. ISSN: 0003-6951, 1077-3118. DOI: 10.1063/1.3474618.

[27] L. Bányai and A. Aldea. "Master Equation Approach to the Hopping Transport Theory". In: *Fortschritte der Physik* 27.9 (1979), pp. 435–462. ISSN: 1521-3978. DOI: 10.1002/prop.19790270903.

[28] J. Cottaar and P. A. Bobbert. "Calculating Charge-Carrier Mobilities in Disordered Semiconducting Polymers: Mean Field and Beyond". In: *Phys. Rev. B* 74.11 (Sept. 19, 2006), p. 115204. DOI: 10.1103/PhysRevB.74.115204.

[29] F. Jansson. "Charge Transport in Disordered Materials". In: (), p. 92.

[30] G. D. Mahan. *Many-Particle Physics*. Boston, MA: Springer US, 2000. ISBN: 978-1-4419-3339-3 978-1-4757-5714-9. DOI: 10.1007/978-1-4757-5714-9.

[31] D. Watson-Parris. "Carrier Localization in InGaN/GaN Quantum Wells". Ph.D Thesis, University of Manchester, 2011.

[32] B. K. Ridley. *Quantum Processes in Semiconductors*. Fifth Edition. Oxford, New York: Oxford University Press, Aug. 8, 2013. 450 pp. ISBN: 978-0-19-967722-1.

[33] T. Kasuya. "A Theory of Impurity Conduction I". In: *Journal of the Physical Society of Japan* 13.10 (Oct. 1958), pp. 1096–1110. ISSN: 0031-9015. DOI: 10.1143/JPSJ.13.1096.

[34] A. Logg, K.-A. Mardal, and G. Wells, eds. *Automated Solution of Differential Equations by the Finite Element Method: The FEniCS Book*. Lecture Notes in Computational Science and Engineering. Berlin Heidelberg: Springer-Verlag, 2012. ISBN: 978-3-642-23098-1. DOI: 10.1007/978-3-642-23099-8.

[35] V. Hernandez, J. E. Roman, and V. Vidal. "SLEPc: A Scalable and Flexible Toolkit for the Solution of Eigenvalue Problems". In: *ACM Trans. Math. Softw.* 31.3 (Sept. 1, 2005), pp. 351–362. ISSN: 0098-3500. DOI: 10.1145/1089014.1089019.

[36] J. A. Sethian. "A Fast Marching Level Set Method for Monotonically Advancing Fronts." In: *Proceedings of the National Academy of Sciences* 93.4 (Feb. 20, 1996), pp. 1591–1595. ISSN: 0027-8424, 1091-6490. DOI: 10.1073/pnas.93.4.1591.

[37] R. Kimmel and J. A. Sethian. "Computing Geodesic Paths on Manifolds". In: *Proceedings of the National Academy of Sciences* 95.15 (July 21, 1998), pp. 8431–8435. ISSN: 0027-8424, 1091-6490. DOI: 10.1073/pnas.95.15.8431.

[38] V. Ambegaokar, B. I. Halperin, and J. S. Langer. "Hopping Conductivity in Disordered Systems". In: *Phys. Rev. B* 4.8 (Oct. 15, 1971), pp. 2612–2620. ISSN: 0556-2805. DOI: 10.1103/PhysRevB.4.2612.

Chapter 5

Conclusion and perspectives

In this manuscript, we have addressed the question of electronic transport in disordered semiconductors. In the first chapter, we outlined the general theories of electronic transport starting from completely quantum mechanical theories to the different semi-classical approaches. We then summarized how various types of disorder can affect the transport mechanisms and their parameters.

In the second chapter, we described our work on electronic transport in the space charge regime. The space charge regime refers to situations when there are non-negligible electrostatic fields in a semiconductor altering the current flow. Treating this case required numerically solving Poisson's equation for the electrostatic potential in addition to the drift-diffusion and current conservation equations. We discretized the relevant equations using the Scharfetter-Gummel scheme which is a modified finite difference method in 1D. We were able to explain the experimentally observed regimes of the I-V curves, the switching of the carrier currents from a bipolar regime to a unipolar hole regime. Furthermore, we showed the dependence of the electronic transport on the electrostatic fields of the carriers and also on the recombination effects of the traps. This work resulted in the publication of a paper titled "Piezoresistance in Defect-Engineered Silicon" [1].

In addition, we outlined the equations to be solved for the small signal analysis of the system which is to understand the response of the charge carries to an alternating signal. This is important in the context of understanding the impedance spectroscopy measurements on defect engineered samples [2].

In chapter 3, we outlined the major developments of the localization landscape (LL) theory, which allows us to treat the quantum effects of disorder in semiconductor systems. LL theory defines an effective potential that predicts the energies and locations of the localized eigenstates. Previous work had shown that the integration of LL theory with the aforementioned drift-diffusion-Poisson system of equations. It thus accounted for the localization of charge carriers due to disorder and the effect of localization on the transport parameters. Further developments led to the LL-based Wigner-Weyl approach where the effective potential was used to calculate the phase space occupation of the eigenstates of a disordered potential. The effective potential also enables the definition of a metric called the Agmon distance that bounds the exponential decay of the eigenstates, whose applicability had not been studied in the context of transport.

In chapter 4, we studied the applicability of the effective-potential-based Agmon distance in modeling hopping transport. Hopping transport occurs when a charge carrier hops between localized electronic states at low enough carrier concentrations and low enough temperatures. The hopping network is characterized by the localization lengths of the states, their energy levels and the subsequent hopping rates between the different states. We performed exact eigenstate-computations for a disordered potential and calculated the corresponding hopping rates. We then compared the exact eigenstate-based hopping rates with hopping rates computed for states estimated with the LL-based effective potential. We noted that the states thus reconstructed were able to reproduce the exponential decay of the localized states, and we quantified the error in this approximation. The above defined procedure was applicable only to the fundamental modes of the disordered potential. We then compared the hopping mobilities between the exact eigenstates and the LL-based states. In this regard, we first showed that for the potentials considered, at temperatures around 30-40 K, the excited states (which are not accounted for by our effective potential based approximation) are involved in the hopping process. We then compared the effective conductance network for the two approaches.

We conclude that while the LL-based estimates help us reconstruct the network visually, by broadly emphasizing where the carrier hops, there can be significant quantitative differences in the computed mobilities or conductances. These quantitative differences can be attributed to two factors. The first is due to the error in

the LL-based Agmon distance for the eigenstate. The hopping rates are extremely sensitive to the exponential tails of the eigenstates. We noted that the error in the LL-based approximation of the states increases with distance and at low temperatures, the hops can extend beyond the nearest neighbors leading to significant errors in the hopping rates. Secondly as mentioned before, at higher temperatures, the excited modes in the wells of the potential begin to contribute to transport. These are not accounted for in our LL-based method.

Therefore, a model that accounts for the excited states is preferable. One approach could be via the Wigner-Weyl method developed recently in references [3, 4], and briefly summarized in chapter 3. The Wigner-Weyl approach was able to account for the phase space behavior of the states, even at higher energies, when the eigenstates delocalize. Perhaps an extension of the Wigner transport theory, briefly outlined in chapter 1 could be an interesting avenue to explore.

Another perspective of this work could be to consider a multiple trapping model [5], where the trap states and energies are predicted by the basins of the effective potential. Charges in the trap states are excited to the extended band states by the thermal vibrations like in hopping transport, but in this case, the transport is dominated by the extended states. Recent work has shown that the effective potential gives reasonable estimations of the mobility edge [6], the energy at which the electronic states transition from localized to delocalized.

Another possible development would be to improve the estimate of the exponential decay of the localized states. As mentioned before, a source of error in our computations was due the difference in the Agmon distance and the exponential tail of the exact eigenstates. This error can be understood as being due to the Agmon distance being defined by the single path that minimizes an integral. A more accurate bound might be obtained by having a weighted sum of the different paths through a path integral formulation. However, such an approach would be computationally more expensive. This issue is present to a lesser degree in 1D, since there is only one path connecting two points in 1D. Therefore, hopping transport in 1D polymers [7] might be an interesting application of the method developed in this manuscript.

Finally, an interesting perspective would be to combine the chapter 2 and chapter 4 to model hopping transport in the space charge regime, thereby accounting for

interactions between the charge carriers, the variations in the electrostatic fields due to the localized charges and also to study the effects of recombination on bipolar transport. Some of these ideas were pursued previously in the context of organic semiconductors [8] using the Miller-Abrahams' model.

References

[1] H. Li et al. "Piezoresistance in Defect-Engineered Silicon". In: *Physical Review Applied* 15.1 (Jan. 2021), p. 014046. DOI: 10.1103/PhysRevApplied.15.014046.

[2] H. Li et al. "Giant, Anomalous Piezoimpedance in Silicon-on-insulator". In: *Physical Review Applied* 11.4 (Apr. 2019), p. 044010. DOI: 10.1103/PhysRevApplied.11.044010.

[3] J.-P. Banon et al. "Wigner-Weyl Description of Light Absorption in Disordered Semiconductor Alloys Using the Localization Landscape Theory". In: *Phys. Rev. B* 105.12 (Mar. 31, 2022), p. 125422. DOI: 10.1103/PhysRevB.105.125422.

[4] P. Pelletier et al. "Spectral Functions and Localization-Landscape Theory in Speckle Potentials". In: *Phys. Rev. A* 105.2 (Feb. 14, 2022), p. 023314. DOI: 10.1103/PhysRevA.105.023314.

[5] D. Monroe and M. A. Kastner. "Generalizations of Multiple Trapping". In: *Philosophical Magazine B* 47.6 (June 1983), pp. 605–620. ISSN: 1364-2812, 1463-6417. DOI: 10.1080/01418638308228266.

[6] P. Pelletier. "Mécanisme de Localisation Des Condensats de Bose-Einstein d'atomes Froids". These En Préparation. Institut polytechnique de Paris, 2019.

[7] R. P. Fornari and A. Troisi. "Theory of Charge Hopping along a Disordered Polymer Chain". In: *Physical Chemistry Chemical Physics* 16.21 (2014), p. 9997. ISSN: 1463-9076, 1463-9084. DOI: 10.1039/c3cp54661f.

[8] W. F. Pasveer et al. "Unified Description of Charge-Carrier Mobilities in Disordered Semiconducting Polymers". In: *Phys. Rev. Lett.* 94.20 (May 23, 2005), p. 206601. ISSN: 0031-9007, 1079-7114. DOI: 10.1103/PhysRevLett.94.206601.

DOCTORAL SCHOOL

Titre : Transport électronique en présence d'états localisés dans les semi-conducteurs désordonnés

Mots clés : transport électronique, localisation, désordre, semi-conducteurs

Résumé : Le développement de l'industrie des semi-conducteurs et, en parallèle, la recherche en physique des semi-conducteurs, a conduit à la miniaturisation des dispositifs à l'échelle du nanomètre. À cette échelle, toutes les imperfections ou inhomogénéités du matériau peuvent avoir un impact considérable sur les performances électriques ou optiques. Les désordres structurels tels que les défauts ou les désordres de composition intrinsèques présents dans les alliages aléatoires peuvent conduire à la localisation des fonctions d'onde électroniques.
Ce travail traite du transport électronique dans les semi-conducteurs en présence d'états localisés. Premièrement, nous décrivons le transport électronique en présence d'états localisés profonds dans le régime de charge d'espace. Le régime de charge d'espace fait référence à des situations où il existe des champs électrostatiques non négligeables dans un semi-conducteur modifiant le flux de courant. La prise en compte du champ électrostatique nécessite la résolution de l'équation de Poisson couplée aux équations de dérive-diffusion. Nous montrons que les effets électrostatiques et les effets de recombinaison via des pièges profonds sont importants pour modéliser convenablement les courbes de polarisation du courant dans des échantillons expérimentaux de silicium piézorésistif.
Nous modélisons ensuite le transport par sauts entre états localisés induit par le désordre intrinsèque. Le transport par sauts se produit lorsqu'un électron saute d'un état localisé à un autre assisté par des phonons. C'est le mode de transport dominant à des concentrations de porteurs suffisamment faibles et à des températures suffisamment basses. Le transport par sauts est souvent étudié à l'aide du modèle de Miller-Abrahams qui nécessite un ensemble de paramètres empiriques pour définir les taux de transition et les chemins préférentiels entre les états. Nous montrons que ce réseau de sauts peut être visualisé avec un potentiel effectif dérivé de la théorie du paysage de localisation, et que le couplage entre états localisés est essentiellement supporté le long de géodésiques d'une métrique déduite du paysage de localisation. Nous calculons les taux de transition à l'aide de ce potentiel effectif et comparons ces prédictions à des calculs exacts des états propres, puis évaluons donc l'applicabilité de la modélisation du transport par sauts à l'aide de la théorie du paysage de localisation.

Title : Electronic transport in the presence of localized states in disordered semiconductors

Keywords : Electronic transport, localization, disorder, semiconductors

Abstract : The development of the semiconductor industry and in parallel, the research in semiconductor physics has led to the miniaturization of devices to the nanometer scale. At this scale, all imperfections or inhomogeneities of the material can drastically impact the electrical or optical performance. Structural disorder such as defects or intrinsic compositional disorder present in random alloys can lead to the localization of the electron wavefunctions.
This work addresses electronic transport in semiconductors in the presence of localized states. First, we describe electronic transport in the presence of deep localized states in the space charge regime. The space charge regime refers to situations when there are non-negligible electrostatic fields in a semiconductor altering the current flow. Accounting for the electrostatic field requires solving the Poisson equation coupled with the drift-diffusion equations. We show that the effects of electrostatics and recombination via deep traps are important to suitably model the current-bias curves in experimental samples of piezoresistive silicon.
We then model hopping transport between localized states induced by intrinsic disorder. Hopping transport occurs when an electron hops from one localized state to another assisted by phonons. This transport is predominant at low enough carrier concentrations and low enough temperatures. Hopping transport is often studied using the Miller-Abrahams' model that requires a set of empirical parameters to define the hopping rates and the preferential paths between the states. We show that this hopping network can be visualized with an effective potential derived from the localization landscape theory, and that the coupling between localized states is essentially supported along geodesics of a metric deduced from the localization landscape. We compute the hopping rates using this effective potential, and compare its predictions with the exact eigenstate calculations, then assess the applicability of modeling hopping transport using the localization landscape theory.

Institut Polytechnique de Paris
91120 Palaiseau, France